Coherent X-ray diffraction studies of mesoscopic materials

Dissertation

zur Erlangung des Doktorgrades
des Department Physik
der Universität Hamburg

vorgelegt von

ANATOLY SHABALIN

Hamburg
2015

Gutachter/in der Dissertation:	Prof. Dr. Edgar Weckert Prof. Dr. Ivan A. Vartanyants
Gutachter/in der Disputation:	Prof. Dr. Edgar Weckert Prof. Dr. Ivan A. Vartanyants Prof. Dr. Wilfried Wurth Prof. Dr. Christian Schroer
Datum der Disputation:	24 November 2015
Vorsitzender des Prüfungsausschusses:	Prof. Dr. Michael Rübhausen
Vorsitzender des Promotionsausschusses:	Prof. Dr. Daniela Pfannkuche
Dekan des Fachbereichs Physik:	Prof. Dr. Heinrich Graener

Abstract

Neue nanostrukturierte Materialen werden mesoskopisch genannt, wenn die charakteristische Länge gro ist im Vergleich mit den elementaren Bausteinen, z.B. Atome oder Moleküle. Teilt man Materialien in makroskopisch und mikroskopisch ein, so können diese durch klassische Physik und durch Quantenphysik beschrieben werden. Mesokopische Materialien bilden die Brücke zwischen der Nano- und der Mikroskala. Aufgrunf ihrer einizigartigen Eigenschaften sind mesoskopische Materialien vielfach in der Nanotechnologie anzutreffen.

Ein bemerkenswertes Beispiel für mesoskopische Materialien sind selbst-organisierte kolloidiale Kristalle. Durch ihre photonische Bandlücke sind kolloidiale Kristalle vielversprechende Bausteine der Photonik. Weiterhin dient der selbst-organisationseffekt kolloidialer Lösungen als anerkanntes Kristallisationsmodel in atomaren Systemen. Diese Beispiele sind die Triebfedern für das steigende wissenschaftliche Interesse an der Herstellung und der gezielten Manipulation der Eigenschaften von kolloidialen Kristallen.

Hochauflösende und drei-dimensionale Bildgebung von mesoskopischen Materialien ist eine eigene Herausforderung. Klassische Mikroskopie mit sichtbarem Licht ist prinzipiell auflösungsbegrenzt und eigent sich daher überwiegend für makroskopische Objekte. Die interne Strukturuntersuchung von opaquen Materialen lässt sich auerdem nur mit hohem Präparationsaufwand durchführen. Oberflächenuntersuchung mit atomare Auflösung erreicht man mit Elektronenmikroskopen. Durch die geringe Eindringtiefe von Elektonen lässt sich die interne Struktur eines Objekts nur durch aufwändige Präparationsmethoden vermessen. Kohärente Röntgen (X-Ray) Streuung eröffnet im Hinblick auf die Vermessung der internen Struktur eines Objekts viel versprechende Ergebnisse. Die vorliegende Arbeit beschreibt inwiefern kohärente Röntgenstreumethoden auf die Strukturanalyse von drei-dimensionalen kolloidialen Kristallen angewendet werden können.

Diese Arbeit widmet sich drei in sich abgeschlossenen Projekten. Zuerst werden Effekte dynamischer Streuungtheorie in Verbindung mit kohärenter Röntgenbeugungsbildgebung (Coherent X-ray Diffractive Imaging, CXDI) vorgestellt. Im zweiten Teil sind die Ergebnisse eines CXDI Experiments an einem einzelnen kolloidialen Kristallkorn zusammengefasst. Ein wichtiges Resultat stellt die Auflösung von einzelnen Partikeln im drei-dimensionalen Kristallgitter dar. Der dritte Teil umfasst Röntgenbeugungsstudien zur Strukturentwicklung von dünnen kolloidialen Kristallschichten unter steigender Temperatureinwirkung. Auf Basis dieser Studien wird ein physikalisches Model zur Beschreibung von nano- und mesoskopischer Strukturentwicklung unter Temperatureinfluss vorgeschlagen.

Abstract

Mesoscopic materials form the subset of nano-structured materials for which the characteristic length scale is large compared with the elementary constituents of the material, i. e. atoms or molecules. These systems form a bridge between macroscopic systems governed by classical physics and atomic systems governed by quantum physics. Due to their unique properties mesoscopic materials find a variety of applications in the fields of nanofabrication and nanotechnology.

A remarkable example of promising mesoscopic material are self-organized colloidal crystals. Due to the existence of the photonic band gap they have valuable potential of applications in photonics. In addition, the process of self-organization in colloidal suspensions widely serves as a simple model of crystallization in atomic systems. These reasons are main drivers for a growing scientific interest in the methods of fabrication and control of intrinsic properties of colloidal crystals.

High resolution three-dimensional imaging of mesoscopic objects is a challenging problem. Available imaging techniques of visible light microscopy can be applied for structural investigations of macroscopic objects, but they are severely limited in resolution. In addition, some of the materials are opaque for visible light which complicates imaging of the internal structure of such samples. High quality images of a surface structure with atomic resolution can be provided by electron microscopy. However, short penetration depth for electrons and elaborate sample preparation in electron microscopy do not allow obtaining information about the bulk without destroying the sample. In this sense X-ray scattering methods offer a great opportunity for in-situ studies of mesoscopic objects. The present work describes how methods of coherent X-ray scattering can be applied to structural investigations of three-dimensional colloidal crystals.

This thesis is devoted to three separate projects, which can be considered as independent. First, the dynamical scattering effects in the Coherent X-ray Diffractive Imaging (CXDI) method will be discussed. Based on the analysis of the model and results of simulations, a straightforward method of correction for the refraction and absorption artifacts in the Bragg CXDI reconstruction is suggested. The second part summarizes the results of an Coherent X-ray Diffractive Imaging experiment with a single colloidal crystal grain. A remarkable result is that positions of individual particles in the crystal lattice have been resolved in three dimensions. The third project is devoted to X-ray diffraction experimental studies of structural evolution of colloidal crystalline films upon incremental heating. Based on the results of the analysis a model of structural evolution of a colloidal crystal upon heating on nanoscopic and mesoscopic length scales is suggested.

Contents

Chapter 1

Coherent X-ray scattering

1.1 X-ray sources

X-rays are a form of electromagnetic radiation with corresponding wavelength similar in scale to atomic dimensions. The most common practice to distinguish them from ultraviolet and gamma rays is based on the photon energy: spectrum of X-rays cover the range from 0.5 keV to 100 keV (see Figure 1.1). Since their discovery in 1895 [2], X-rays have had a profound impact on science, medicine and technology. Very high frequencies and short wavelengths, complex and element sensitive interaction with material, ability to penetrate deep into the interior of solid objects opened a variety of possibilities to use them as invaluable probe of a structure of matter.

X-ray science has been extensively developing over more than a hundred years and it is still developing fast nowadays. Its progress has been closely interconnected with evolution of X-ray sources, since elaboration of new techniques and applications has been requiring new X-ray facilities. At the same time, with the advent of a new generation of X-ray sources new types of experiments became available leading to development of other novel methods. Different mechanisms for the generation of X-rays, available for experiments are illustrated in Figure 1.2.

In an X-ray tube the electrons accelerated by external electric field are slowed down upon collision with the metal target, and emit so-called Bremsstrahlung, or ”braking radiation”. Its spectrum depends on the target material and the accelerating voltage and in general can be described as a smooth, continuous curve with several intense spikes of characteristic lines. The characteristic radiation is emitted in consequence of atomic transition. The electrons knocked out from an inner shell of the atoms are replaced by electrons from higher states. In a consequence of filling the vacancy, the X-ray photon with its energy precisely determined by the electron energy levels is emitted. Since the process of generation and refilling of vacancies is independent for each individual atom, radiation is spatially incoherent (theory of optical coherence will be discussed in Chapter 2) and emitted into all directions. In most experiments only characteristic part of radiation is used, but the Bremsstrahlung is filtered. X-ray tubes have played a significant role in material science. Thus, pioneering experiments with X-ray diffraction on crystals [3, 4] which have initiated a remarkably successful field, called X-ray

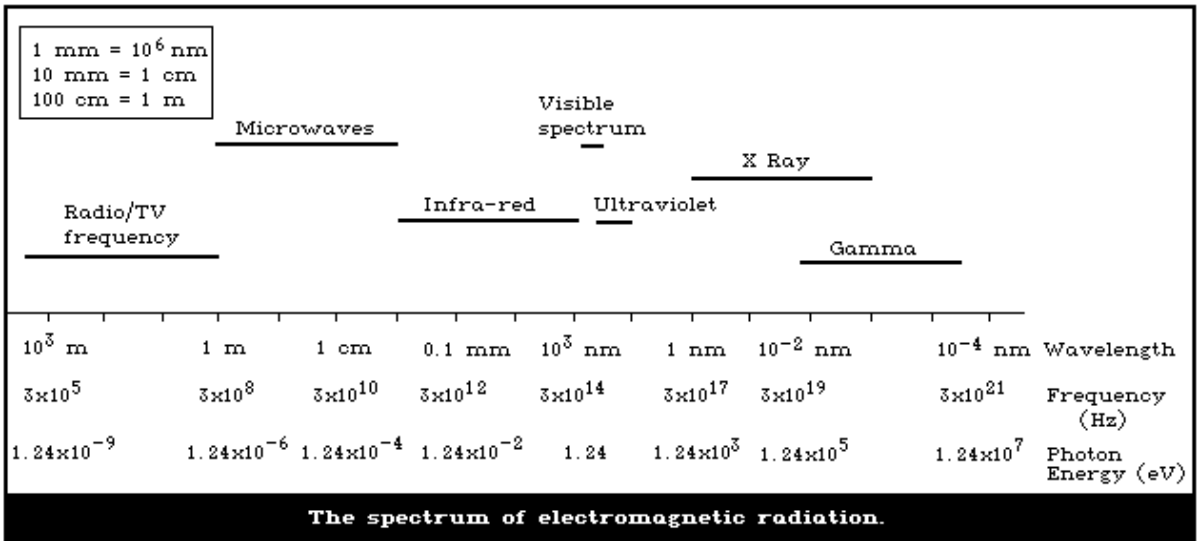

Figure 1.1: The electromagnetic spectrum, showing the major categories of electromagnetic waves [1].

crystallography were performed with X-ray tubes. Modern X-ray tube is a powerful tool which is widely used in science, medicine and industry.

In a different type of X-ray source, as synchrotron, light charged particles, electrons or positrons, accelerated to relativistic speed go through strong magnetic field. The Lorenz force accelerates the particles bending their trajectory and as a result the radiation is emitted. Due to relativistic effects the radiated power is concentrated in a narrow cone with the opening angle $\theta = \gamma^{-1}$ where $\gamma = E/mc^2$ is the particle energy in units of the rest mass energy. The first-generation synchrotron light sources were using synchrotron radiation from accelerator facilities of high energy physics, where it was produced as an undesired side effect, counteracting the intended acceleration. In these big accelerators the electrons were forced to circulate around the storage ring composed of a series of bending magnets separated by straight sections. The synchrotron radiation produced by the magnets was used parasitically. However, soon the unique properties of synchrotron radiation such as high intensity, tunability over a large range of the electromagnetic spectrum, polarization properties, pulsed time structure, and extreme collimation motivated construction of dedicated facilities. These light sources of second generation were exclusively constructed for the production of X-ray synchrotron radiation and became a great step forward in the productivity of experiments.

Current third generation synchrotron light sources [1] optimise the intensity of generated X-rays by incorporating long straight sections into the storage ring for ”insertion devices” such as undulators and wiggler magnets [5, 6]. These periodic magnetic structures composed of many repeating north and south poles force the particles to follow a sinusoidal or helical path. In wiggler these path deflections are rather large and the emission process is incoherent similar to radiation from a bending magnet. At the same time the intensity is enhanced by a factor of N_p, which is the number of magnets in the wiggler. In addition, a continuous spectrum extends to shorter wavelengths.

[1] For example, PETRA III in Germany, ESRF in France, Spring-8 in Japan, APS in the USA and others.

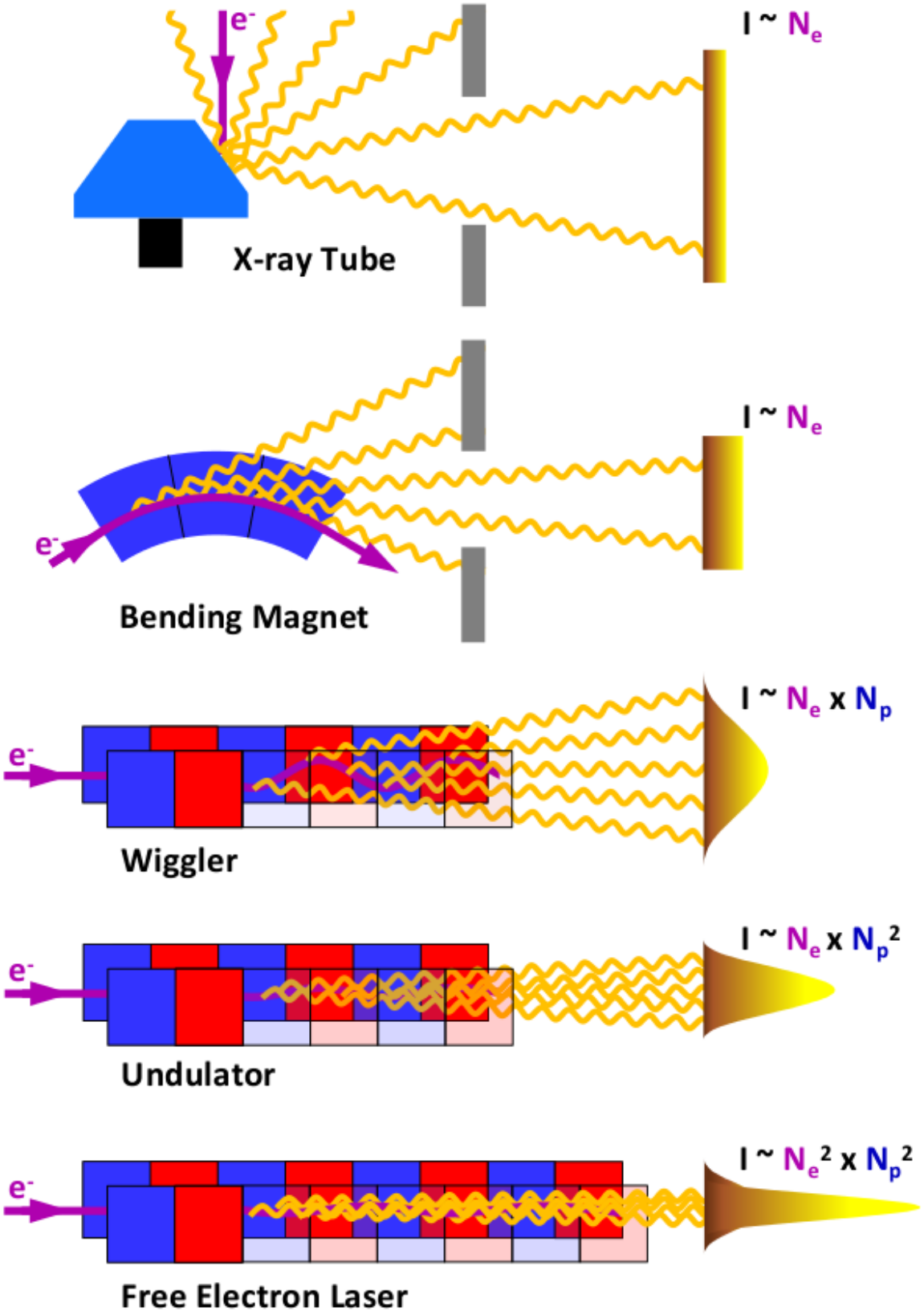

Figure 1.2: Principles of X-ray generation in X-ray tube, bending magnet, wiggler, undulator and Free Electron Laser. The electron beam is always marked in purple and the X-rays are visualized here in orange. The different colors in the magnetic structures indicate the two different magnetic poles.

Undulators are similar to wigglers but generally have weaker fields and more dipoles. In undulator the angular excursions of the particle are much smaller than the natural opening angle of radiation θ. Also, the electromagnetic wave emitted by a single particle in one turn interferes constructively with the field of the same particle emitted in the previous turn. As a consequence, the resulting beam has smaller angular divergence and a spectrum concentrated into narrow bandwidth for a given photon energy and its harmonics n. The resulting opening angle in this case might be approximated by $\theta/\sqrt{N_p}$ and the photon flux can be up to N_p times more than from a bending magnet. Despite the similarity, wigglers evolved independently from undulators at the start. One of the major differences is that the efficient operation of the undulators requires rather small and parallel beam of particles compressed into bunches. In third-generation synchrotron sources a dramatic improvement of the photon beam quality has been achieved due to technological development of storage rings specialized for undulators.

The electromagnetic field generated in the undulator is confined to a narrow cone of angles $\theta = 1/2\gamma$, where $\gamma = 1/\sqrt{1 + (v/c)^2}$ is the Lorentz factor, v is the speed of the particles [2]. The wavelength of emitted radiation can be expressed as [7]

$$\lambda = \frac{\lambda_u}{2\gamma^2}\left(1 + \frac{K^2}{2} + \gamma^2\theta^2\right), \tag{1.1}$$

where λ_u is the undulator period, $K = eB_0\lambda_u/2\pi m_e c$ is the undulator parameter, θ is the off axis angle, B_0 is the magnetic field of the undulator, e is the elementary charge, and m_e is the rest mass of the electron.

Although the radiation from a single electron in undulator is coherent, in the sense that the radiation from one oscillation is in phase with that from the subsequent ones, the radiation from different electrons is incoherent. This comes from the fact that the electrons in the bunch are not ordered spatially. In order to force a group of electrons irradiate as a single one, they have to be compressed into a microbunch with longitudinal thickness less then the wavelength. The principle of fourth generation light sources is based on the idea that the emitted electromagnetic field produced in an undulator can become strong enough to modulate the electron distribution within the electron bunch [8]. Over the length of the undulator the formerly smooth electron bunch becomes structured into several micro bunches. The distance between them is exactly the wavelength of the generated field, although each of the micro bunches is narrower then that. Almost all electrons in this periodic structure begin to emit coherent radiation in phase and thus enhance the modulating field. Through constructive interference the intensity increases exponentially as the electron beam and the radiation co-propagate along the undulator. This process is called Self Amplification of Spontaneous Emission (SASE) [9, 10]. It demands long undulator sections and high requirements on the electron beam quality in terms of small emittance, low energy spread, and a large critical current. Light sources based on SASE, also called X-ray free-electron lasers (XFEL), are built on linear accelerators but not the storage rings as conventional

[2] For example, at the third generation synchrotron source PETRA III electrons have an energy of 6 GeV. This yields about 50 µrad of the natural opening angle θ.

synchrotron [11]. Several of them are operating currently [3], being constructed [4] or planned [5]. Extreme intensity, high degree of spatial and temporal coherence, ultrashort structure of X-ray pulses produced by XFEL open great opportunities for imaging and time-resolved experiments in materials science and biology.

Due to the weak interaction of X-rays with matter the amount of the photon flux available is crucial for most applications. It is typically characterized by the spectral photon flux, that is determined by number of photons per second within a bandwidth (typically $0.1\,\%$) [12]

$$F(\lambda) = \frac{\text{Photons/second}}{(0.1\,\%\ \text{bandwidth})}. \tag{1.2}$$

In many practical cases the collimation of the beam is important, therefore it becomes more convenient to measure the quality of X-ray source with the brilliance [13]

$$\text{Brilliance} = \frac{\text{Photons/second}}{(\text{mrad}^2)\cdot(\text{mm}^2\ \ \text{source}\ \ \text{area})\cdot(0.1\,\%\ \ \text{bandwidth})}. \tag{1.3}$$

Distinct to the spectral photon flux this characteristic takes into account the source area (in mm^2) and the angular divergence of the photons (in mrad^2), or how fast the beam spreads out. With higher brilliance more photons can be concentrated in a spot. The Figure 1.3 illustrates trends in brilliance of X-ray sources since their invention to nowadays. Typically, the brilliance and the coherence properties of the X-ray beam are determined by the electron bunch properties and are thus limited by the ring characteristics. An important aspect for high-quality beam is how densely the electron bunch is packed and its transverse velocity spread. That is characterized by the electron beam emittance $\epsilon_e = \sigma_e \sigma'_e$, where σ_e and σ'_e is the size of the electron bunch and its divergence, respectively. A low emittance of the photon beam results in a higher brilliance and a higher coherent photon flux of the source.

1.2 Basics of X-ray scattering

The interaction of X-rays with matter includes variety of effects with high sensitivity to material properties at different scales. There are two common approaches to describe it: to treat the material as a continuum, with an interface to the surrounding or to consider it as an ensemble of atoms or molecules. First, the interaction of X-ray photon with a single atom will be discussed.

Generally, it can happen in one of two ways: the photon can be scattered or it can be absorbed. In the case of absorption the photon energy is spent to knock out an electron from the inner shell, and the excess energy is transferred to the electron kinetic energy. This process is known as photoelectric absorption and quantitatively can be described by the linear absorption

[3] For example, SACLA in Japan, SLAC FEL in the USA or FLASH in Germany.
[4] European XFEL in Germany, SwissFEL in Switzerland and others.
[5] For example, NGLS in the USA.

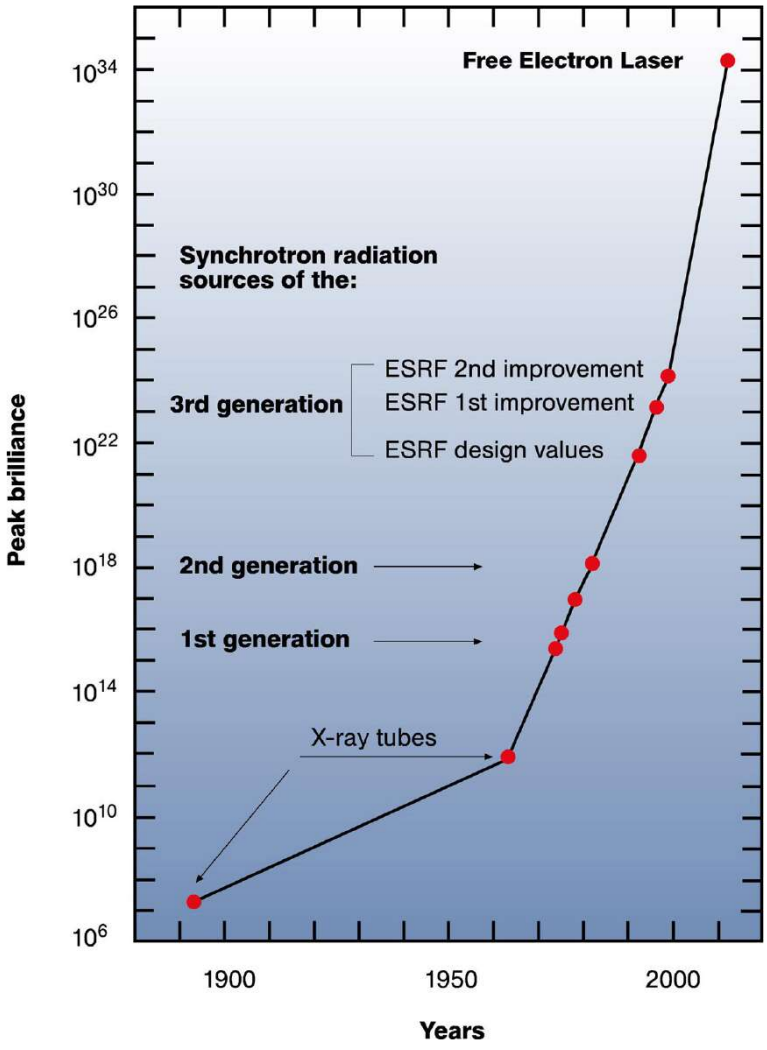

Figure 1.3: Evolution of the peak brilliance of different X-ray sources. The Figure was adopted from European XFEL website [14].

coefficient μ in differential equation

$$-dI(z) = I(z)\mu dz. \tag{1.4}$$

Here μdz is the attenuation of the beam through an infinitely small sheet of thickness dz at a depth z from the surface. The solution of this equation establishes an exponential decay of the intensity in the direction of the beam propagation and is known as the absorption law

$$I(z) = I_0 e^{-\mu z}, \tag{1.5}$$

where the incident beam intensity at $z = 0$ is denoted as I_0. The absorption cross section has a distinct dependence on the photon energy $\mathcal{E}$ and atomic number Z of the absorber. Far from the absorption edges corresponding to characteristic energies of electrons in atom it is approximately proportional to $Z^4/\mathcal{E}^3$.

Differences in the absorption cross-section between different elements make X-rays remark-

ably useful for imaging of interior of media. The very first example of such application was demonstrated in 1896 by Röntgen [2], where he visualized the structure of bones in a hand of a living human. Absorbing higher fraction of the radiation than surrounding tissue the bones appeared as a shadow on the photograph. This approach is widely used in imaging techniques, such as in radiography [15] and X-ray computed tomography [16].

The most simple way to understand the scattering process is to consider a single photon colliding with a free charged particle. The electric field of the incident photon accelerates the particle, causing it to emit radiation, and thus the wave is scattered. As far as the atomic nucleus is too heavy to scatter X-ray photon, the only scattering by the electron shell has to be taken into account. We will assume in the following that the distance to the observation point is much larger then the wavelength and size of scattering elements such as atoms, molecules or unit cells in the case of a crystal.

1.2.1 Scattering on a single electron

Let us consider the most elementary case of collision of one X-ray photon with a single, free electron. In a quantum mechanical description, the scattered photon has a lower energy relative to that of the incident one, since part of the energy is transferred to the recoiling electron. This inelastic scattering process is known as the Compton scattering [17]. The shift of the wavelength $\Delta\lambda$ increases with scattering angle Θ according to the Compton formula

$$\Delta\lambda = \frac{2\pi\hbar}{m_e c}(1 - \cos\Theta), \tag{1.6}$$

where $\hbar$ is the Plank constant, m_e is the electron rest mass, and c is the speed of light. The Figure 1.4 illustrates the ratio of the final to initial energy of the photon given by this formula and the relation $\mathcal{E} = 2\pi\hbar c/\lambda$. The scattering becomes progressively more inelastic as the energy $\mathcal{E}$ of the incident X-ray is increased and the difference between energies is more pronounced for larger scattering angles. On the other side the low-energy limit can be well approximated as elastic meaning without any loss of energy as described by the classical electromagnetism theory [18]. This limit is valid as long as the photon energy is much less than the mass energy of the particle. It has to be emphasized that elastic and inelastic scattering are different processes and the energy spectrum of scattered radiation is always composed of them both. Being incoherent, Compton component cannot form an interference pattern [6], but produces a smoothly varying background which sometimes needs to be subtracted from the data. The cross-section of Compton scattering is decreasing with decrease of the incident energy while the cross-section of elastic scattering is getting more and more dominant. Theoretical and experimental studies described in this work are focused on the latter type of X-ray scattering, known also as Thomson scattering.

[6] The coherence and the role of the statistical properties in the formation interference pattern will be discussed in the next Chapter.

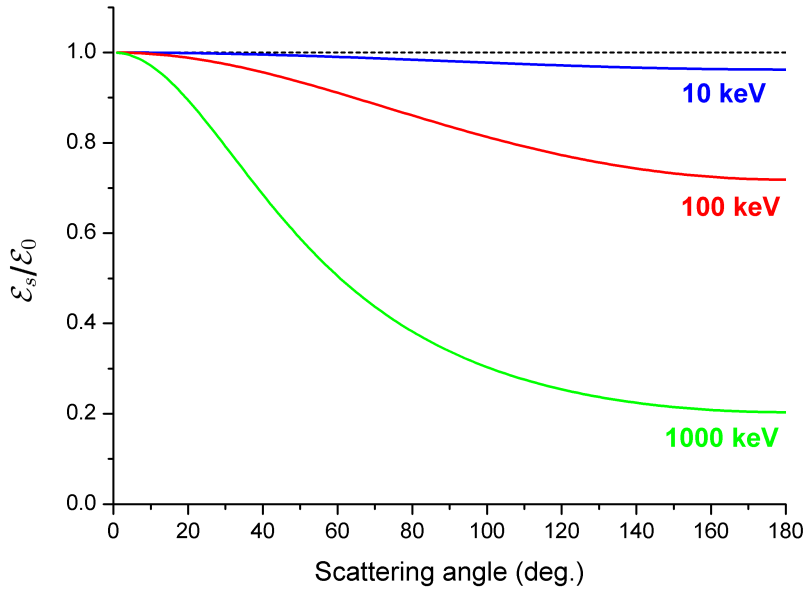

Figure 1.4: The ratio of the energy $\mathcal{E}_s$ of the scattered photon to the energy $\mathcal{E}_0$ of the incident one as function of scattering angle.

In the classical electromagnetic theory the process of the elastic scattering is described in the following way. The electron is accelerated by the electric field component $\mathbf{E}_{in}$ and moves in the direction of its oscillations, resulting in the dipole radiation

$$\mathbf{E}_s = \frac{1}{c^2 R}[[\ddot{\mathbf{d}}\mathbf{n}]\mathbf{n}]. \tag{1.7}$$

Here the direction to the point of observation located at distance R_0 from the electron is given by the unit vector $\mathbf{n}$. The second time derivative of the dipole moment can be expressed as a function of accelerating electric field from the Newton's second law $\ddot{\mathbf{d}} = e^2\mathbf{E}_{in}/m_e$. With respect to the polarization of the incident beam, the scattered amplitude can be rearranged as

$$\mathbf{E}_s(R, \Psi, t) = -r_0 \frac{e^{i\omega R/c}}{R_0} \sin\Psi \cdot \mathbf{E}_{in}(t - R/c). \tag{1.8}$$

Here the constant $r_0 = e^2/(m_e c^2) = 2.82 \times 10^{13}$ cm is a classical radius of the electron, and the angle Ψ is formed by the direction of the polarization of the incoming field and direction to the observation point (see Figure 1.5). The observable quantity is intensity I_s defined as energy per unit area per unit time that is given by the Poynting vector in CGS units averaged over the oscillation period

$$I_s = \frac{c}{8\pi}\langle \mathbf{E}_s^2 \rangle = I_0 \frac{r_0^2}{R^2} \sin^2\Psi = I_0 \frac{r_0^2}{R^2} C. \tag{1.9}$$

The polarization factor $C = \sin^2\Psi$ is usually expressed through the scattering angle Θ. It equals 1 in the case of the σ-polarization when the direction of oscillations of the electric field is perpendicular to the scattering plane determined as the plane formed by the wave vectors of

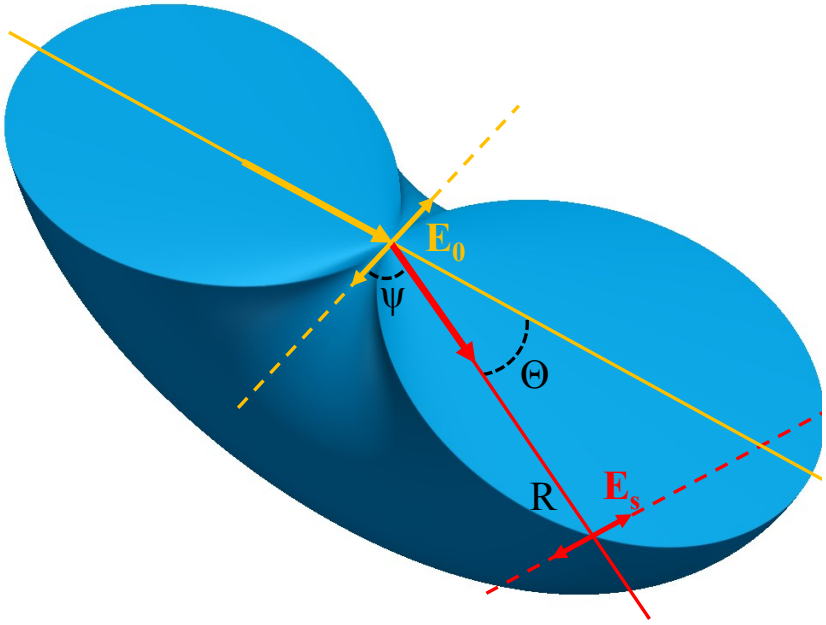

Figure 1.5: The angular dependence of Thomson scattering illustrated as a surface of constant intensity. For clarity only lower part of the surface is shown. The direction of the electric field oscillations is shown by orange for the incident radiation and by red for the scattered one.

the incident and the scattered waves. In the case of the π-polarization which corresponds to in-plane oscillations the polarization factor is given by $cos^2\Theta$. The Figure 1.5 illustrates angular dependence of the scattered radiation which takes the form of a donut with its maximum in the equatorial plane. In the case of unpolarized primary beam the σ and π components have equal contributions, so that

$$C = \frac{1 + \cos^2 \Theta}{2}. \tag{1.10}$$

Being more strong in a direction perpendicular to acceleration, the scattered radiation appears to be more or less polarized, depending on where an observer is located. In this way the process of scattering always produces partial polarization which becomes linear at 90° as far as only σ-component can be scattered at this angle.

1.2.2 Scattering on atom

The radiation field scattered by an atom is a superposition of contributions from all electrons, where the magnitudes of all the terms are the same because characteristic size of atom is orders of magnitude smaller than the distance to the observation point. That size, however, is comparable with the wavelength of the radiation, therefore the phases of terms defined by the optical path depend on the position of the scattering volume in atom.

Let us consider the phase difference, between the wave scattered by a volume element around the origin and that, scattered by another one located at $\mathbf{r}$ (see Figure 1.6). The part of the optical path which is common for both wave can be omitted. If the incoming wave is

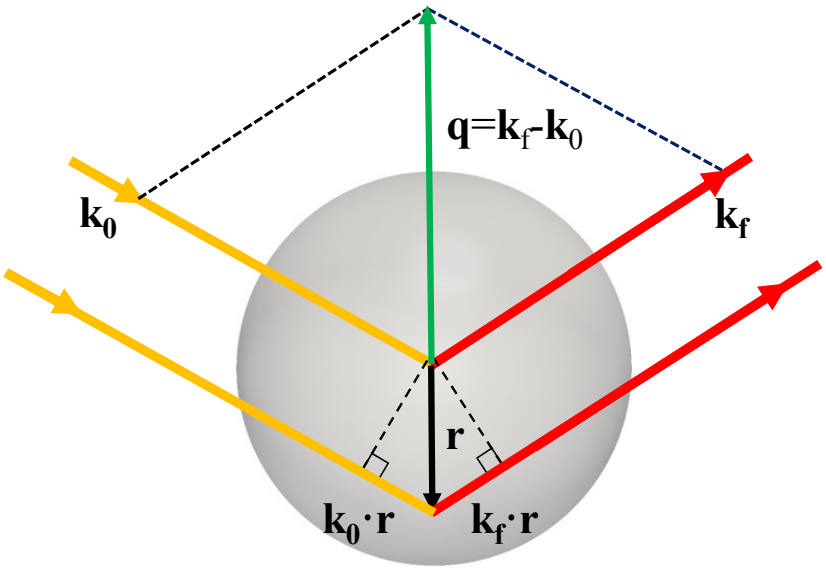

Figure 1.6: Scattering from an atom. The wavevectors of the incident and the scattered waves are denoted as $\mathbf{k}_0$ and $\mathbf{k}_f$. The difference in phase between a wave scattered at the origin and one at a position $\mathbf{r}$ is given by $\mathbf{k}_0 \cdot \mathbf{r} - \mathbf{k}_f \cdot \mathbf{r}$.

assumed to be plane the phase difference is given by expression

$$\Delta\phi(\mathbf{r}) = \mathbf{k}_0 \cdot \mathbf{r} - \mathbf{k}_f \cdot \mathbf{r} = -\mathbf{q} \cdot \mathbf{r}, \tag{1.11}$$

where $\mathbf{k}_0$ and $\mathbf{k}_f$ are the wavevectors of the incident and scattered fields and the scattering vector $\mathbf{q} = \mathbf{k}_f - \mathbf{k}_0$ is known as the wavevector transfer. If the electron density distribution is specified by a number density, $\rho(\mathbf{r})$ the resulting scattered amplitude from the whole atom will be proportional to a Fourier transform

$$f(\mathbf{q}) = \int \rho(\mathbf{r}) e^{-i\mathbf{q}\cdot\mathbf{r}} d\mathbf{r}, \tag{1.12}$$

known as the atomic form factor. In the limit $\mathbf{q} \to 0$ all different volume elements scatter in phase so that f approaches Z, the number of electrons in the atom. As $\mathbf{q}$ increases from zero the different volume elements start to scatter out of phase and consequently $\lim_{\mathbf{q}\to\infty} f(\mathbf{q}) = 0$.

Typically the electron distribution in the atom considered as being spherically symmetric thus the integral in equation (1.12) has only real part, denoted hereafter as f^0. It should be noted that given model of scattering by an atom does not take into account the fact that electrons in atom are not free but bounded with certain discrete energy levels. In more accurate treatment the corrected atomic scattering factor can be presented as

$$f = f^0 + \Delta f' + i\Delta f'' \tag{1.13}$$

where $\Delta f'$ and $\Delta f''$ are the real and imaginary parts of the anomalous dispersion correction [19]. They are normally considered as functions of the X-ray energy $\hbar\omega$ only as far as the angular dependence of these values is much smaller than that of f^0. When the ω is close to one of the resonant frequencies in atom, the total scattering dramatically increases and all components in the decomposition (1.13) reach their extremal values. As consequence, the energy dependence of the absorption coefficient displays a sharp variation in the vicinity of that resonance, that is known as absorption edge. In this narrow energy range the atomic factor reveals high sensitivity to the electronic states structure in the atom. That is widely used in the methods of X-ray absorption spectroscopy, such as Extended X-ray Absorption Fine Structure (EXAFS) and X-ray Absorption Near-Edge Structure (XANES) [20]. At the same time, far from the absorption edges the dispersion correction parts are rather small. Tables of values f^0, $\Delta f'$ and $\Delta f''$ are given in the International Tables For Crystallography [21].

The treatment of the scattering by an atom, which has been given here, is rather simplified and ignores the X-ray fluorescence [22], magnetic scattering by the electron spin [23], influence of molecular vibrations [24] and other effects. However, this classical approach is entirely sufficient in the majority of cases dealing with coherent X-ray scattering.

Using the same reasoning for a cluster of atoms we can find that the scattered field from a small object of size d at the distance z is directly proportional to the Fourier transform of the electron density distribution function. Because of this relationship between real space spanned by $\mathbf{r}$ and the Fourier space spanned by $\mathbf{q}$, the latter is referred to as reciprocal space. This basic relation is widely used in X-ray scattering although the limitations of this simple approach have to be discussed.

First, the observation point has to be located in the far-field, which is defined as a zone where the Fresnel number

$$N_f = \frac{d^2}{\lambda z}, \tag{1.14}$$

is much less than unity. If this condition is fulfilled, the optical paths can be treated as parallel for all points within the object which results in the phase difference $\mathbf{q} \cdot \mathbf{r}$. Second, the model assumes the incoming radiation to be a plane wave throughout the whole object and also that the scattered wave does not experience rescattering on the way to the observation point. In the literature that is often referred as the first Born approximation [25]. Due to weak interaction of X-rays with media such assumptions work well for small samples consisting of comparably small number of atoms or molecules, where the effects of interference can be neglected.

1.3 Kinematical theory of X-ray diffraction by crystals

One of the most remarkable phenomena in X-ray science is the diffraction of coherent X-ray radiation by crystals. In this case ordered ensemble of atoms works as a three-dimensional (3D) diffraction lattice and the radiation, scattered by different atoms interferes positively for certain directions. In the scattering pattern that results in appearance of intense peaks on the detector,

so-called Bragg peaks. This phenomenon was discovered experimentally in 1912 by Max von Laue [3, 26] and explained theoretically in 1913 by William Bragg [4].

There are two theoretical approaches to describe the diffraction of the wave field by periodic structures, known as the kinematical and dynamical theories [27]. The kinematical theory is based on the assumption that the scattered radiation does not experience rescattering on the way to the detector which leads to a considerable simplification. This approximation is also known as the weak-scattering limit because it is valid while the intensity of the diffracted radiation is small in comparison to the intensity of the incident wave [27]. The dynamical theory takes into account the multiple scattering and the interference effects, introduced by coupling of the transmitted and scattered waves in a crystal. First the kinematical theory of X-ray diffraction on the example of an ideal crystal will be discussed.

The ideal crystal is defined as an infinite medium with translational symmetry, which consists of identical cells (single or several atoms, molecules etc.). These unit cells are positioned with an invariable translational symmetry, described by three linearly independent space vectors $\mathbf{a}_1$, $\mathbf{a}_1$ and $\mathbf{a}_3$. Then every unit cell is displaced from one to another one with a distance defined by a translation vector

$$\mathbf{T_n} = n_1\mathbf{a}_1 + n_2\mathbf{a}_2 + n_3\mathbf{a}_3 \tag{1.15}$$

where n_1, n_2, n_3 are integer numbers. That periodic and systematic arrangement of atoms forms a regular repeating pattern called the crystalline lattice. Characteristic symmetries of a given lattice which include symmetry elements such as translations, rotations, reflections, and their combinations play key role in mechanical, optical and electrical properties of crystals. The full classification of all crystal structures which comprise the 32 symmetry classes and 14 distinct types of lattices, known as Bravais lattices, can be found in standard books on crystallography such as [28].

The electron density in a crystal can be expressed as the convolution of an electron density of a unit cell $\rho_{uc}(\mathbf{r})$ and infinite periodicity function of the lattice multiplied by the shape function $s(\mathbf{r})$ defined as 1 within the crystal and 0 everywhere outside

$$\rho(\mathbf{r}) = \rho_{uc}(\mathbf{r}) \otimes \sum_{\mathbf{n}} \delta(\mathbf{r} - \mathbf{T_n}) \cdot s(\mathbf{r}). \tag{1.16}$$

Here the summation is carried out over all possible integer vectors $\mathbf{n} = \{n_1, n_2, n_3\}$. As it was shown in previous section, the scattered amplitude in the far-field is proportional to the Fourier transform of the electron density if the weak-scattering limit is valid. For the expression (1.16) it can be evaluated as [29]

$$A(\mathbf{q}) = -r_0 F_{uc}(\mathbf{q}) \cdot \left[\frac{(2\pi)^3}{V_{uc}} \sum_{hkl} \delta(\mathbf{q} - \mathbf{G}_{hkl})\right] \otimes s'(\mathbf{q}), \tag{1.17}$$

where the convolution theorem for Fourier Transform [30] was applied. Let us now discuss all components in the formula (1.17) one after another.

The structure factor $F_{uc}(\mathbf{q})$ represents the scattering ability of a single unit cell in the direction corresponding to the scattering vector $\mathbf{q}$ and can be expressed as a sum over all the atoms in the unit cell

$$F_{uc}(\mathbf{q}) = \sum_j f_j(\mathbf{q}) e^{-W_j(\mathbf{q})} e^{-i\mathbf{q}\mathbf{r}_j}, \tag{1.18}$$

where $f_j(\mathbf{q})$ is the atomic factor of the j^{th} atom and $\mathbf{r}_j$ is the position of this atom within the unit cell. The $W_j(\mathbf{q})$ is the Debye-Waller factor which takes into account the attenuation of the coherent scattering properties due to the thermal vibrations of the atoms [31]. Being dependent on a type of the atoms and their spatial arrangement, the structure factor is widely used in solid state physics as a unique footprint of crystalline materials.

The Fourier transform of the direct lattice represents infinite periodicity function in reciprocal space. That is given by the sum of $\delta-$functions normalized by the unit cell volume V_{uc}. It describes a regular grid, or reciprocal lattice, with basis vectors

$$\mathbf{b}_1 = 2\pi \frac{\mathbf{a}_2 \times \mathbf{a}_3}{\mathbf{a}_1 \cdot (\mathbf{a}_2 \times \mathbf{a}_3)};\ \mathbf{b}_2 = 2\pi \frac{\mathbf{a}_3 \times \mathbf{a}_1}{\mathbf{a}_1 \cdot (\mathbf{a}_2 \times \mathbf{a}_3)};\ \mathbf{b}_3 = 2\pi \frac{\mathbf{a}_1 \times \mathbf{a}_2}{\mathbf{a}_1 \cdot (\mathbf{a}_2 \times \mathbf{a}_3)}. \tag{1.19}$$

The position of each node on this grid determines the reciprocal lattice vector

$$\mathbf{G}_{hkl} = h\mathbf{b}_1 + k\mathbf{b}_2 + l\mathbf{b}_3, \tag{1.20}$$

where hkl are integers. Thus the periodicity function takes nonzero values whenever the scattering vector coincides with one of the reciprocal lattice vectors

$$\mathbf{q} = \mathbf{G}_{hkl}. \tag{1.21}$$

The equation (1.21) is called the Laue condition for the observation of X-ray diffraction. Physically that corresponds to the case when the scattered wave from one unit cell is in phase with the waves scattered by surrounding cells. Due to translational symmetry the constructive interference occurs over the whole crystal that leads to bright intensity peak in the selected direction.

A simple and elegant way to visualize diffraction events in reciprocal space graphically is provided by the Ewald construction, shown schematically in Figure 1.7. When the wave vectors of the incident $\mathbf{k}_0$ and diffracted $\mathbf{k}_h$ waves are drawn with respect to the reciprocal lattice they compose a triangle with the third side represented by the scattering vector $\mathbf{q} = \mathbf{k}_h - \mathbf{k}_0$. The vector $\mathbf{k}_0$ points to the origin of reciprocal space and makes an angle of θ_B with the crystalline planes. The vector $\mathbf{k}_h$ begins at the same point as $\mathbf{k}_0$ and follows the direction to the detector position. Then all achievable points in reciprocal space for a given crystal orientation are represented by a sphere of the radius $2\pi/\lambda$, constructed around the beginning point of the wave vectors. In the literature, that spherical cross-section of the reciprocal space is known as the Ewald sphere [28]. It has to be noted that in reality the measured intensity is integrated over some solid angle captured by the detector and the bandwidth of the incident radiation, which defines the thickness of the sphere. In full agreement with the Laue condition the constructive

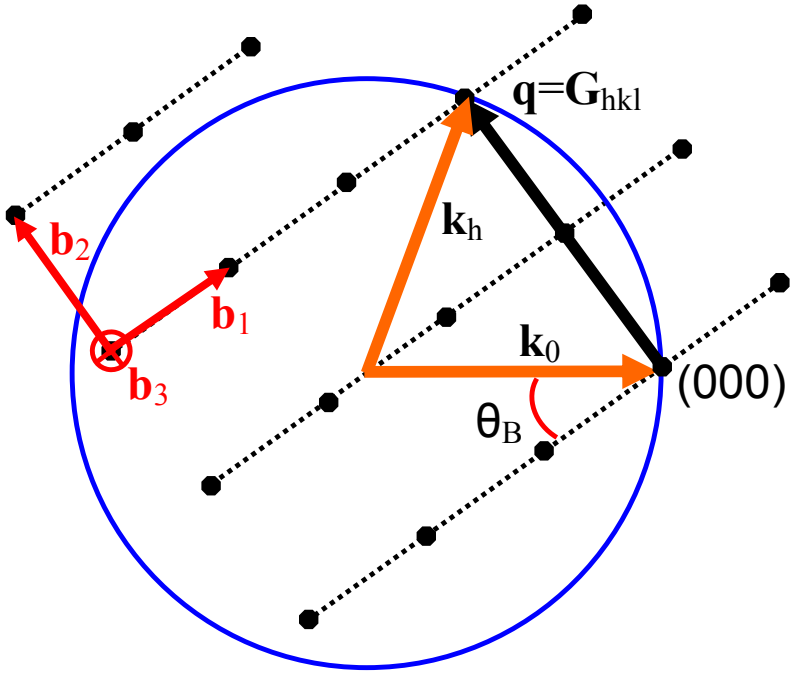

Figure 1.7: Reciprocal lattice of a crystal with the basis vectors $\mathbf{b}_1, \mathbf{b}_2, \mathbf{b}_3$ and a graphical representation of the Bragg condition by the Ewald sphere. The corresponding diffracting planes *in real space* are marked with dash lines. The (000) node is the origin of the reciprocal space, the $\mathbf{q}$ is the scattering vector.

interference can be observed whenever the Ewald sphere cross over one of nodes in reciprocal space with the vector $\mathbf{G}_{hkl}$.

Each node in reciprocal space specified by the reciprocal lattice vector $\mathbf{G}_{hkl}$ corresponds to a set of parallel equidistant planes in the crystal. The spacing between the planes d_{hkl} relates to the magnitude of the reciprocal lattice vector as

$$d_{hkl} = \frac{2\pi}{|\mathbf{G}_{hkl}|}. \tag{1.22}$$

It can be shown that one of the planes passes through the origin of the unit cell, and the next nearest makes intercepts $(\mathbf{a}_1/h, \mathbf{a}_2/k, \mathbf{a}_3/l)$ on the crystallographic axes $(\mathbf{a}_1, \mathbf{a}_2, \mathbf{a}_3)$. The integers hkl, called Miller indices, are commonly used in literature for specifying the family of crystallographic planes. A planar spacing can be calculated from these numbers and the basis of the direct lattice. For example, in case of a cubic lattice directly from the geometry it follows that

$$d_{hkl} = \frac{a}{\sqrt{h^2 + k^2 + l^2}}, \tag{1.23}$$

where a is the lattice parameter. One of the important features of the planes specified by Miller indices is that the density of lattice points in a given family of planes is the same. Thus all lattice points are contained within each family. From the geometry it follows that similar to the reflection from the mirror the angle of incidence on the plane θ is equal to the diffraction angle. Therefore the diffraction peaks from a crystal are often called Bragg reflections. Using

the relation (1.22), the Laue condition (1.21) for a family of reflections can be rewritten as

$$2d_{hkl} \sin\theta = n\lambda, \tag{1.24}$$

where $n = 1, 2, 3..$ is the order of the reflection. This formulation of the diffraction condition is called Bragg's law.

The third component $s'(\mathbf{q})$ in equation (1.17) is the Fourier transform of the shape function. It describes the scattered intensity distribution in the vicinity of reciprocal lattice points and due to convolution with the periodicity function it has identical shape for all of them. For perfect crystals the intensity distribution around each of the reflections has a central symmetry due to Friedel's law [29]. In the presence of the displacement field this symmetry breaks, which can be used for characterization of the strain in crystalline samples [32, 33, 34].

For larger crystals the characteristic width of the peak becomes narrower and vice versa. If the size of the X-ray beam is comparable with the size of the sample, or radiation is not fully coherent on the size of the crystal it introduces additional, instrumental broadening into the peak width. In the case of mosaic crystals the shape of the Bragg peak is composed of contributions from all small perfect blocks with a distribution of orientations around some average value. Then the linear increase of the peak width from first order of reflections to higher orders describes the averaged size and the angular spread of the mosaic blocks. The corresponding analysis of the mosaicity parameters of the crystal by Bragg diffraction is know as Williamson-Hall method [35]. In a limit when the specimen consists of a very large number of microcrystals oriented randomly the Bragg peaks transform into uniform rings. Since all possible crystal orientations are measured simultaneously, the recorded diffraction data correspond to three-dimensional reciprocal lattice projected onto a one-dimensional space [36].

The kinematical theory finds variety of applications in crystallography, topography and imaging. One of the distinguished examples is the X-ray diffraction structural analysis, where the three-dimensional structure of the crystalline material is solved by measuring as many Bragg peaks as possible as a function of Miller indices. In this method the positions and relative intensities of the Bragg reflections are used for the determination of the structure factor. The symmetry of the lattice and distances between the crystallographic planes is determined from the positions of the Bragg peaks, while the information about spatial arrangement of atoms or molecules in the unit cell is obtained from the relative intensities. However, the full information about the structure factor requires also phases of the reflections, which cannot be measured directly. Sophisticated techniques [37] have been developed for finding the unique solution and now the whole process of the structure determination in the case of a single crystal is routine and highly automated.

1.4 Dynamical theory of X-ray diffraction

The dynamical theory takes into account effects of multiple scattering which become essential in the case of X-ray diffraction on a large crystal. Unlike the kinematical approach, dynamical theory gives full description of refraction, extinction and interference effects. It was created by Ewald in 1917 [38] and Max von Laue in 1931 [39] and then summarized in the book of Laue [40] and a review paper of Batterman and Cole [41]. General description of the dynamical theory can be found in the books of Authier [27], Pinsker [42] and Zachariasen [43].

Initially, the dynamical theory was hardly needed in practical applications of X-ray diffraction. Due to weak interaction of X-rays with media the effects of multiple scattering become significant only for relatively large crystals (about microns). Even in this case the kinematic approach is often sufficient, because most of crystalline materials in nature are composed of small perfect blocks with the spread of orientations. Diffraction on each of the blocks can be considered in the frame of kinematical theory with a correction for the loss of intensity occurring when the incident beam crosses the block (so-called, the secondary extinction). The scientific interest to the dynamical theory started to increase rapidly when artificially grown large perfect crystal of silicon and germanium became the raw materials of the semiconductor revolution [44]. Nowadays, the dynamical theory of X-ray diffraction finds variety of applications in different aspects of modern X-ray science, in particular, X-ray optics. This chapter is aimed to give a brief introduction into those aspects of this theory which directly concern the subject of this thesis.

1.4.1 Wave equation

In the most general case both the incoming and scattered wave fields are propagating through the material in accordance with the classical electrodynamics. It is more convenient then to treat the material as a continuum, with an interface to the surrounding vacuum (or air) and use the microscopic Maxwell equations as the basis for describing the propagation and diffraction of the electric field in the substance

$$\begin{aligned} \text{curl}\,\mathbf{E} &= -\frac{1}{c}\frac{\partial \mathbf{H}}{\partial t} \\ \text{curl}\,\mathbf{H} &= \frac{4\pi}{c}\mathbf{j} + \frac{1}{c}\frac{\partial \mathbf{E}}{\partial t} \\ \text{div}\,\mathbf{E} &= 4\pi\rho \\ \text{div}\,\mathbf{H} &= 0. \end{aligned} \tag{1.25}$$

Here the electromagnetic field is represented by the vectors of electric and magnetic components of the field $\mathbf{E}$ and $\mathbf{H}$. The equations are presented in cgs units. Applying curl to the first equation and using the mathematical relation curl curl $=$ grad(div) $-\,\Delta$ one can obtain a differential

equation for the electric field

$$\Delta\mathbf{E} - \text{grad}(\text{div}\mathbf{E}) = \frac{\mathbf{1}}{\mathbf{c^2}}\frac{\partial^2\mathbf{E}}{\partial\mathbf{t^2}} + \frac{4\pi}{\mathbf{c^2}}\frac{\partial\mathbf{j}}{\partial\mathbf{t}}. \tag{1.26}$$

It has to be outlined that although characteristic scales for the induced microscopic current $\mathbf{j}$ are comparable to interatomic distances contrary to the conventional macroscopic approach the media is still considered as a continuum.

The total current can be expressed now through the electron density and velocity of the electrons so that $\mathbf{j}(\mathbf{r},t) = e\rho\mathbf{v}(\mathbf{r},\mathbf{t})$. If the forcing field is oscillating with the frequency ω and amplitude $\mathbf{E}(\mathbf{r})$ the Newton's second law, which describes the motion of the electron, can be expressed as $m_e\dot{\mathbf{v}}(\mathbf{r},t) = e\mathbf{E}(\mathbf{r})e^{-i\omega t}$. From this relation the first derivative of the current in equation (1.26) can be obtained as follows

$$\frac{\partial\mathbf{j}(\mathbf{r},\mathbf{t})}{\partial t} = \frac{e^2}{m_e}\rho(\mathbf{r})\mathbf{E}(\mathbf{r})e^{-i\omega t}. \tag{1.27}$$

Consequently the equation (1.26) takes the form

$$\Delta\mathbf{E}(\mathbf{r}) - \text{grad}(\text{div}\mathbf{E}) + \frac{\omega^\mathbf{2}}{\mathbf{c^2}}[\mathbf{1}+\chi(\mathbf{r})]\mathbf{E}(\mathbf{r}) = \mathbf{0}, \tag{1.28}$$

where the linear response of media to the applied electric field is described by the susceptibility

$$\chi(\mathbf{r}) = -\frac{4\pi e^2}{m_e\omega^2}\rho(\mathbf{r}) = -\frac{r_0\lambda^2\rho(\mathbf{r})}{\pi}. \tag{1.29}$$

Here r_0 is the classical electron radius defined in equation (1.8). Since both σ- and π-polarized components of the electric field $\mathbf{E}(\mathbf{r})$ propagate independently of each other, the wave equation (1.28) is typically solved separately for each polarization. In the following we will always consider the case of one polarization and relying on that treat the wave field as a scalar function.

The wave equation (1.28) complemented by the boundary conditions is a general equation for the propagation of electromagnetic waves in media. The variety of effects such as dispersion, refraction and reflection of X-rays, anomalous absorption and X-ray diffraction can be described by a solution of this equation. For example, from the wave equation it follows that the refraction coefficient, defined as relative change of the wavenumber in media in comparison with that in vacuum, is given by

$$n(\mathbf{r}) = \sqrt{1+\chi(\mathbf{r})} = 1 - \frac{r_0\lambda^2}{2\pi}\rho_{at}(\mathbf{r})f(0). \tag{1.30}$$

Here the total electron density $\rho(\mathbf{r})$ was expressed as a product of the number density of atoms ρ_{at} and the atomic form factor for forward scattering $f(0)$. If the dispersion corrections (see equation (1.13)) are taken into account, the refractive index of the material n_m becomes a complex number with an imaginary part corresponding to the absorption. Distinct to the optics of a visible light the real part of the refraction coefficient for X-rays is less than unity since $Re[\chi] < 0$. For that reason the phase velocity in the material $v_m = c/n$, but not the group

one, is more than the speed of light in vacuum c. Due to this some of the optical principles work in opposite direction for X-rays. For example, in contrast to the total *internal* reflection phenomena in optics of visible light, X-rays exhibit an effect of a total *external* reflection, when the beam incident from vacuum on a flat, sharp interface under grazing angles is fully reflected.

1.4.2 Takagi-Taupin equations

In the case of an ideal crystal the susceptibility $\chi(\mathbf{r})$ (1.29) is a periodic function that can be conveniently represented as a Fourier series

$$\chi(\mathbf{r}) = \chi_0 + \sum_h \chi_h e^{i\mathbf{h}\cdot\mathbf{r}}, \tag{1.31}$$

Here the summation is carried out over all reciprocal lattice vectors and the expression for the Fourier component of the susceptibility χ_h has a form

$$\chi_h = -\frac{r_0\lambda^2}{4\pi V_{u.c.}} F_h, \tag{1.32}$$

where $V_{u.c.}$ is the unit cell volume. The values of $\chi_\mathbf{h}$ are on the order of magnitude form 10^{-4} to 10^{-6} for hard X-rays, that is considered as a small parameter in the theory of X-ray diffraction. In the case of weak deformations, when relative displacements are small in terms of interatomic distances, the susceptibility of a deformed crystal $\chi^d(\mathbf{r})$ is defined from that of a perfect one according to the relation $\chi^{(d)}(\mathbf{r}) = \chi^{(p)}(\mathbf{r} - \mathbf{u}(\mathbf{r}))$. Hence, a convenient replacement for the Fourier component $\chi_h^{(p)}$ of a perfect crystal can be used

$$\chi_h^{(d)} \to \chi_h^{(p)} e^{-i\mathbf{h}\cdot\mathbf{u}(\mathbf{r})} \tag{1.33}$$

and in this way equations of the dynamical theory for a perfect crystal are generalized to the case of the deformed one. For the sake of shortness the local displacement field $\mathbf{u}(\mathbf{r})$ will be further referred as simply $\mathbf{u}$.

In order to linearize the differential equation (1.28), with the susceptibility $\chi(\mathbf{r})$ expressed as the Fourier series (1.31), one should express the solution as a sum of waves propagating along the directions $\mathbf{k}_0 + \mathbf{h}$ over all reciprocal lattice vectors.

$$E(\mathbf{r}) = e^{i\mathbf{k}_0\cdot\mathbf{r}}[E_0(\mathbf{r}) + \sum_h E_h(\mathbf{r}) e^{i\mathbf{h}\cdot\mathbf{r}}]. \tag{1.34}$$

Such representation of a total wave field in crystals is known as the decomposition into Bloch waves [45]. Since the interference effects are growing in strength in the vicinity of the Bragg reflections, the contribution of certain wave to the total wave field depends on how close is the Ewald sphere to the corresponding node in reciprocal space.

Let us consider the most simple case of X-ray diffraction, when the Ewald sphere crosses

just one reciprocal lattice nod beside the (000). Then a sum of the Bloch waves can be reduced to a superposition of two waves

$$E(\mathbf{r}) = E_0(\mathbf{r})e^{i\mathbf{k}_0\cdot\mathbf{r}} + E_h(\mathbf{r})e^{i(\mathbf{k}_0+\mathbf{h})\cdot\mathbf{r}}, \tag{1.35}$$

which are propagating along the directions of transmission and diffraction. Contributions from all other waves are neglected since they are negligibly small. This case describes the most simple but at the same time the most typical case of dynamical diffraction and is known in literature as the two-beam approximation.

Substituting the decompositions (1.31) and (1.35) in the wave equation (1.28), written for scalar wave field, and using the substitution (1.33), one can obtain a set of differential equations for the transmitted and diffracted components

$$\begin{aligned} \frac{\partial E_0(\mathbf{r})}{\partial s_0} &= \frac{i\pi}{\lambda}[\chi_0 E_0(\mathbf{r}) + C\chi_{\bar{h}}e^{i\mathbf{h}\cdot\mathbf{u}}E_h(\mathbf{r})], \\ \frac{\partial E_h(\mathbf{r})}{\partial s_h} &= \frac{i\pi}{\lambda}[(\chi_0+\alpha)E_h(\mathbf{r}) + C\chi_h e^{-i\mathbf{h}\cdot\mathbf{u}}E_0(\mathbf{r})]. \end{aligned} \tag{1.36}$$

Here the partial derivatives $\partial/\partial s_0, \partial/\partial s_h$ are taken along the directions of vectors $\mathbf{k}_0$ and $\mathbf{k}_0+\mathbf{h}$ and C is the polarization factor, introduced in equation (1.9). The index $-h$ is denoted as $\bar{h}$ and the angular deviation parameter α has a form

$$\alpha = 2\Delta\theta\sin(2\theta_B), \tag{1.37}$$

where $\Delta\theta$ is an angular deviation from the precise Bragg angle so that $\Delta\theta = \theta - \theta_B$.

The equations (1.36), known as the Takagi-Taupin equations [45, 46], play a significant role in the dynamical theory. Complemented by boundary conditions they can be solved numerically, or in some specific cases analytically. The detailed derivation of Takagi-Taupin equations can be found in Chapter 3.

1.4.3 Kinematical limit of the dynamical theory

The cross-component terms with factors χ_h and $\chi_{\bar{h}}$ in the set of equations (1.36) describe the coupling between the transmitted and diffracted waves, while two other terms with factor χ_0 both describe effects of refraction and absorption. For a small crystal the amplitude of the diffracted wave is small in comparison with the amplitude of the primary beam, therefore the cross-component term in the first equation can be neglected. Consequently, this equation becomes independent on the diffracted wave and the propagation is performed by integration along the direction of transmission.

$$E_0(l) \propto e^{\frac{i\pi}{\lambda}\chi_0 l}. \tag{1.38}$$

Here the real part of χ_0 multiplied by $i\pi/\lambda$ provides a phase shift which is proportional to the optical path l in the material and corresponds to the refraction phenomenon.The imaginary

part gives a real decrement that corresponds to attenuation of the amplitude due to absorption process. If these effects are also neglected by assumption of $\chi_0 = 0$ the amplitude of the transmitted wave is constant over the whole crystal and the diffracted amplitude can be obtained by integration of the second equation. Consequently, the Takagi-Taupin equations are reduced to

$$\begin{aligned} \frac{\partial E_0(\mathbf{r})}{\partial s_0} &= 0, \\ \frac{\partial E_h(\mathbf{r})}{\partial s_h} &= \frac{i\pi}{\lambda}[\alpha E_h(\mathbf{r}) + C\chi_h e^{-i\mathbf{h}\cdot\mathbf{u}} E_0(\mathbf{r})], \end{aligned} \tag{1.39}$$

which represents purely kinematical case, as far as the last term with χ_h describes diffraction with a single scattering event. In such a way, the results of the dynamical theory in a limit of a small crystal converge to the predictions of the kinematical theory.

The effects of the multiple scattering becomes valuable only for large crystals, when the contribution of the amplitude $E_h(\mathbf{r})$ in equations (1.36) becomes comparable with that of $E_0(\mathbf{r})$. The deeper the radiation penetrates into the crystal the more energy is transferred from the transmitted wave to the diffracted one. Propagating through the crystal the primary beam becomes more and more attenuated. This effect is known as primary extinction [47]. For a finite size crystal the evolution of the wave field and, consequently, the extinction process depend also on the crystal's shape and the diffraction geometry. When the precise Bragg condition is satisfied the characteristic length of attenuation, or extinction depth Λ, which corresponds to decay of the transmitted wave in e times is defined as [27]

$$\Lambda = \frac{\lambda\sqrt{\gamma_0|\gamma_h|}}{\pi\sqrt{\chi_h\chi_{\bar{h}}}}. \tag{1.40}$$

Here the geometrical factor $\sqrt{\gamma_0|\gamma_h|}$ is composed of the directional cosine angles for the incident and diffracted beams

$$\gamma_0 = \cos(\mathbf{k}_0, \mathbf{n}), \;\; \gamma_h = \cos(\mathbf{k}_0 + \mathbf{h}, \mathbf{n}), \tag{1.41}$$

where $\mathbf{n}$ is the surface normal. The diffraction geometry is called symmetric if the wave vectors $\mathbf{k}_0$ and $\mathbf{k}_0+\mathbf{h}$ make the same angle with the crystal surface, i.e. when $|\gamma_0| = |\gamma_h|$. The extinction depth is commonly used as a characteristic length to distinguish between the kinematical and dynamical diffraction.

There are two main cases of practical importance described in literature as Bragg and Laue geometries [27] (see Figure 1.8). In the Bragg geometry the diffracted beam exits from that side of the crystal where the incoming beam is entering the crystal. In the Laue geometry the diffracted beam exits from the opposite side of the crystal. The geometrical factor $\sqrt{\gamma_0|\gamma_h|}$ equals to $\sin\theta_B$ in the symmetric Bragg case, and $\cos\theta_B$ in the symmetric Laue case.

1.4.4 Bragg and Laue diffraction from an infinite crystalline plate

One of the illustrative cases of the dynamical theory is the diffraction of a plane wave by a thick crystalline plate infinite in two dimensions (see Figure 1.8), which is also a case of great practical importance. The set of equations (1.36) are then supplemented by the following boundary conditions on the upper and lower surfaces for the Bragg and Laue geometries:

$$\textbf{Bragg:}\begin{cases} E_0(z)|_{z=0} = E_{in} \\ E_h(z)|_{z=L} = 0 \end{cases} \qquad \textbf{Laue:}\begin{cases} E_0(z)|_{z=0} = E_{in} \\ E_h(z)|_{z=0} = 0 \end{cases}. \tag{1.42}$$

Using the Riemann method, the analytical solution for the reflected and transmitted waves can be obtained [48]. When the Bragg condition is fulfilled, the total electromagnetic field introduced in equation (1.35), reveals periodic standing wave pattern that has the same period as the crystal lattice. Specific feature of this pattern is that the position of nods is extremely sensitive to the slightest deviation of the atomic planes (or individual atoms) from their correct position within a perfect crystal (or on its surface). Thus, the atomic positions can be scanned by the X-ray interference field and exactly determined if the yield of the element-specific photoelectrons or X-ray fluorescence photons is recorded as a function of the glancing angle. This makes the standing waves method particularly useful for analysis of the structure of crystals and their adsorbates at the atomic level. An excellent experimental example, displaying this aspect of dynamical diffraction is given by the angular dependence of the absorption in the Laue case discovered by Borrmann [49]. If the antinodal planes pass through the atom sites, the radiation suffers enhanced absorption (*anomalous absorption*). In the opposite case, when the antinodes are located in the middle between the lattice planes, the radiation travels along them with a less than normal absorption (*anomalous transmission*).

Figure 1.9(a) illustrates results of dynamical diffraction from Si crystalline plate infinite in two dimensions in the Bragg geometry. The considered (111) crystallographic planes were assumed to be parallel to the crystal surface. The selected photon energy was $8\,\mathrm{keV}$, which yields $14.3°$ of the Bragg angle. The angular dependencies of the amplitude and phase of the reflected wave are calculated for two different values of crystal thickness L. Considering that an effective attenuation distance for X-rays upon the dynamical diffraction is represented by the extinction depth $\Lambda = 1.72\,\mu\mathrm{m}$, all other distances shall be compared with this typical distance. The Figure 1.9(a) presents a purely dynamical case of a thick crystal with $L = 100\Lambda$. In a very small region of angular deviation $\Delta\theta$ from the Bragg condition, the reflectivity curve

$$R(\Delta\theta) = \left.\frac{E_h(z,\Delta\theta)}{E_0(z,\Delta\theta)}\right|_{z=0}, \tag{1.43}$$

shows sharp asymmetric peak with the maximum of the order of unity in modulus. Remarkably, that the phase shift between the reflected and incident fields changes from π to 0 across this curve. The left and right edges correspond to the antinodes passing either in between diffracting planes or through them, which results the difference in absorption. In consequence of the

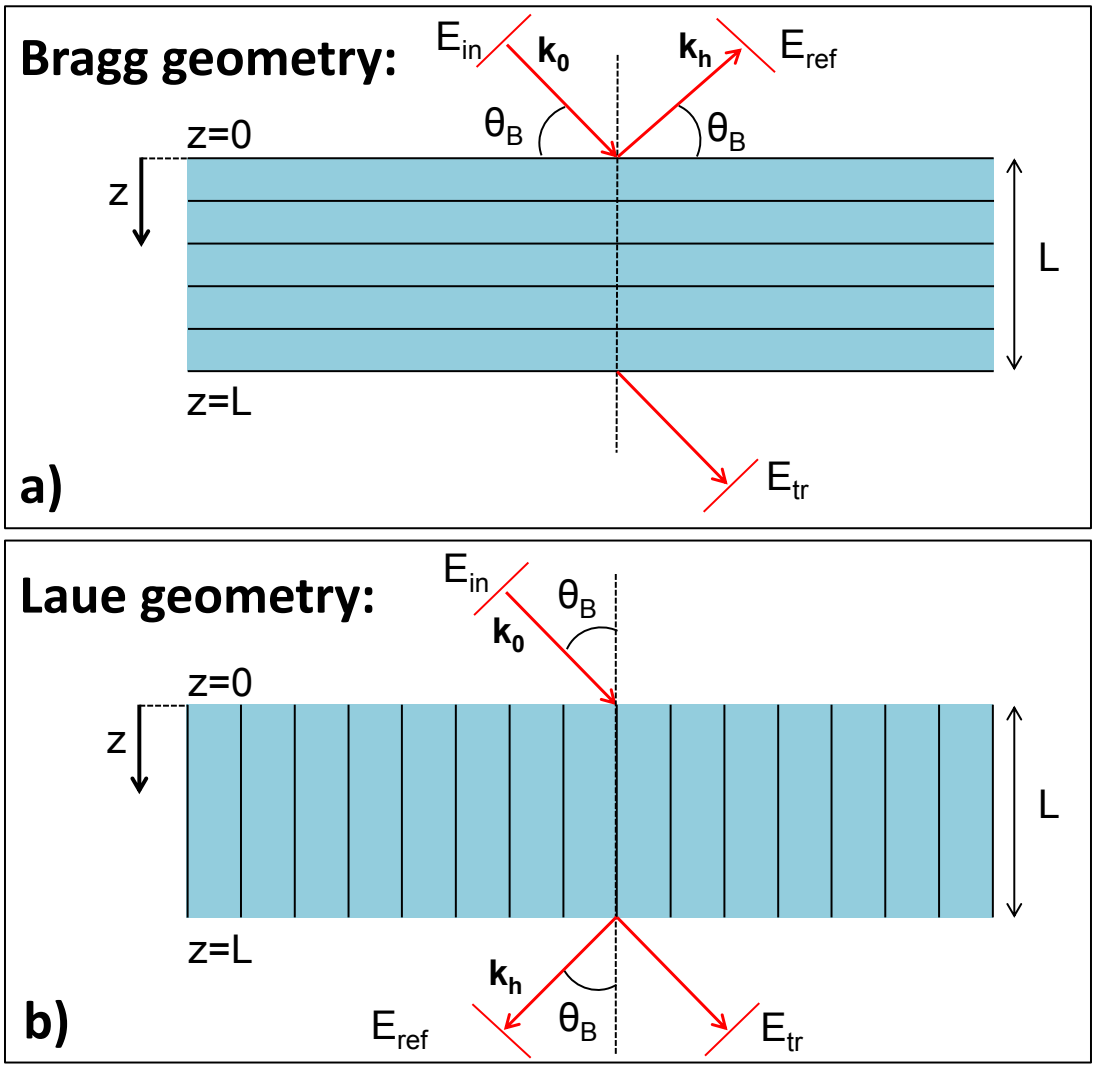

Figure 1.8: Bragg (a) and Laue (b) diffraction geometries in the case of a crystalline plate. The z axis corresponds to the depth from the surface plane, L is the thickness. In symmetric case (the crystalline planes are not inclined with respect to the surface plane), the angle of reflection is equal to the incident angle.

refraction the position of the peak is shifted with respect to the value, provided by Bragg's law (1.24). Significant difference from the kinematical predictions is also revealed by the width of the reflectivity curve. According to the kinematical theory the width of the Bragg peak becomes infinitely small with the increase of the crystal thickness. Contrary to that, in dynamical theory it converges to a certain value, which is typically about 0.1 mrad.

For the sake of completeness an intermediate case between the dynamical and the kinematical diffraction was considered. In the Figure 1.9(b) the same dependencies calculated for the crystalline plate of $L = \Lambda$ thickness are presented. Since the amplitude of the diffracted wave is rather small, the coupling between E_0 and E_h does not contribute much to the wave field distribution in the crystal and the obtained results are rather close to the kinematical prediction. The reflectivity curve is almost symmetric and reveals oscillations on the tails which arise from the interference of crystal truncation rods – streaks of scattering in reciprocal space in the direction normal to the surface.

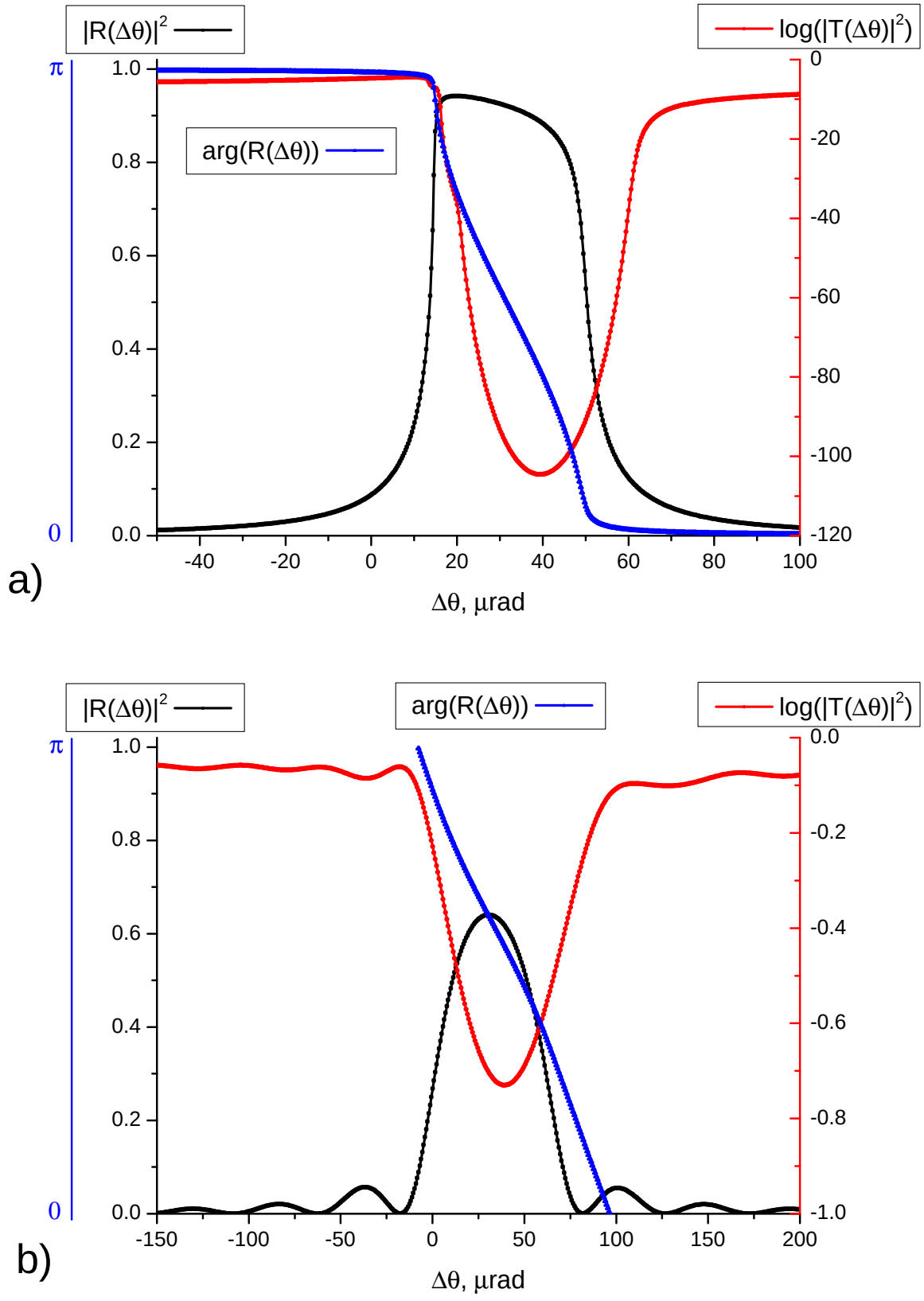

Figure 1.9: (a) The angular dependence of the squared modulus of the reflectivity coefficient $|R(\Delta\theta)|^2$ (black curve), its phase (blue curve) and the transmission coefficient $|T(\Delta\theta)|^2$ (red curve) for thick crystalline plate $L = 100\Lambda$. (b) The same dependencies for the thin crystal ($L = \Lambda$).

Chapter 2

Coherent X-ray Diffractive Imaging (CXDI)

2.1 Coherence

In the classical electromagnetic theory [18] the wave field is assumed to have defined amplitude and phase at each considered point. In many realistic cases this description is not comprehensive due to the statistical nature of light, e.g. the total radiation field fluctuates as a function of time. These fluctuations are much faster than current electronic devices for detection, therefore only statistical properties of these fluctuations can be determined. In the theory of statistical optics and optical coherence [50, 51] the radiation field is treated with a correlation function of the complex wave fields. The coherence, in general, describes all properties of the correlation between the physical quantities of a wave. Experimentally the coherence can be determined as a possibility to observe an interference, one of the most fundamental phenomena in physics.

In the concept of optical coherence the mutual coherence function that is defined as

$$\Gamma(\mathbf{r}_1, \mathbf{r}_2; t_1, t_2) = \langle E^*(\mathbf{r}_1, t_1) E(\mathbf{r}_2, t_2) \rangle, \tag{2.1}$$

plays the main role. It is determined as a first order correlation function between two complex values of the electric field $E(\mathbf{r}_1, t_1)$ and $E(\mathbf{r}_2, t_2)$ at different points $\mathbf{r}_1$ and $\mathbf{r}_2$ and different times t_1 and t_2. The brackets denote the ensemble average [50], which is generally defined as

$$\langle f(\mathbf{r}, t) \rangle = \lim_{N \to \infty} \frac{1}{N} \sum_{\tau=1}^{N} f^{(\tau)}(\mathbf{r}, t), \tag{2.2}$$

where $f^{(\tau)}(\mathbf{r}, t)$ is one realization from the ensemble of all possible realizations of the statistical function $f(\mathbf{r}, t)$. In the theory of statistical optics the fluctuations of the wave field are typically assumed to be ergodic, which means that statistical average can be replaced by the time average

$$\langle f(\mathbf{r}, t) \rangle_T = \lim_{T \to \infty} \int_{-T/2}^{T/2} f(\mathbf{r}, t) dt. \tag{2.3}$$

In the following we will also assume the ensemble statistics do not depend on time $\Gamma(\mathbf{r}_1, \mathbf{r}_2; t, t+\tau) = \Gamma(\mathbf{r}_1, \mathbf{r}_2; \tau)$ (i.e. a stationary random process).

If two points and times coincide the mutual coherence function gives the average of intensity

$$\langle I(\mathbf{r}, t)\rangle_T = \Gamma(\mathbf{r}, \mathbf{r}, \tau = 0) = \langle |E(\mathbf{r})|^2\rangle_T. \tag{2.4}$$

This can be used for normalization of the mutual coherence function that yields the complex degree of coherence

$$\gamma(\mathbf{r_1}, \mathbf{r_2}; \tau) = \frac{\langle E^*(\mathbf{r_1}, t)E(\mathbf{r_2}, t+\tau)\rangle_T}{\sqrt{\langle I(\mathbf{r}_1, t)\rangle_T}\sqrt{\langle I(\mathbf{r}_2, t+\tau)\rangle_T}}. \tag{2.5}$$

This function has an importance in interference experiments, because the modulus of this value corresponds to the contrast of the interference fringes. It can take values from 0 defining the completely incoherent case to 1 for the fully coherent case. All intermediate values correspond to partially coherent field. As it follows from the definition (2.5) when two points and times coincide the complex degree of coherence yields 1 which means that the field is always coherent with itself in a single point. If the separation between the points in space $\mathbf{r}_2 - \mathbf{r}_1$ and time τ increases, then the degree of coherence drops down to values below 1. Therefore, the coherence volume can be defined as a region throughout the space and time within which the electromagnetic field is highly correlated (see Figure 2.1). A characteristic size of this volume in the spatial and in temporal domain is called the transverse and longitudinal coherence length. In most cases, transverse and longitudinal coherence can be treated as independent.

Before we proceed, let us introduce two formulas which have important implications for the estimates of coherence properties in practical cases. The first one follows from the Van Cittert--Zernike theorem [51]. It serves for the determination of the transverse coherence length L_t at distance z from a spatially incoherent source

$$L_t = \frac{\lambda z}{2\pi D}. \tag{2.6}$$

Here D is the source size and λ is the wavelength. As it follows from this formula, the radiation from fully incoherent source exhibits a non-zero degree of coherence at large distances.

The second formula is used for estimates of the longitudinal coherence length and can be obtained from the Wiener-Khinchin theorem [50]. According to that, the autocorrelation function $\Gamma(\tau)$ of a stationary process can be expressed as the Fourier transform of the power spectrum

$$\Gamma(\tau) = \frac{1}{2\pi}\int S(\omega)e^{i\omega\tau}d\omega. \tag{2.7}$$

In the assumption that the wave field has a Gaussian distribution of power over optical fre-

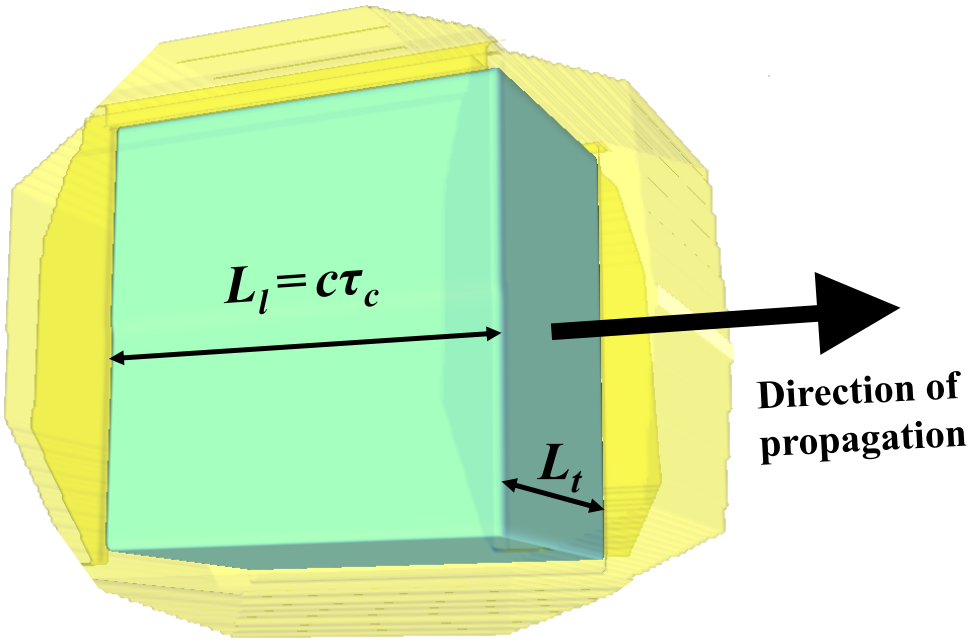

Figure 2.1: Schematic of coherence volume (cyan cube) whose length L_l is determined by the coherence time and whose cross-sectional area is determined by the transverse coherence length L_t. The translational region (outlined by yellow) is not sharp because the mutual coherence function gradually goes to zero.

quency, the spectral bandwidth $\Delta\omega$ and the coherence time τ_c are related to each other as [51]

$$\tau_c = \frac{2\sqrt{2\pi \ln 2}}{\Delta\omega}. \tag{2.8}$$

In X-ray science the spectral bandwidth is more often expressed in terms of the energy resolution $\Delta E/E = \Delta\lambda/\lambda$, where the ΔE is the full width at half maximum (FWHM) of the power spectrum. Taking into account that $\Delta\omega = 2\pi c\Delta\lambda/\lambda^2$, we obtain the equation for the longitudinal coherence length [51]

$$L_l = c\Delta\tau_c = \sqrt{\frac{2\ln 2}{\pi}}\frac{\lambda^2}{\Delta\lambda} \approx 0.664\frac{\lambda^2}{\Delta\lambda}. \tag{2.9}$$

The more narrow is the spectral bandwidth the more is the temporal coherence. At experimental stations of synchrotron the temporal coherence properties of X-ray beam is determined by energy resolution of the monochromator. For example, in the experiments which will be described in Chapter 5 we used the high-resolution Si(111) double crystal monochromator. At $8\,\text{keV}$ of the photon energy that provides about 10^{-4} of the energy resolution. For this number, the formula (2.9) yields approximately $1\,\mu\text{m}$ of the longitudinal coherence length. In the coherent X-ray diffraction experiment that means the high contrast diffraction pattern can be obtained only if the object size does not exceed this value in the longitudinal dimension.

The estimates for the vertical and horizontal transverse coherence lengths can be obtained

from the formula (2.6). The end station at the P10 beamline is located 90 m from the undulator. A typical size of the electron beam is 6 µm in vertical and 36 µm in horizontal directions, that can be considered as the source size. For 8 keV of photon energy ($\lambda = 1.55$ Å) the equation (2.6) yields 360 µm and 60 µm of coherence length in vertical and horizontal directions correspondingly. That is equal to 91 % and 2 % from the beam size which is 390×2520 µm. If the experiment requires a higher degree of transverse coherence the coherent fraction of the beam can be selected by the collimating slits. As a result, a narrow beam which can be considered as almost fully coherent on the size of the beam is obtained. At the same time, that leads to a decrease of total flux since the substantial part of the beam is cut off.

2.2 CXDI on non-crystallographic objects

In the conventional visible light microscope the magnified image of the object is produced by combination of the refractive lenses. That allows to achieve resolution [7] close to the Abbe diffraction limit Δ, established by [25]

$$\Delta = \frac{0.61\lambda}{n \sin\theta}. \tag{2.10}$$

Here n is the refractive index of the medium and θ is half the angle subtended by the objective lens. The larger the aperture of the lens, and the smaller the wavelength, the finer the resolution of an imaging system. Considering green light around 500 nm wavelength and a numerical aperture $n \sin\theta$ of 1, the Abbe limit can be estimated as roughly 300 nm.

To increase the resolution, the radiation of shorter wavelengths, such us ultraviolet and X-rays can be used. X-ray microscopes offer up to 12 nm of resolution [52, 53] but are suffer from lack of contrast. In addition, available focusing elements of X-ray optics, such as Kirkpatrick-Baez (KB) mirrors [54], compound refractive lenses (CRL) [55] and Fresnel zone plates (FZP) [56] do not allow to achieve high magnification and efficiency comparable with the those in optics of the visible light. However, there is an alternative approach that can produce high-resolution image of a sample without using any optics on the way to detector. Methods of Coherent X-Ray Diffractive Imaging (CXDI) [57, 58] exploit diffraction data from coherently illuminated specimen and reconstruct the sample image relying on the relationship between the wave field in the object plane and detector plane. More specifically, the complex amplitude of the wave field on the exit surface of the object is reconstructed.

There are two distinguished concepts of experimental realization of these methods [8]. First one is based on the forward scattering where the diffraction pattern is recorded by a two-dimensional (2D) detector positioned in the transmission geometry (see Figure 2.2). This approach is typically used for imaging of non-crystalline objects. Distinct to that, the second concept exploits the Bragg geometry where a crystalline sample is oriented to satisfy the Bragg

[7] The smallest distance at which two points can still be uniquely resolved.

[8] In this thesis we do not discuss the Grazing Incidence Small Angle X-ray Scattering methods.

condition and the detector records the scattered intensity in the vicinity of the selected Bragg peak. This section will focus on the CXDI in the transmission geometry, while the Bragg CXDI will be discussed next section.

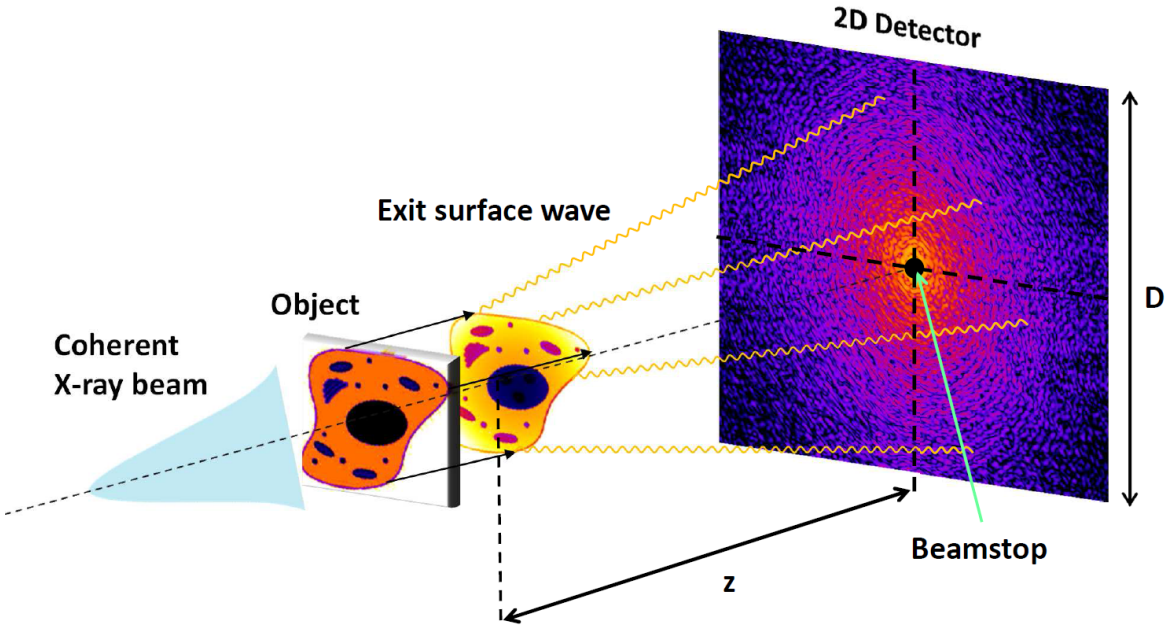

Figure 2.2: The concept of a coherent X-ray scattering experiment in case of a non-crystallographic object. A coherent X-ray beam illuminates the sample producing the modulations in the wave field on the exit surface. The diffraction pattern is measured under far-field conditions by a two-dimensional detector, protected from the direct beam with the beamstop.

Figure 2.2 illustrates the general principles of a coherent X-ray diffraction experiment with a non-crystallographic sample. A coherent beam is incident on the sample and results in two-dimensional diffraction pattern on the detector, positioned at distance z downstream in the far-field. In order to block the direct beam, which is usually much brighter than the scattered signal and can damage the detector, a beamstop may be used. By back-propagation to the object plane one retrieves the two dimensional complex amplitude of the exit surface of the sample. Generally speaking, the propagation through the free space, which establishes the relationship between the wave fields in the object plane and detector plane, is done by integration of the point source function over the irradiating surface [59]. However, conventional CXDI schemes assume the detector to be located in the far-field which allows to reduce this integral to a simply Fourier transformation. On the other hand, if the sample is thin and weakly diffracting, the projection approximation is valid. According to that, the exit surface wave (ESW) is a product of the incident illumination function and the projection of the refraction coefficient, given by the equation (1.30). Therefore, the reconstruction of the ESW provides full information about projected electron density, if the illumination function is known *a priori* or can be determined by the reconstruction, as in ptychography [60].

The concept of the projection approximation can also be conveniently described in terms of basics of kinematical theory of X-ray diffraction. According to this theory, a two-dimensional

diffraction pattern measured in the far-field corresponds to the cross-section in reciprocal space which contains information about electron density distribution of the scattering object. Generally speaking, that cross-section in reciprocal space is described by the Ewald sphere. However, in many practical cases the curvature of the part subtended by the detector is small. When the full detector side length D is much smaller than the sample-to-dectector distance z, the small angle approximation

$$\sin\left(\frac{D}{2z}\right) \approx \frac{D}{2z} \tag{2.11}$$

is valid and the subtended part of the Ewald sphere can be considered as being flat. Consequently the scattering vector can be approximated by

$$\mathbf{Q} = \frac{2\pi}{\lambda}[\frac{x}{z}, \frac{y}{z}, 0], \tag{2.12}$$

where x and y are coordinates in the detector plane. From the basic properties of Fourier transformation a two-dimensional amplitude distribution $A(q_x, q_y, q_z = 0)$ within this flat reciprocal space cross-section corresponds to the projection of the object in real space on the xy-plane. By collecting diffraction patterns at different orientations of the sample the whole reciprocal space can be measured and thus the CXDI method is extended to three dimensions so that

$$A(\mathbf{q}) \propto \int \rho(\mathbf{r}) e^{i\mathbf{q}\cdot\mathbf{r}} d\mathbf{r}. \tag{2.13}$$

Here $\rho(\mathbf{r})$ denotes electron density distribution in real space.

Since the diffraction image recorded by a detector represents discrete intensity distribution with a certain pixel size, the recovery of the scattering object requires sufficient sampling criterion. In essence, it is based on the Nyquist-Shannon-Kotelnikov sampling theorem [61, 62]. It states that a band-limited analog signal that has been sampled can be perfectly reconstructed from an infinite sequence of samples if the sampling rate exceeds 2 samples per period of the highest frequency in the original signal. In imaging that means that to recover a feature of size Δl the corresponding fringes in reciprocal space has to be sampled with at least two pixels per interference fringe. In other words the resolution in reciprocal space must not fall below $\Delta q = \pi/\Delta l$. In addition, from the sampling theorem it follows that the achievable resolution in real space is theoretically limited by the highest measured spatial frequencies and therefore can be calculated from the detector size as

$$\Delta x = \frac{\lambda z}{D}. \tag{2.14}$$

In practical cases, however, the effective resolution depends on the biggest scattering angle where a significant signal can be measured, which in its turn depend on the scattering ability of the specimen and the detector efficiency. Unfortunately, in many cases the lower signal can not be simply compensated by the longer exposure, since the atomic structures can only withstand a limited dose before they are destroyed. This effect is called radiation damage and occurs

already at low and medium doses in case of biological materials consisting of large molecules with weak chemical bonds and predominantly light elements [63].

2.3 Bragg CXDI

The concept of the Bragg CXDI relies on the Bragg diffraction and this method is intended for imaging of crystalline samples. Typical geometry of the Bragg CXDI experiment is shown in Figure 2.3.

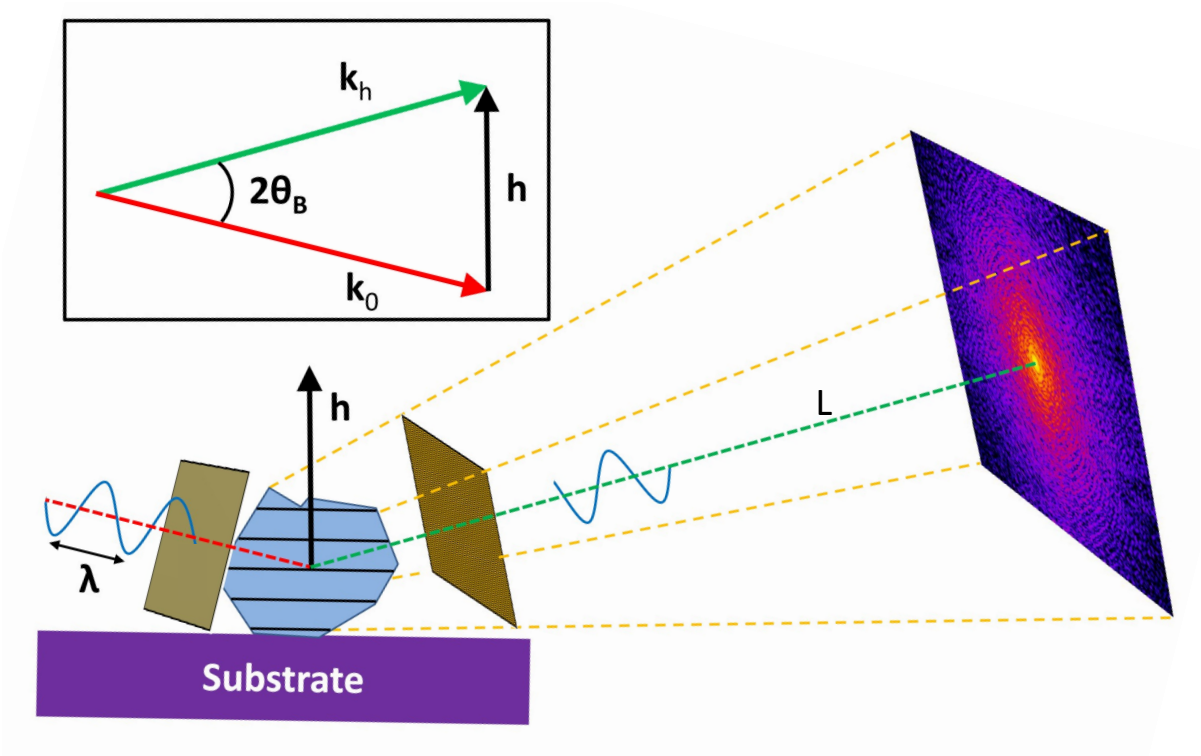

Figure 2.3: Coherent X-ray Diffractive Imaging experiment in the Bragg geometry. A crystalline sample is fully illuminated by coherent X-ray beam with the wave vector $\mathbf{k}_0$ and wavelength λ. The orientation of the crystal is assumed to fulfill the Bragg condition for the reflection with reciprocal lattice vector $\mathbf{h}$. The diffracted wave propagates in the direction of the wave vector $\mathbf{k}_h = \mathbf{k}_0 + \mathbf{h}$ as it is shown in the inset. The resulted diffraction pattern is recorded by a 2D detector positioned in the far-field at distance L and contains the selected Bragg peak and surrounding speckles.

Let us consider a finite crystal with its shape described by the function $s(\mathbf{r})$. The crystal is fully illuminated by a monochromatic beam with the complex amplitude $E_0(\mathbf{r})$ and the orientation of the crystal is chosen to satisfy the Bragg condition for selected crystallographic planes. The diffracted signal is recorded by a two-dimensional detector positioned in the far-field at distance L. In reciprocal space the position of each pixel on the detector can be described by the scattering vector $\mathbf{q}$. By integrating the second equation in the set of equations (1.39) and propagating the results to the far-field, the following expression for the scattered amplitude $A(\mathbf{q})$ can

be obtained [32]

$$A(\mathbf{q}) = -r_0 F_h \frac{(2\pi)^3}{V_{uc}} \frac{e^{i\omega L/c}}{L} \int E_0(\mathbf{r}) s(\mathbf{r}) e^{-i\mathbf{h}\cdot\mathbf{u}} e^{-i(\mathbf{q}-\mathbf{h})\cdot\mathbf{r}} d\mathbf{r}. \tag{2.15}$$

Here F_h denotes the structure factor. According to this equation, the intensity distribution around each of the Bragg reflections is given by the Fourier transform of the electron density distribution of the crystalline part of the sample, if the illumination function remains constant over the whole crystal. In the case of a perfect crystal this intensity distribution function is central symmetric with respect to the specific lattice node. However, in the presence of a displacement field such a symmetry breaks. By varying the angular position of the crystal around the Bragg angle different points of the reciprocal space can be reached. By stitching the collected diffraction patterns, a three-dimensional reciprocal space map in the vicinity of selected reflection is constructed. The inversion of it into real space as a result gives the three-dimensional object function [29]. As it follows from the equation (2.15) the amplitude of this function describes the shape of the crystalline part of the sample and the phase $-\mathbf{h}\cdot\mathbf{u}$ corresponds to the projection of the displacement field on the reciprocal lattice vector. This relation is widely used in coherent X-ray diffraction imaging methods, in particular, for a mapping of a deformation field inside of three-dimensional nanocrystals [32, 33, 34]. As far as optical and electrical properties of the crystal depend on the local strain such methods are of importance in the design and implementation of functional nanocrystalline materials [64].

Distinct to the forward scattering geometry, the scheme of the Bragg CXDI assumes the measurements of intensities at higher scattering angles ($2\theta_B$). In consequence, the parasitic contribution from the direct beam is eliminated and the diffraction pattern can be recorded without using beamstop. In addition, due to the constructive interference the scattered signal is enhanced in a narrow solid angle, which allows to separate it from the background signal which comes from the substrate or other crystalline particles if several of them are illuminated simultaneously.

2.4 Small Angle – Bragg Coherent X-ray Diffraction Imaging

The resolution in the diffractive imaging experiments is fundamentally limited by the highest scattered angles at which a significant signal can be measured. The substantial constructive interference which appears in case of ordered structures, such as crystals, can be used to increase the amount of recorded information in many times. However, to merge together the scattered intensities measured in the vicinity of different reciprocal lattice nodes the relative phases of all the Bragg reflections are required. This problem can be overcome by some *a priori* knowledge about the structure as it is commonly done in the protein crystallography [37], or by a phase retrieval approach that uses the interference pattern formed with contributions from neighboring

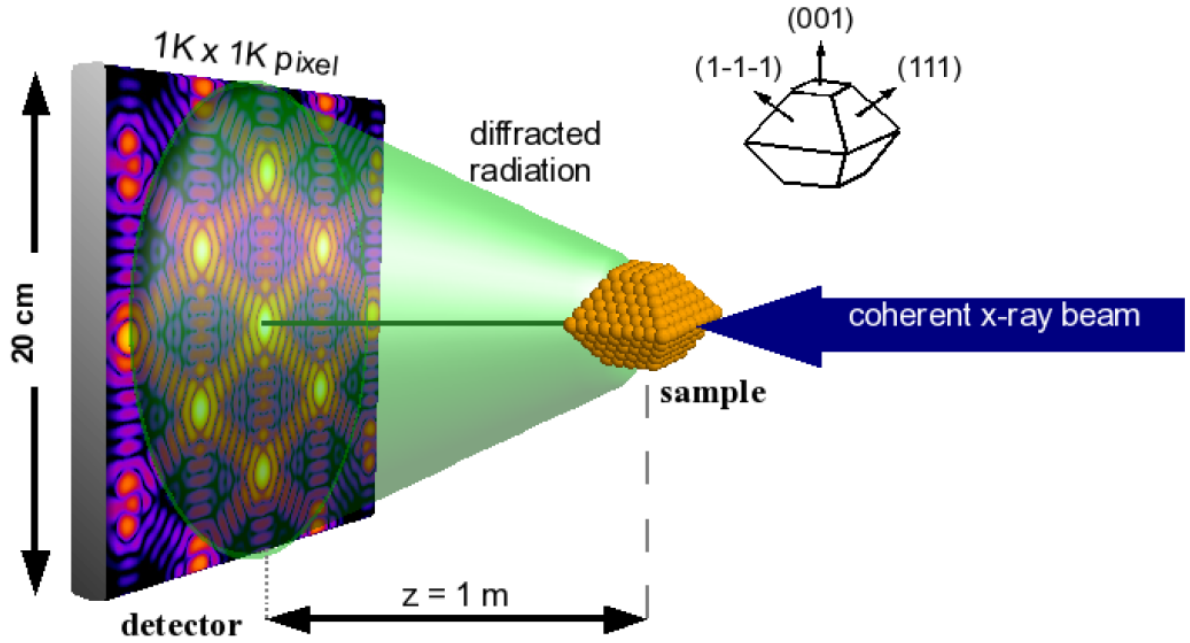

Figure 2.4: The model parameters used for the simulations demonstrated in [66]. A 6 nm Pd nanocrystal with a shape restricted by {111} side facets was located one meter upstream of the detector. The direction of the incident beam of 100 keV of photon energy was taken along the [100] crystallographic direction. (Figure was adopted from Reference [66].)

reflections. This idea was proposed by Sayre more than half a century ago in work [65], where he suggested to phase crystallographic data by measuring information between the Bragg peaks in reciprocal space. Such a method was later termed an oversampling method in contrast to conventional sampling at Bragg peaks in crystallography. In this approach the inversion of the coherent diffraction pattern containing several Bragg peaks gives the positions of individual scatterers in the crystalline structure. In other words, the geometry of such an experiment assumes a Small-Angle and Bragg CXDI measurements performed simultaneously. Potentially, this approach can be applied for three-dimensional imaging of internal structure of crystalline samples. The full crystallographic data opens a way to reconstruct both the crystal shape and the positions of individual scatterers with atomic resolution. This approach was developed earlier in Reference [66], where the coherent high-energy X-ray beam was proposed to map several Bragg peaks on a single detector (see Figure 2.4). As one of the important experimental parameters, the incoming photon flux, required for successful reconstruction of the structure of Pd nanoislands with atomic resolution was estimated.

Although these ideas were successfully demonstrated in the electron microscopy [67, 68, 69], the realization of such an experiment with atomic structures and high-energy X-rays is rather challenging, because of lack of the scattered signal. On the other hand, instead of going for higher energies a crystal with a larger unit cell can be imaged. A notable example was presented in [70] where 2D structure of a colloidal crystal was reconstructed. The positions of individual particles as well as the lattice defects have been revealed by this approach. In the Reference [71] it was suggested to extend this approach to three-dimensions. Using azimuthal

rotation scans the 3D scattered intensity from an isolated colloidal crystal grain in the far-field was measured. It included several Bragg peaks as well as the coherent interference speckles around these peaks. Although this approach was demonstrated by authors in modeling at that time it was not possible to perform the 3D reconstruction of measured data owing to experimental challenges. In the present work a successful experimental demonstration of described approach.

2.5 Phase retrieval algorithms

In general case the scattered amplitude $A(\mathbf{q})$ is a complex function, therefore the transformation of it into real space requires knowledge of both the real and imaginary components. If the diffraction data are sufficiently sampled with N independent measurements in reciprocal space, the reconstruction of the object function is represented by a vector in $2N$-dimensional space will require $2N$ image coefficients. However, the measurement always yields the squared modulus of the scattered amplitudes, which provides only N coefficients and all the phase information set by the other N coefficients is not available, what is known as the phase problem [25]. Utilizing some *a priori* knowledge as additional constraints it is possible to reduce the number of unknown variables substantially and retrieve the phases through iterative algorithms [72]. Propagating the measured amplitudes backward to the sample plane and again to the detector iteratively such algorithms successively apply the constraint operators. The result is that the reconstruction converges to the image which fulfills the constraints and whose Fourier spectrum matches the measurement. Originally proposed by Gerchberg and Saxton [73] and later brought into practice by Fienup [74], the phase retrieval approach over the decades has been developed into several numerical methods [75]. Being a very dynamic field it is rapidly becoming an invaluable imaging tool in short wavelength microscopy because it circumvents the limitations of X-ray and electron lenses, such as low efficiency, small numerical aperture, or presence of aberrations.

2.5.1 Error Reduction and Hybrid input-output algorithms

In Figure 2.5 the principles of conventional scheme of the phase retrieval algorithm are shown schematically. Starting with the measured intensities $I(\mathbf{q}) = |A(\mathbf{q})|^2$ the iterative process aims to recover the entire complex wave field

$$A(\mathbf{q}) = |A(\mathbf{q})|e^{i\phi(\mathbf{q})}, \tag{2.16}$$

where only the amplitude is known from the measurement. Initially, the algorithm is seeded by a set of random phases $\phi_1(\mathbf{q})$ assigned to the measured amplitudes which is called the *first guess*

$$A_1(\mathbf{q}) = \sqrt{I(\mathbf{q})}e^{i\phi_1(\mathbf{q})}. \tag{2.17}$$

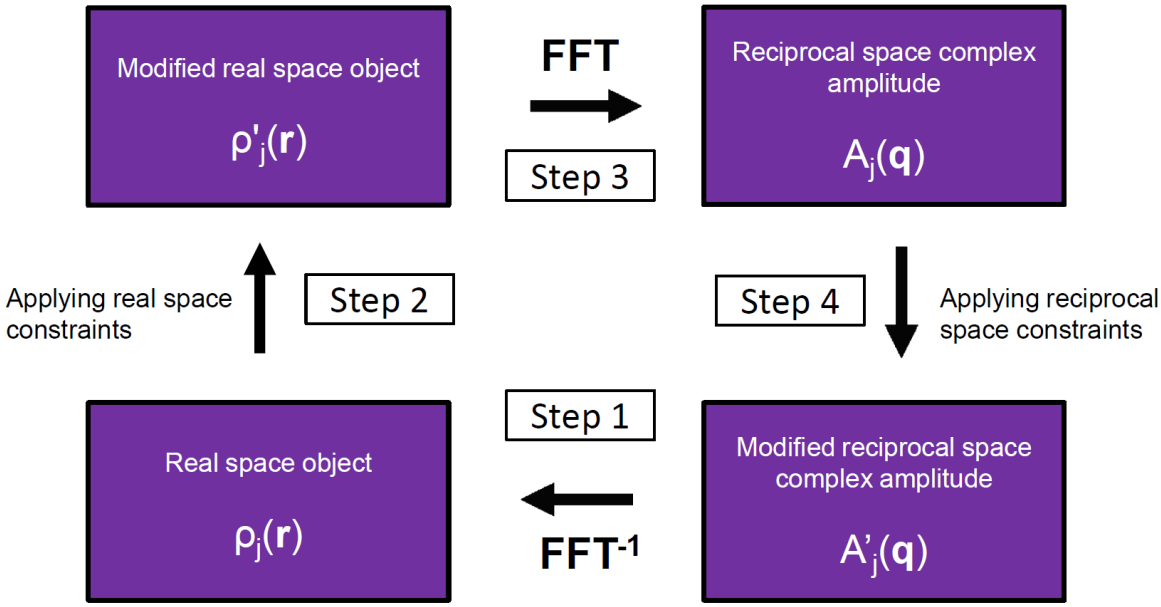

Figure 2.5: Four steps of the iterative phase retrieval algorithm. In order to compute the discrete Fourier transform and its inverse a numerical algorithm of Fast Fourier Transform (FFT) is typically used.

Step 1 of the iteration yields the *first guess* of the image in real space $\rho_1(\mathbf{r})$ formed by an inverse Fourier transform

$$\rho_1(\mathbf{r}) = \mathrm{FFT}^{-1}[A_1(\mathbf{q})]. \tag{2.18}$$

The constraint in real space which is applied in the Step 2 uses the information that the object is isolated and of finite size. Defining the support S as the area where the electron density may take non-zero values, the most simple operator of this constraint can be expressed as

$$\rho'(\mathbf{r}) = \begin{cases} \rho(\mathbf{r}), & \text{if } x \in S \\ 0, & \text{otherwise,} \end{cases} \tag{2.19}$$

where the $\rho(\mathbf{r})$ is the input and the $\rho'(\mathbf{r})$ is the output. As a consequence of this modification, the result of the direct Fourier transform of the output (Step 3) will be distinct from the initial reciprocal space amplitudes. Closing the cycle the obtained phases $\phi_2(\mathbf{q})$ are multiplied with the measured amplitudes in the Step 4 yielding the updated complex wave field or the *second guess*

$$A'_2(\mathbf{q}) = \sqrt{I(\mathbf{q})}e^{i\phi_2(\mathbf{q})}. \tag{2.20}$$

These four steps are repeated for a finite number of iterations converging to a valid solution. The algorithm based on the operator (2.19) is known as Error Reduction (ER) algorithm since the error metrics, describing how well the modulus and support constraint are satisfied, always decrease after applying the operator. As a result the algorithm converges fast but without any chance to escape from local minima, which would require a step that increases these metrics. In order to improve the performance of the phase retrieval procedure more sophisticated con-

straints in real space can be applied. Without the aim to provide a full overview, below we give a description of the most common techniques which were successfully used in the present studies.

The stagnation problem can be overcame with the hybrid input-output (HIO) algorithm [74], which uses the output from the previous iterate to update the current one according to the rule

$$\rho'_j(\mathbf{r}) = \begin{cases} \rho_j(\mathbf{r}), & \text{if } x \in S \\ \rho_j(\mathbf{r}) - \beta\rho_{j-1}(\mathbf{r}), & \text{otherwise.} \end{cases} \tag{2.21}$$

The amount of feedback is controlled by the real constant β which is in the range of 0 to 1, the best results are typically achieved with $\beta = 0.8$ [74, 76]. The inspiration for this algorithm comes from control theory, with the idea to provide a negative feedback to the operation. Since the HIO is tolerable to nonzero amplitudes outside the support it is practically useful to perform several iterations of ER between HIO steps. The ER algorithm refines the result of the HIO algorithm, which in its turn helps to avoid stagnation in local minima. There are many other modifications of these algorithms which improve the convergence rate by taking bigger steps in image space or alternating the search strategy, as explained and reviewed by Marchesini [75].

A particular one, known as the Guided Hybrid Input-Output (GHIO) method [77], worth to be introduced here because it was used in the studies, which will be presented in Chapter 5. Taking advantage of the fact that typically several reconstructions are run in parallel to verify a reliability of obtained result, this algorithm divides the reconstruction procedure into several stages, or generations g, where the mean of best results is used to seed a subsequent generation. As a first step, N processes which have been independently seeded with random phases are started. The reconstruction with the best error metrics is selected as a template of this zeroth generation $\rho^{g=0,n}(\mathbf{r})$, where $n = 1, 2, .., N$ is the sequence number of the run. To start the next generation, each of the processes is seeded through the expression

$$\rho^{g+1,n}(\mathbf{r}) = \sqrt{\rho^{g,template}(\mathbf{r}) \times \rho^{g,n}(\mathbf{r})}. \tag{2.22}$$

After running all N reconstructions in parallel again the best result is chosen as a template for the subsequent generation, and this process is repeated several times until the desired convergence criteria is met.

2.5.2 Shrinkwrap method

The implementation of HIO and GHIO algorithms might significantly improve the convergence rate and robustness of the phase retrieval method. At the same time the obtained solution strongly depends on how close the chosen support fits the actual object. Only a limited number of solutions will satisfy the constraint of a very tight support which helps the algorithm to converge, and in that way the real space support is a key parameter in the reconstruction procedure. In addition to the support constraints, the so-called positivity constraint, might be applied at

each of the iterations requiring the object function to be real and positive. However, in many particular cases the phase cannot be considered as being flat over the object, and consequently the density function is complex valued. In particular that occurs with soft X-rays (photon energies below $1\,\mathrm{keV}$), where refraction effects play a significant role. In this case, knowledge of actual boundary of the object is imperative, since with a loose of support an out-of-focus image would be a valid solution either.

This problem can be overcome by using the dynamic support which updates occasionally from the estimate of the object based on the current reconstruction. Originally proposed by Marchesini [78], the so-called Shrinkwrap method starts with a support which is derived from the autocorrelation function or might be even chosen arbitrary. Every 20–50 iterations a new support is deduced from the current reconstruction, that had been preliminary smeared by a convolution with a Gaussian function in order to avoid artifacts. Image pixels below a certain threshold (typically about 10–20%) are treated as being outside the object. When the reconstruction progresses the support tends to gradually shrink to the boundary of the actual object. At some point a stop criteria must be added to avoid over shrinking. The Shrinkwrap method does not work for objects with smooth edges, where the real space density slowly falls off to zero. It also has problems with objects, that has vacancies, since the algorithm stimulate growth of the holes. Nevertheless, this method can substantially facilitate the reconstruction process in most of usual cases.

In many experimental situations, the ratio between the intensities at lowest and highest scattering angles is very high and might exceed the dynamic range of the detector. In order to avoid oversaturation the zero-order beam is usually suppressed or dumped by a beam stop or a hole in the detector, which results in a region of missing data. When only a support constraint is applied, there will be particular modes that are neither constrained by the diffraction measurement nor the support [79]. If the region of missing data is larger than the size of a single speckle, which corresponds to the object's dimension in real space, the important part of the information is lost and the iterative algorithm may fail. When the reconstruction progresses the missing intensities tend to grow unconstrained and become dominating. In some cases it is, however, possible to achieve successful reconstruction applying some restraining rule which suppresses them down to some normalization value calculated using a high-pass filter [80]. The missing data issue can also be overcame in dark-field Coherent Diffraction Imaging [81, 82].

2.5.3 Uniqueness and resolution

A very important aspect of iterative algorithms is the uniqueness of the obtained solution. Beside the fact that the phases are reconstructed up to a constant, the general properties of the Fourier transformation give three possible real space solutions. If the correct solution is described by $\rho(\mathbf{r})$, the shifted object $\rho(\mathbf{r}+\Delta\mathbf{r})$ as well as the inverted complex conjugated one $\rho^*(-\mathbf{r})$, so called twin image, also have the same modulus of the Fourier transform. The appearance of the displaced object can be easily avoided by utilizing a support which is tight

enough to localize the object in real space. For not very symmetric objects the twin image can be suppressed by using an asymmetric support, which pushes the reconstruction towards one solution. However, in the presence of symmetry in the object density function the equivalent solutions which fulfill both the modulus and support constraints might appear. It has been shown that a number of such solutions primarily depends on the dimensionality of the dataset [83]. Being nearly always unique in the three-dimensional case, the reconstruction can reveal other solutions in some special 2D cases, and generally have a few of them for one dimension. In a summary, except for rare not ordinary cases the phase retrieval algorithms always converge to the unique correct solution.

Due to different reasons like presence of noise or missing area in the experimental data a single true solution cannot be distinguished from a family of images that satisfy all constraints within the errors. The common way to estimate the best image is to calculate the average $\overline{\rho}(\mathbf{r}) = \langle \rho_i(\mathbf{r}) \rangle$ over the number of runs, which have been independently seeded by sets of random phases. The ratio of the modulus of the scattering amplitude determined from this average and the square root of measured diffraction intensity is known as the phase retrieval transfer function (PRTF)

$$\mathrm{PRTF}(\mathbf{q}) = \frac{|\mathrm{FFT}[\overline{\rho}(\mathbf{r})]|}{\sqrt{I_M(\mathbf{q})}}. \tag{2.23}$$

The obtained value of this function at each pixel or voxel is in the range of 0 to 1 and tends to decrease with increasing the resolution due to the fact that the signal at higher scattering angles is more influenced by noise. Therefore it appears to be a good way to determine the actual resolution in the reconstruction from the PRTF function.

Successful reconstruction depends on the number of the algorithm's parameters which can differ and has to be chosen manually for each dataset. In some practical cases the presence of noise and parasitic scattering in the experimental data, the detector gaps or effects of incoherence can make the reconstruction procedure extremely complicated and even unreliable. Nevertheless, being a dynamically developed field phase retrieval algorithms suggest a powerful tool for visualization of internal structure of micro- and nanoscopic samples [57].

2.5.4 Ptychography and other algorithms

For the sake of completeness other phase retrieval methods, that have not been used in the present work, should be mentioned. The conventional scheme of the Coherent Diffractive Imaging is limited to isolated objects or pre-characterized finite illumination functions. These shortcomings could be overcome by ptychography, that employs a set of diffraction patterns generated from overlapping illuminated regions of the specimen [84]. Redundant information about the common area is used as an additional constraint in real space which is applied on each iteration. The reconstruction of all scan points on the sample is performed simultaneously looping over all the scan positions (see Figure 2.6). The overlap ratio and number of diffraction patterns determines the redundancy of the ptychographic dataset, when compared to other

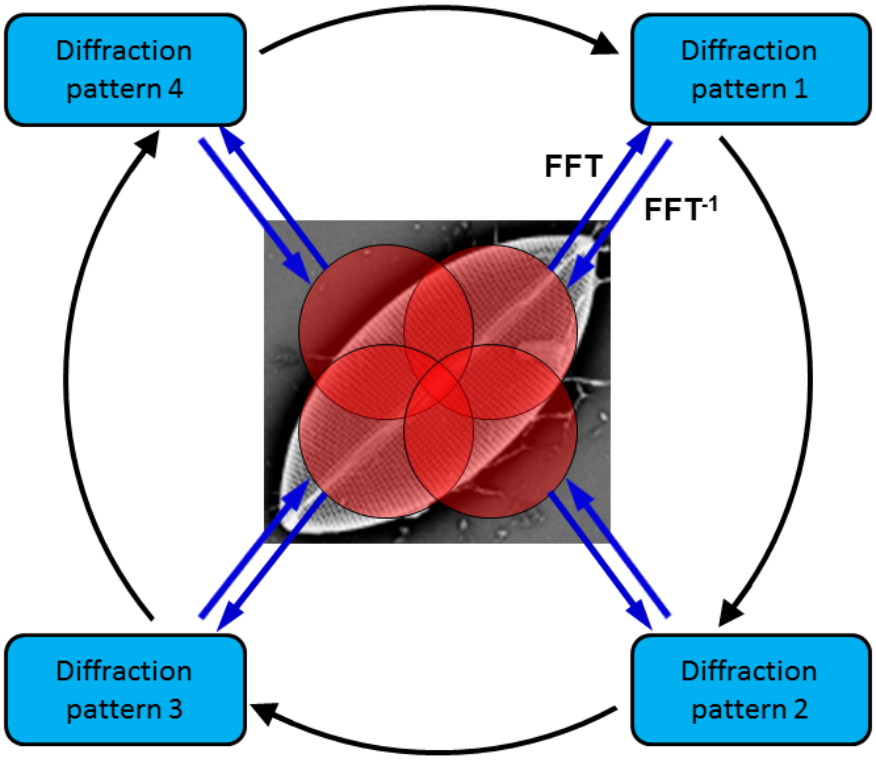

Figure 2.6: Schematic diagram of the ptychographical iterative algorithm. The outer circle outlines the big loop over all scan positions on the sample. The double arrows represent a single update of one position during one full iteration of the classical phase retrieval routine.

imaging methods that employ only a single diffraction pattern.

There are, basically, two types of iterative ptychographic algorithms called the Ptychographic Iterative Engine (PIE) and extended Ptychographic Iterative Engine (ePIE). The PIE algorithm requires *a priori* knowledge of the illumination, whereas the ePIE algorithm retrieves it by refining the initial guess. The first successful demonstrations of applying the PIE algorithm in X-ray regime revealed extremely fast and robust convergence [85, 86, 87]. One of the most remarkable results has been the three dimensional reconstruction of bone structure [88], where a high contrast bone density map was reconstructed with a resolution of 100 nm. An additional great advantage of ptychographical approach is the automatic reconstruction of the illumination function if the ePIE algorithm is used. That yields a detailed quantitative picture of the complex wave field, and provides a fast, robust and powerful tool for the beam characterization with high spatial resolution and dynamic range [60].

Another imaging technique, which allows to get rid of the restriction of the isolated sample is called Fresnel CDI [89]. While the classical scheme of CDI, described above, assumes the flat illumination phase, which is typically achieved by localizing the sample in the focal plane, the Fresnel CDI suggests to place the sample at a small distance downstream. That allows the divergent beam to carry additional information, which assists in the reconstruction routine. However, these favorable effects can be exploited only if the illumination phase is well characterized. The first experimental realization [90] revealed accelerated convergence compared to

plane illumination and later it was shown that Fresnel CDI is more robust in the case of partial coherence when compared to plane wave illumination [91, 92]. Allowing to image parts of objects, embedded within a larger entity, this method can also be combined with scanning techniques e.g. ptychography.

The last coherent diffraction imaging technique that has to be mentioned here is X-ray holography. This method addresses the phase problem by coherent interference of a wave diffracted by the object with some reference wave. In most practical cases the reference scatterer is represented by an aperture which is located in the same plane as the object [93]. The phase of the object wave gets encoded by the reference wave in the combined intensity distribution in the far-field which itself is captured by a detector. Due to the fact, that a simple back Fourier transform of the diffraction pattern reveals the object, this method is known as Fourier Transform Holography (FTH) [93, 94]. A very simple and straightforward way of reconstruction, as well as robustness, are the advantages of this method that meets, however, rather strict experimental constraints. The reference scatterer has to be positioned further away than the lateral dimensions of the object [9], therefore a high degree of coherence is required to get an interference pattern [95]. In addition, the diffracted intensities from the reference scatterer have to be of similar magnitude as the scattered intensities from the object [96]. The last condition limits the size of the reference scatterer below, and consequently, the achievable resolution.

[9] More specifically, the distance between the reference source and the nearest edge of the object must exceed the maximal lateral dimension of the object.

Chapter 3

Dynamical effects in Coherent X-ray Diffractive Imaging

A wide variety of Coherent Diffractive Imaging methods rely on the kinematical approximation, which is based on the assumption that each photon scatters only once in the material. This leads to considerable simplification in the interpretation of the experimental results. In particular, the real space density distribution is connected to the far-field scattered amplitude by the Fourier transformation. That serves as the foundational relationship for the majority of the X-ray diffraction methods, such as SAXS, CXDI, ptychography, Fourier Transform holography etc.

As it was shown in pioneering work on Bragg CXDI [97, 32, 98, 33] Bragg diffraction can be used for the mapping of the deformation field inside of three-dimensional nanocrystals. In this method the 3D complex density function of a nanocrystal is reconstructed from the reciprocal space dataset measured in the vicinity of a Bragg reflection. According to the kinematical theory the magnitude of that density function is proportional to the continuous electron density distribution of the crystalline part of the object and the phase is related to the projection of the local deformation field on the reciprocal lattice vector [29]. However, if the size of the crystal is comparable to the extinction length, the cross-coupling between the diffracted and the transmitted waves becomes significant and can give rise to artifacts in the reconstruction. In general, the refraction and absorption might also play a considerable role in the diffraction process. All these effects can be taken into account consistently by the dynamical theory. This theory has been extensively developed already for decades [27], however, the influence of the dynamical effects on the results of the Bragg CXDI has not been studied yet.

In order to investigate this problem in details we performed a series of simulations of the scattered wave field around a specific Bragg reflection using the dynamical approach. Results of the inversion of the simulated dataset to real space reveal the character of the artifacts, introduced by the dynamical diffraction. This chapter will cover the theoretical aspects of the model, the detailed analysis of the simulations and a comparison with the kinematical theory. Special attention will be paid to ways of correction of the results of real experiments in order to prevent

appearance of such artifacts in a reconstruction.

3.1 Model description

Let us consider a typical geometry of a Bragg CXDI experiment with an isolated crystalline object fully illuminated by a monochromatic X-ray beam. The orientation of the crystal fulfills the Bragg condition for the selected wavelength and the diffracted intensities are recorded by a two-dimensional detector located in the far-field. 3D reciprocal space data are measured by a series of diffraction patterns in which the incidence angle of the beam is varied by a fraction of a degree in the region of the Bragg angle (see Figure 3.1). Experimentally, the angular scan is

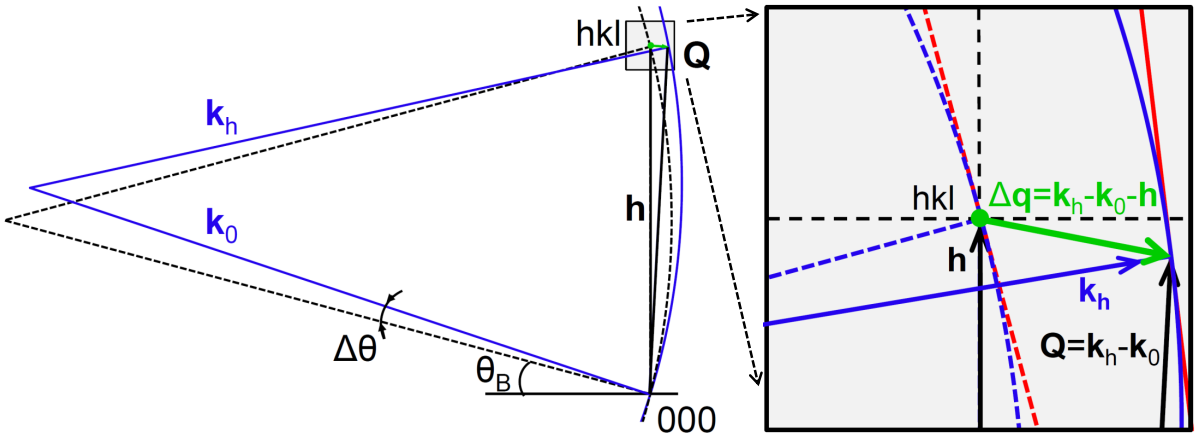

Figure 3.1: A schematic view of 3D reciprocal space covered by a rocking scan. The real measurement yields the diffraction pattern that corresponds to the spherical surface in reciprocal space described by the Ewald sphere (shown by blue color), while the simulated one is attributed to a flat surface (shown by red color).

performed by a rotation of the sample in the scattering plane, while the positions of the incident beam and the detector are fixed. Figure 3.1 schematically shows how the diffraction patterns are merged in reciprocal space. When the Bragg condition is fulfilled ($\theta = \theta_B$) the two-dimensional surface in reciprocal space that corresponds to the recorded image is crossing the reciprocal lattice node hkl. For certainty let us assume that the central point of the detector coincides with the center of the Bragg peak. When the crystal is rotated by a small angular deviation $\Delta\theta = \theta - \theta_B$, the triangle formed by wave vectors $\mathbf{k}_0$, $\mathbf{k}_h$ and scattering vector $\mathbf{Q} = \mathbf{k}_h - \mathbf{k}_0$ is rotated by the same value $\Delta\theta$ around the origin of reciprocal space 000. According to that the position of the cross section in reciprocal space is changed by the same transformation of rotation. Then, the position of the central point on the detector in reciprocal space will be shifted for the vector $\Delta\mathbf{q} = \mathbf{Q} - \mathbf{h} = \mathbf{k}_h - \mathbf{k}_0 - \mathbf{h}$ as ishown in Figure 3.1. From the geometry it follows that the length of this vector is $|\Delta q| = 2h\sin(\Delta\theta/2)$.

In our model we use the laboratory coordinate system where the orientation of the beam is static during the angular scan but the sample is rotating. The origin is chosen on the axis of the crystal rotation. In this coordinate system the orientation of the reciprocal lattice vector depends

on the angular position of the crystal θ. For the sake of shortness it will be referred as $\mathbf{h}$ in the following, meaning that in laboratory coordinate system this vector is a function of the angular deviation $\Delta\theta_B$.

We generally assume the two-beam diffraction case and a perfect or weakly deformed finite size crystal [10]. The set of Takagi-Taupin equations [45, 46] supplemented by the boundary conditions is used to propagate the complex electric field through the whole three-dimensional crystal. For each angular position the two-dimensional distribution of a complex amplitude of the diffracted wave is obtained at the exit surface. Results of the propagation of this wave field from the exit surface to the far-field yields the simulated diffraction pattern. As far as the phase information is included, the resulted 3D reciprocal space dataset can be directly inverted to real space, without iterative phase retrieval procedure. The characterization of dynamical artifacts in real space is performed by a comparison of the output with the original object function.

An analytical solution of Takagi-Taupin equations is nontrivial and can be performed for a few specific cases only. For example, such a solution is known in the case of a crystal plate finite in one dimension, but infinite in two others [27]. The methods for numerical integration in the two-dimensional case for a few certain geometrical shapes were developed in the References [99, 100, 101, 102]. Here we offer a more general approach, based on a modification of the Takagi-Taupin equations aimed to facilitate a numerical solution in a finite three-dimensional crystal of almost any shape in the presence of deformations.

3.2 Modifications of the Takagi-Taupin equations

Commonly, the Takagi-Taupin equations are used in the form (1.36), where the space derivatives are taken along directions of the wave vectors $\mathbf{k}_0$ and $\mathbf{k}_0 + \mathbf{h}$. After the propagation, the total electric field at the exit surface can be obtained by multiplying the resulted complex amplitudes $E_0(\mathbf{r})$ and $E_h(\mathbf{r})$ by the corresponding phase exponents $\exp(i\mathbf{k}_0 \cdot \mathbf{r})$ and $\exp(i\mathbf{k}_0 \cdot \mathbf{r} + i\mathbf{h} \cdot \mathbf{r})$ (see expression (1.35)). In most cases only the relative phase between the wave field components E_0 and E_h is important, which makes it sufficient to determine the phase distribution up to a constant. However, if the angular scan is performed the phase exponents cannot be omitted because the results of the scalar products in the exponential factors depend on the angular deviation $\Delta\theta$. In our model this component in the phase distribution of the exit-wave is essential for further propagation of the diffracted amplitude to the far-field by directly using Fourier transformation. In addition, the accurate phases are required for subsequent construction of the complete dataset in reciprocal space by merging diffraction patterns, which have been calculated for different angular deviations. Taking this into account, we determine all phases in reference to the origin of the laboratory coordinate system located on the crystal rotation axis. This point remains its position in both laboratory coordinate systems and that associated with the crystal during the angular scan. As a consequence, the phase distribution on the simulated diffraction pattern can

[10] Simulations performed in this work were done for the case of a perfect crystal.

be directly used in the merging in reciprocal space.

We suggest an alternative form of the Takagi-Taupin equations, which brings us to rather clear and elegant approach of the numerical solution. The key point is to propagate the diffracted wave field in the crystal straight along the direction to the detector, which holds its position during the angular scan. For that reason we define the wave vector of the diffracted field $\mathbf{k}_h$ as a constant vector with its magnitude equal to $k = \omega/c = |\mathbf{k}_0|$ remaining oriented to the center of the detector during the angular scan. Consequently, both wave vectors $\mathbf{k}_0$ and $\mathbf{k}_h$ are fixed in the laboratory coordinate system and the grid, used for the propagation of the wave field along provided directions, is unvarying with respect to the angular deviation $\Delta\theta$. In addition, the exponential factor $i\mathbf{k}_h \cdot \mathbf{r}$ in the expression for the total diffracted field on the exit surface yields a constant phase invariant with the angular deviation, and can be legitimately omitted in the merging procedure.

To derive these modified Takagi-Taupin equations we start with the wave equation (1.28), considering the case of $\sigma-$polarization, so the equation is written in scalar form. The solution of the differential equation (1.28) is expressed in the form of a sum of the Bloch waves

$$E(\mathbf{r}) = E_0(\mathbf{r})e^{i\mathbf{k}_0\cdot\mathbf{r}} + E_h(\mathbf{r})e^{i\mathbf{k}_h\cdot\mathbf{r}}. \tag{3.1}$$

Distinct to the representation (1.35) the wave vector of the diffracted field here is related to the reciprocal lattice vector as

$$\mathbf{k}_h = \mathbf{k}_0 + \mathbf{h}(\Delta\theta) + \Delta\mathbf{q}. \tag{3.2}$$

The residual wave vector $\Delta\mathbf{q}$ is determined by the angular deviation from the exact Bragg condition (see Figure 3.1). Hereafter we will refer the reciprocal lattice vector $\mathbf{h}(\Delta\theta)$ as simply $\mathbf{h}$ meaning that its orientation is a function of the angular deviation $\Delta\theta$.

In order to linearize the wave equation (1.28), the susceptibility and the total electric field are substituted by the decompositions (1.31) and (3.1). We assume that the considered volume is electrically neutral on average (so that div $\mathbf{E} = 0$) and use the following representation of the Laplace operator, applied to both components E_0 and E_h

$$\Delta[E_{0,h}(\mathbf{r})e^{i\mathbf{k}_{0,h}\cdot\mathbf{r}}] = [-k^2E_{0,h}(\mathbf{r}) + 2ik\frac{\partial E_{0,h}(\mathbf{r})}{\partial s_{0,h}} + \Delta E_{0,h}(\mathbf{r})]e^{i\mathbf{k}_{0,h}\cdot\mathbf{r}}. \tag{3.3}$$

That allows to split the equation in two parts corresponding to the propagation along directions

given by $\mathbf{k}_0$ and $\mathbf{k}_h$:

$$\begin{aligned}
&[\Delta E_0(\mathbf{r}) + 2ik\frac{\partial E_0(\mathbf{r})}{\partial s_0} + (k^2\chi_0 + k^2 - k^2)E_0(\mathbf{r}) + \\
&+k^2 E_h(\mathbf{r})e^{i\Delta\mathbf{q}\cdot r}\sum_{h_j}\chi_{h_j}e^{i(\mathbf{h}_j+\mathbf{h})\cdot\mathbf{r}-i\mathbf{h}_j\cdot\mathbf{u}}]e^{i\mathbf{k}_0\cdot\mathbf{r}} + \\
&+[\Delta E_h(\mathbf{r}) + 2ik\frac{\partial E_h(\mathbf{r})}{\partial s_h} + (k^2\chi_0 + k^2 - k^2)E_h(\mathbf{r}) + \\
&+k^2 E_0(\mathbf{r})e^{-i\Delta\mathbf{q}\cdot\mathbf{r}}\sum_{h_j}\chi_{h_j}e^{i(\mathbf{h}_j-\mathbf{h})\cdot\mathbf{r}-i\mathbf{h}_j\cdot\mathbf{u}}]e^{i\mathbf{k}_h\cdot\mathbf{r}} = 0.
\end{aligned} \tag{3.4}$$

Using an approximation of a non-divergent vector field $\Delta E_{0,h} \approx 0$ and neglecting all the non-interference components in the series the equation (3.4) can be transformed to a pair of linear differential equations:

$$\begin{aligned}
\frac{\partial E_0(\mathbf{r})}{\partial s_0} &= \frac{i\pi}{\lambda}[\chi_0 E_0(\mathbf{r}) + \chi_{\bar{h}}e^{i\Delta\mathbf{q}\cdot\mathbf{r}+i\mathbf{h}\cdot\mathbf{u}}E_h(\mathbf{r})], \\
\frac{\partial E_h(\mathbf{r})}{\partial s_h} &= \frac{i\pi}{\lambda}[\chi_0 E_h(\mathbf{r}) + \chi_h e^{-i\Delta\mathbf{q}\cdot\mathbf{r}-i\mathbf{h}\cdot\mathbf{u}}E_0(\mathbf{r})].
\end{aligned} \tag{3.5}$$

where the partial derivatives $\partial/\partial s_0, \partial/\partial s_h$ are taken along the directions of vectors $\mathbf{k}_0$ and $\mathbf{k}_h$. Different from the conventional form of the Takagi-Taupin equations used in [99], the angular dependence in the set of equation (3.5) is represented not by the angular deviation parameter α, but by the phase exponent, which leads to rather symmetric form. Also the propagation is performed not in the direction of $\mathbf{k}_0+\mathbf{h}$, but along the wave vector $\mathbf{k}_h$ given by the relation(3.2).

The boundary conditions assume the total electric field, represented by the decomposition (3.1), to be continuous everywhere including the crystal-vacuum boundary. At the same time the susceptibilities drop down to zero outside the media and thereby undergo discontinuity on the boundaries. We assume, that the vectors $\mathbf{k}_{0,h}$ are the same inside and outside the media, therefore the equations (3.5) do not require any transformation of the amplitudes E_0 and E_h on the crystal-vacuum boundary. Such boundary conditions are particularly useful for numerical integration in case of a three-dimensional crystal with an arbitrary shape.

3.3 Numerical solution of the Takagi-Taupin equations

Taking into account that the electric field is propagating along the directions of the incidence $\mathbf{k}_0$ and diffraction $\mathbf{k}_h$ vectors, it is practically useful to introduce a corresponding coordinate system. The set of basis vectors $\{\mathbf{e}_0, \mathbf{e}_y, \mathbf{e}_h\}$ is represented by the unit vectors in the direction of the incident beam, the normal to the scattering plane and the direction of diffracted beam (see Figure 3.2). Thus, the partial derivatives are taken along $\mathbf{e}_0$ and $\mathbf{e}_h$ vectors, and rotation is performed around the y-axis. The angle between $\mathbf{e}_0$ and $\mathbf{e}_h$ equals to $2\theta_B$, therefore the coordinate system is not orthogonal, but oblique. Any position within the considered volume can be

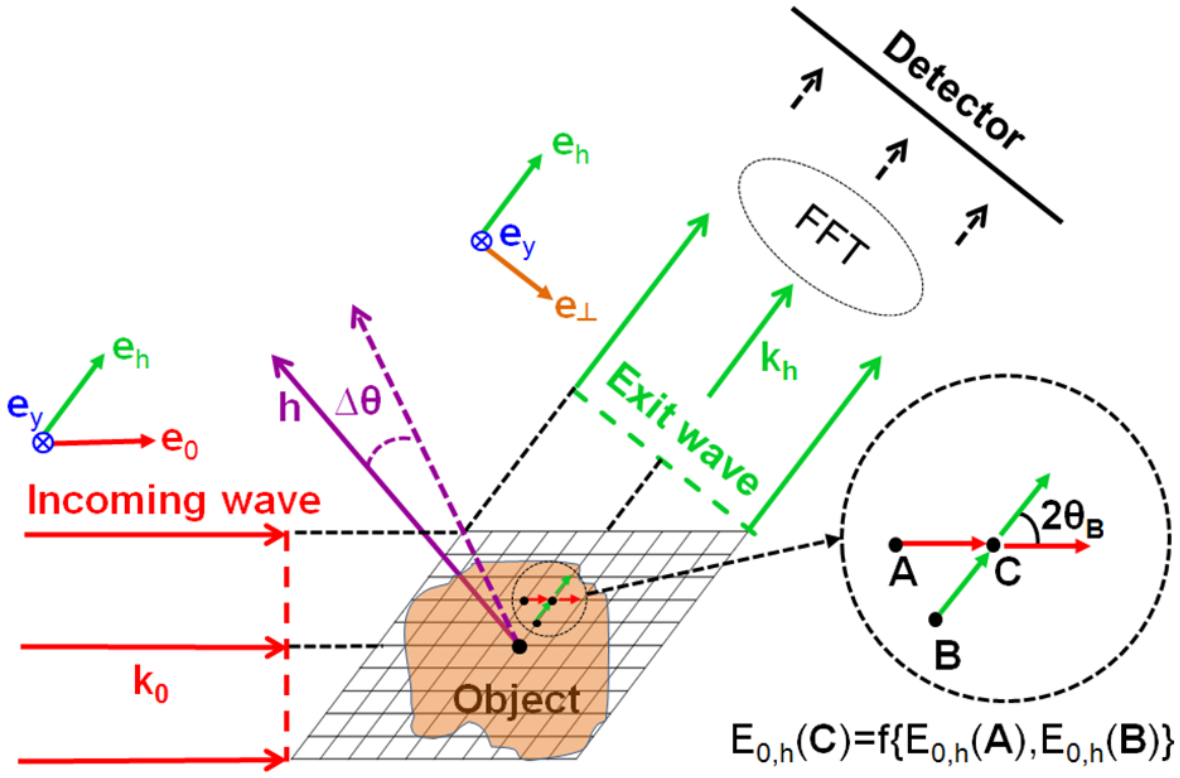

Figure 3.2: A sketch of the model showing a grid used for the numerical solution of the Takagi-Taupin equations. The drawing represents one of the two-dimensional slices in the whole rhombic prism, which enfolds the crystal. A Fast Fourier Transform (FFT) algorithm was applied to the exit wave, represented by a discrete set of values, in order to propagate it to the far-field.

described by the radius vector $\mathbf{r} = s_0\mathbf{e}_0 + s_y\mathbf{e}_y + s_h\mathbf{e}_h$, where s_0, s_y, s_h are the corresponding coordinates.

The numerical integration is performed over a rhombic prism in which the whole crystal is embedded, as it is shown in Figure 3.2. The side facets (parallel to the scattering plane) are represented by parallelograms, the others are rectangles. More specifically, the prism is sliced to a set of layers, settled for different value of the s_y coordinate parallel to the scattering plane, and the equations are solved in the two-dimensional grid independently for each of these layers. As it was discussed above, the propagation of the wave field is performed along the directions $\mathbf{e}_{0,h}$, which do not depend on the angular deviation $\Delta\theta$ in the laboratory coordinate system. Therefore, the whole grid remains invariable during the angular scan, while the coordinate transformation of the rotation is applied to the shape function of the crystal. The nods, which belong to the crystal, are characterized by non-zero values of Fourier components of the susceptibility, which are set to zero for the nods outside. In order to facilitate the treatment of the crystal boundary we use the Takagi-Taupin equations in the form (3.5), which uses real wave vectors $\mathbf{k}_{0,h}$ and requires no special transformation on the boundaries.

In the numerical integration method the complex amplitudes $E_{0,h}(\mathbf{r})$ are represented by a discrete set of values over all integration grid and the equations are transformed to a recurrence matrix form. The matrix expresses the amplitudes for a considered node on the grid as a function

of amplitudes at other nods, which have been calculated previously

$$\begin{pmatrix} E_0(s_0, s_h) \\ E_h(s_0, s_h) \end{pmatrix} = f \begin{pmatrix} E_0(s_0 - p, s_h) \\ E_h(s_0 - p, s_h) \\ E_0(s_0, s_h - p) \\ E_h(s_0, s_h - p) \end{pmatrix}. \tag{3.6}$$

The detailed derivation together with expressions for the matrix coefficients of function f can be found in Appendix A.

The inset in Figure 3.2 illustrates the recurrence properties of the matrix equation (3.6). The values of both amplitudes E_0 and E_h at each node of the integration grid $\mathbf{C}$ are given by the values calculated for anterior points $\mathbf{A}$ and $\mathbf{B}$. In such a way, the calculations proceed from node to node in the directions of the transmission and diffraction. Initially, the values of the amplitudes $E_{0,h}$ are given on the left and bottom sides of the prism, where $E_0 = E_{in}$ and $E_h = 0$, therefore, the integration starts from the lower corner of the front facet running over the nodes from the left to the right. When the opposite side is reached the run returns to the front facet and start the next line above the previous one and the process is continued until the upper facet of the prism is reached.

3.4 Propagation to the detector plane and merging diffraction patterns in reciprocal space

The numerical integration of the matrix equation (3.6) over the rhombic prism results in the complex amplitude at the exit facet ($s_h = s_h^{out}$). For further propagation we exploit an orthogonal coordinate system with the basis $\{\mathbf{e}_\perp, \mathbf{e}_y, \mathbf{e}_h\}$, where the additional vector $\mathbf{e}_\perp = \mathbf{e}_y \times \mathbf{e}_h$ is introduced. It is, basically, corresponding to the projection of $\mathbf{e}_0$ on the plane, which is perpendicular to $\mathbf{e}_h$. Taking this into account the equation for the conversion of the wave field amplitude takes the form

$$E_h^{out}(s_\perp, s_y) = E_h(s_0, s_y, s_h^{out}). \tag{3.7}$$

In such a way the conversion is performed by means of a simple projection $s_\perp = s_0 \sin(2\theta_B)$. As a result, the two dimensional distribution of the diffracted wave field in the plane, which is perpendicular to the direction of further propagation is obtained (shown in green in Figure 3.2). In the following the $E_h^{out}(s_\perp, s_y)$ will be referred to as the exit-wave.

For the free-space propagation the total electric field $E_h^{out}(s_\perp, s_y)\exp(ik_h s_h)$ can be expanded into a sum of infinite number of plane waves, which is referred to as the angular spectrum decomposition in Fourier optics [51]. Each of the component waves is traveling in its own direction and undergoes the corresponding phase change $\frac{\omega}{c}l$ on its path l to the prediction plane. The resulted wave field is composed by a coherent sum of all the propagated components, and in this way the propagation of the wave field is performed by the propagation of the angular spec-

trum. If the observation point is located in the far-field, this method yields simply a 2D Fourier transform of the complex amplitude distribution in the source plane. In the present work, where the exit wave is represented by a discrete set of values, the algorithm of Fast Fourier Transform (FFT) was used for that purpose.

In real experiments the measured diffraction pattern corresponds to the spherical surface in reciprocal space described by the Ewald sphere construction. However, similar to the case of the projection approximation, the Takagi-Taupin equations do not take into account the divergence of the wave field $\Delta E_{0,h}(\mathbf{r})$ during the propagation through the object. Therefore, the simulated 2D diffraction pattern must be attributed to the flat surface (see the schematic in Figure 3.1). To demonstrate this we deduced an analytical expression obtained by the replacement of the first equation with $E_0(s_0, s_y, s_h) = 1$. In addition, the zeroth component of the susceptibility in the second equation was terminated by setting $\chi_0 = 0$. As it was shown in Section 4 of Chapter 1 these two assumptions correspond to the purely kinematical case of the Takagi-Taupin equations. The amplitude of the outgoing diffracted wave field can then be estimated as an integral across the whole crystal along the direction of diffraction

$$E_h^{out}(s_\perp, s_y, \Delta\mathbf{q}) = \frac{i\pi}{\lambda}\chi_h \int s(\mathbf{r}) e^{-i\Delta\mathbf{q}\cdot\mathbf{r} - i\mathbf{h}\cdot\mathbf{u}} ds_h, \tag{3.8}$$

where the following representation $\mathbf{r} = \mathbf{r}(s_\perp, s_y, s_h) = s_\perp\mathbf{e}_\perp + s_y\mathbf{e}_y + s_h\mathbf{e}_h$ is used. To transform the integral to the indefinite form we introduced the shape function $s(\mathbf{r})$ that equals to unity everywhere inside the scattering volume and zero outside it. As it was discussed above the far-field diffraction pattern is obtained by the two-dimensional Fourier transformation of the exit-wave

$$A(q_\perp, q_y, \Delta\mathbf{q}) = \iint E_h^{out}(s_\perp, s_y, \Delta\mathbf{q}) e^{-iq_\perp s_\perp - iq_y s_y} ds_\perp ds_y, \tag{3.9}$$

where $q_\perp, q_y$ are the coordinates on the obtained image. By substituting the expression (3.8) in the equation (3.9) the latter can be rearranged as follows

$$A(q_\perp, q_y, \Delta\mathbf{q}) = \frac{i\pi}{\lambda}\chi_h \iiint s(\mathbf{r}) e^{-i\mathbf{h}\cdot\mathbf{u}} e^{-i\Delta\mathbf{q}\cdot\mathbf{r} - iq_\perp s_\perp - iq_y s_y} ds_\perp ds_y ds_h. \tag{3.10}$$

Seeing that $ds_\perp ds_y ds_h = d\mathbf{r}$, we consider the integral on the right as the three-dimensional Fourier transform of a complex function $s(\mathbf{r})\exp(-i\mathbf{h}\cdot\mathbf{u})$. That is commonly understood as the reciprocal space map in the vicinity of a given Bragg reflection as it discussed in Reference [29]. From the configuration of that integral it follows that the resulted image $A(q_\perp, q_y, \Delta\mathbf{q})$ corresponds to a flat surface, parallel to pair of vectors $\{\mathbf{e}_\perp, \mathbf{e}_y\}$. The central point ($q_\perp = 0, q_y = 0$) of this surface in given by vector $\Delta\mathbf{q}$ in reciprocal space.

Equation (3.10) might also serve as the foundational relation for the Bragg CXDI method. In particular, it directly shows how the reconstructed phase distribution in real space $\Delta\phi(\mathbf{r})$ is attributed to the projection of the local displacement to reciprocal lattice vector $\mathbf{h}\cdot\mathbf{u}$. That results in a final expression, which is commonly used for determination the deformation field

from the Bragg CXDI reconstructions

$$u_h(\mathbf{r}) = -\Delta\phi(\mathbf{r})\frac{d_{hkl}}{2\pi}. \tag{3.11}$$

Here the negative sign reflects the fact that the positive displacement (expanded lattice) leads to the positional shift of the Bragg peak towards lower $\mathbf{Q}$. Considering that the phase retrieval procedure yields the relative phases, which are determined up to some constant, the formula (3.11) is typically applied not to the absolute phases but to the phase difference between the strained and relaxed parts of the crystal.

3.5 Simulations for Au crystal of cubic shape

In this section we present results of simulations of the dynamical diffraction, performed using the model described above. In order to illustrate the appearance and key features of the dynamical effects and artifacts in the Bragg CXDI reconstruction we considered a very simple test object, such as symmetric cubic-shaped gold crystal with an ideal lattice. Figure 3.3 shows a

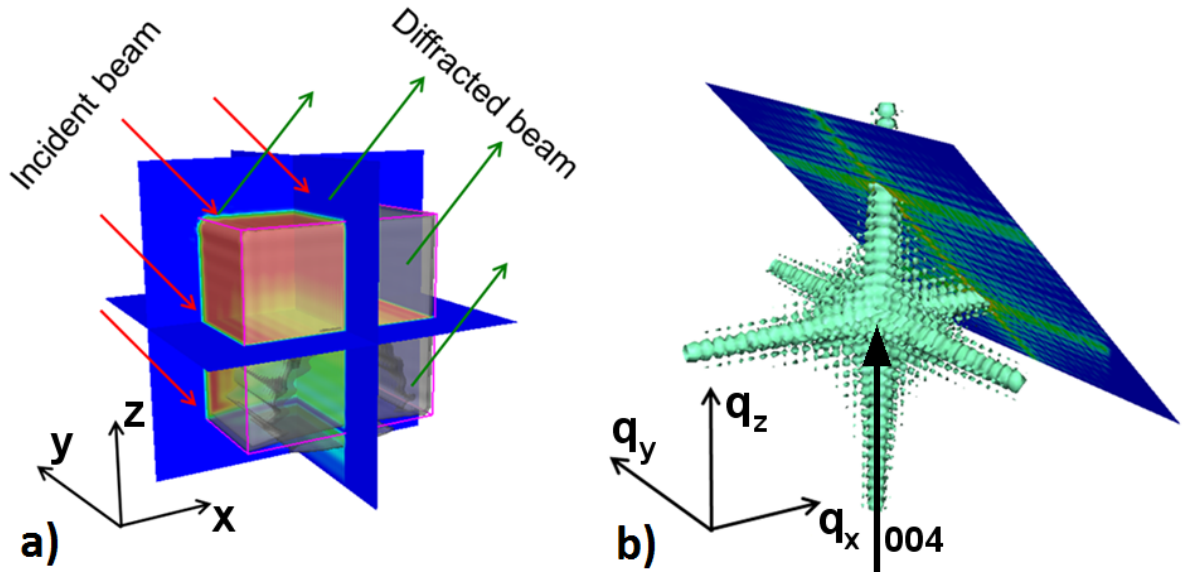

Figure 3.3: The diffraction geometry considered in simulations for a gold cubic crystal. (a) Results of the inversion to real space combined with the schematic view of the diffraction geometry. Different colors in transverse slices represent the charge density distribution. (b) The obtained dataset in reciprocal space. The tilted plane illustrates intensity distribution within one of the diffraction patterns.

schematic of the diffraction geometry in real and reciprocal spaces and the associated orthogonal coordinate system with the x, y, z-axes oriented along the cube edges. A gold crystal has a cubic unit cell $4.078\,\text{Å}$ in size. We assume that the basis vectors of the unit cell are oriented in the same way as the coordinate system shown in Figure 3.3. Hence, the selected (004) crystallographic plane is parallel to the xy-plane (lower and upper facets) and the scattering plane is parallel to the side facets.

We performed simulations for two crystals sizes $100\,\text{nm}$ and $1\,\mu\text{m}$. In the simulations we

considered a plane wave with 8 keV of incident photon energy (1.55 Å of wavelength), which corresponds to a Bragg angle of $49.5°$. For these parameters the Bragg and Laue extinction depths according to definition (1.40) are 711 nm and 607 nm, respectively.

The results of the wave field propagation through the 100 nm Au cube in the exact Bragg condition are presented in Figure 3.4 (a). The amplitude of the exit wave calculated in the frame of the dynamical theory (red curve) is compared to the results of the kinematical theory (black curve), given by equation (3.8). The nearly complete coincidence is a reflection of the fact that the cross coupling between the diffracted and transmitted waves does not gain its power, therefore, the kinematical approximation gives correct result. In this case, the calculated phase profile (blue curve) shows a small phase shift, which can be attributed to refraction. As it follows from scattering geometry (see Figure 3.3) the phase accumulated by the diffracted wave in the top left corner of the crystal can be assigned to zero, as it will be not affected by refraction.This phase will be accumulated more for the waves coming from the depth of the crystal. The scattered signal that contributes to the right part reveals a refraction phase shift of about 0.15-0.25 rad.

The results of the simulation performed in the same way for 1 µm Au crystal are presented in the Figure 3.4 (b). The amplitude profile has nearly the same shape as in the previous case for small crystal in the kinematical approximation. However, the dynamical calculations reveal a considerably lower amplitude profile in comparison to the kinematical prediction, which is explained by the attenuation of the transmitted wave due to the primary extinction. That mostly affects the lower and right part of the cube, therefore that suppression is particularly pronounced on the right side. It has to be mentioned, that even for 1 µm size Au crystal absorption does not have a strong effect, since the crystal size is significantly smaller than the absorption length for crystalline gold (2.9 µm at the given photon energy).

Further propagation of the diffracted amplitude to the far-field results in a 2D diffraction pattern. A series of such calculations performed for a 1 µm cubic Au crystal and different values of $\Delta\theta$ in the angular range from $-0.83°$ to $0.83°$ were merged together in reciprocal space. For comparison we performed simulations using kinematical and dynamical approaches. The central q_xq_z-sections (q_y=0) through the corresponding 3D reciprocal space maps are shown in Figure 3.5(a,b). Both kinematical and dynamical results display a regular structure of square speckles. As it was discussed earlier, such modulations are determined by the 3D Fourier transform of the shape function of the crystal (see equation (1.17) and Section 3 in Chapter 1). The results of simulations performed by dynamical theory show considerable aberrations in the position and magnitude of the fringes (see Figure 3.5(b)).

Difference in the positions and intensities of the speckles is clearly seen on the q_z- profiles taken along the central rode (see Figure 3.6(a)). The corrsponding phase profiles are shown in Figure 3.6(b). One remarkable feature is a displacement of the whole profile in the direction of q_z-axis in the case of dynamical theory simulations. That reflects the shift of the Bragg peak in the direction of positive angular deviations and originates from refraction of the wave field at the crystal boundaries. In the dynamical theory this effect is known as the angular displacement

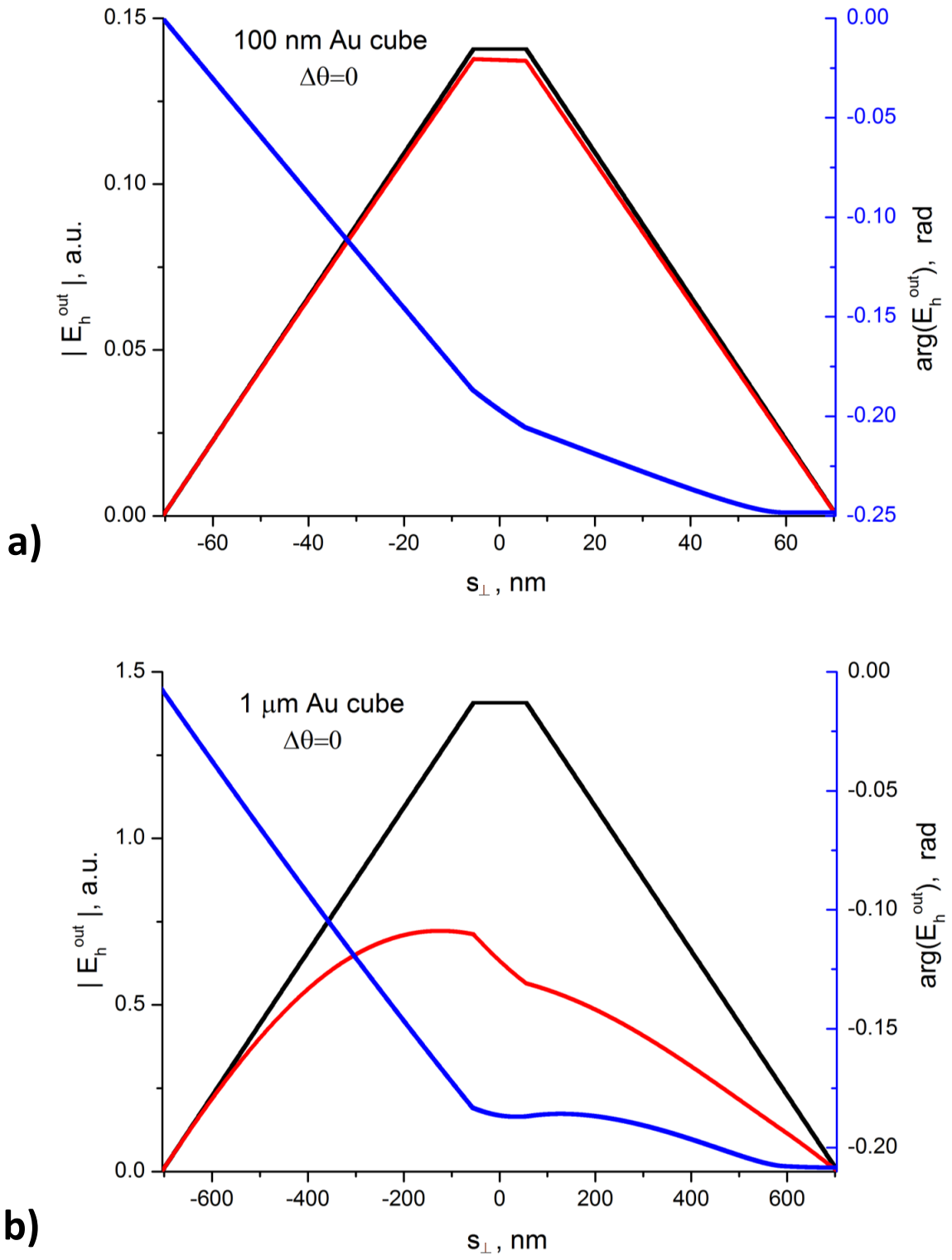

Figure 3.4: (a) The transverse profile of the amplitude (red) and phase (blue) of the exit wave calculated by the dynamical theory for a 100 nm cubic crystal of Au at the exact Bragg condition. For comparison, the amplitude profile obtained in the frame of kinematical theory is shown by the black curve. (b) The results of the same calculations performed for a crystal of 1 μm size.

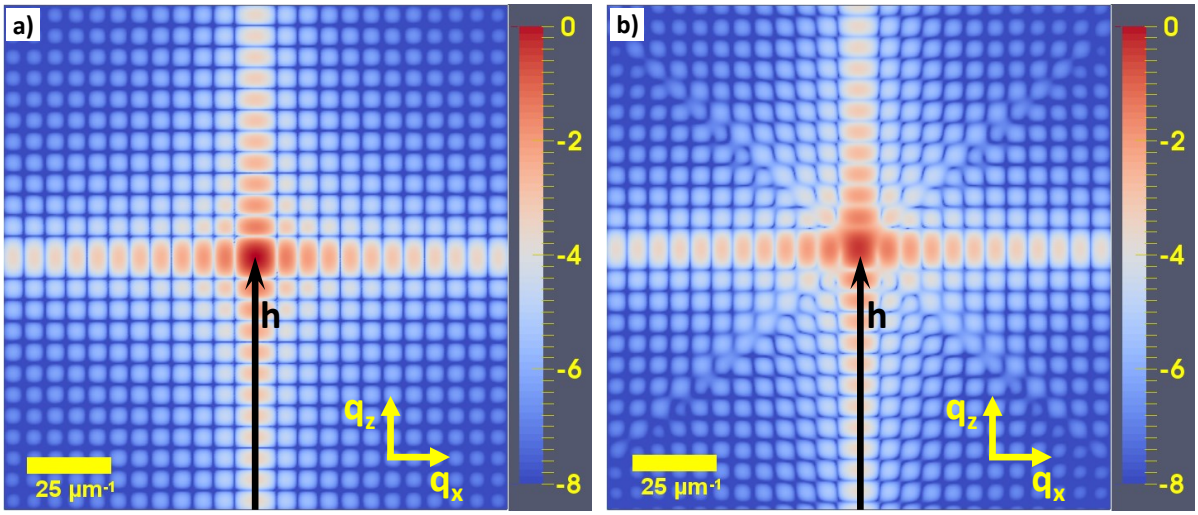

Figure 3.5: Distribution of the modulus of the scattered amplitude within the central $q_x q_z$-sections (q_y=0) through 3D reciprocal space map simulated for 1 μm cubic Au crystal (in logarithmic scale). (a) represents results of calculations performed in the frame of the kinematical theory using equation (3.10), (b) – results of the dynamical theory, obtained by a numerical solution of the Takagi-Taupin equations.

of maximum of the reflectivity curve due to refraction [27]. In the case of the Bragg geometry it is described by the following equation

$$\Delta\theta_M = -\frac{Re[\chi_0](1+b)}{2b\sin(2\theta_B)}. \tag{3.12}$$

Here the asymmetry parameter b is introduced by the directional cosines for the incident and diffracted beams

$$b = \frac{\cos(\mathbf{k}_0, \mathbf{n})}{|\cos(\mathbf{k}_0 + \mathbf{h}, \mathbf{n})|}, \tag{3.13}$$

where $\mathbf{n}$ is the surface normal. For the symmetric Bragg case the equation (3.12) is simplified to $\Delta\theta_M = -Re[\chi_0]/\sin(2\theta_B)$, which results in $18.6''$ angular shift for the reflection and photon energy considered in the simulations. The positional displacement of the maximum of the reflectivity curve in reciprocal space is then expressed as

$$\Delta q_M = 2|\mathbf{k}_0|\sin(\theta_B + \Delta\theta) - h \approx h\sin(\Delta\theta_M)\cot(\theta_B), \tag{3.14}$$

that corresponds to approximately $4.7\,\mu\text{m}^{-1}$. However, in the Laue geometry no positional shift of the reflectivity curve is observed. In the considered case the diffraction geometry represents a mixture of both Bragg and Laue cases since the shape of the crystal is cubic. Therefore, in addition to a positional shift the refraction also leads to a smearing of the central speckle in the direction of q_z-axis. Due to a big size of the central speckle (about $6.3\,\mu\text{m}^{-1}$ for 1 μm crystal size) this smearing is barely pronounced in Figure 3.5. At the same time it becomes more and more distinct in simulations for larger crystals.

The results of the inversion of the whole 3D reciprocal space dataset obtained in dynamical simulations into real space are presented in Figures 3.7 and 3.8. The panels (a,c) in both

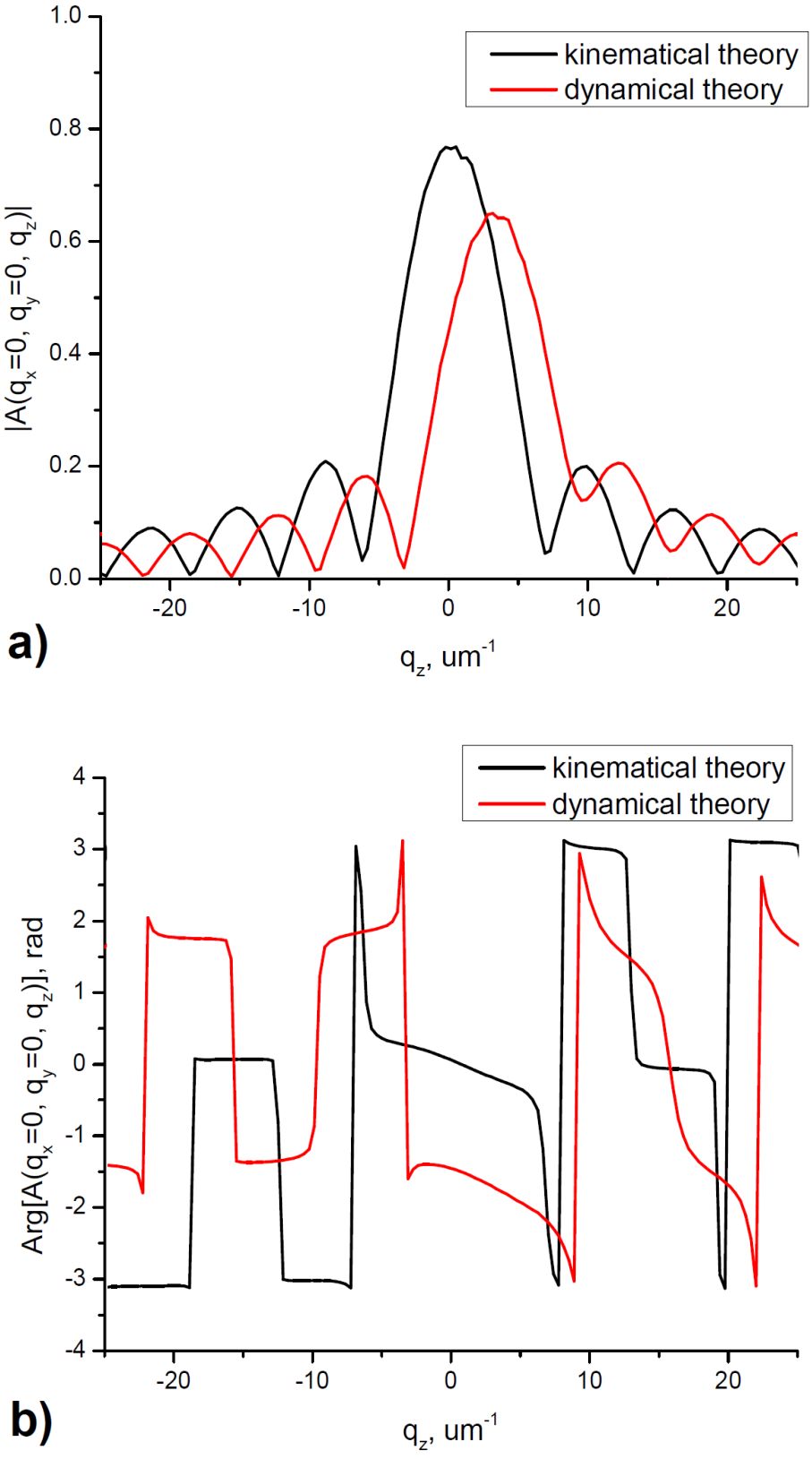

Figure 3.6: Distribution of the complex scattered amplitude along q_z- axis represented by the modulus (a) and phase (b) profiles. The cut is taken through the center of 3D reciprocal space map (q_x=0, q_y=0), which corresponds to the vertical rode in Figure 3.5(a, b). Black curves represent the results of calculations performed in the frame of the kinematical theory, red curves – results of the dynamical theory.

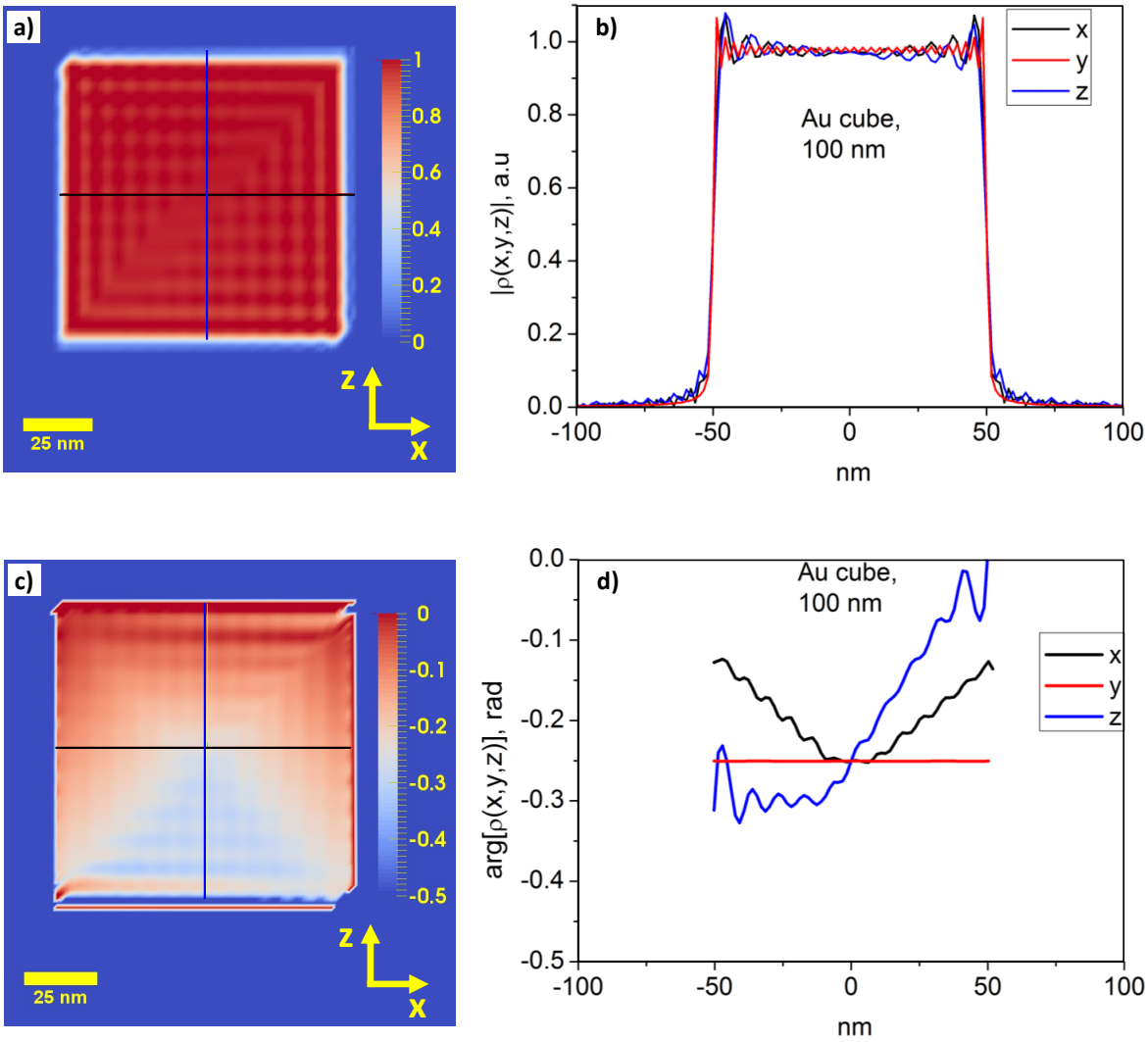

Figure 3.7: The amplitude (a, b) and the phase (c, d) of the complex electron density distribution obtained by the inversion of the 3D reciprocal space dataset calculated for a crystal size 100 nm. The xz-slices at $y = 0$ (center of the crystal) are presented in (a,c); the profiles along the x, y and z - axes are shown in (b,d).

Figures show the xz-slice through the center (y=0) of the crystal. The line profiles along x, y, z axes (schematically shown by the cross at the images on the left) going through the origin are shown in panels (b, d). The distribution of the amplitude reveals wrinkled structure on the cube edges, which is a consequence of a limited q-range in reciprocal space used for inversion. Sharp facets of the 3D shape function lead to intense truncation rodes in reciprocal space, which can be recognized as horizontal and vertical fringes in Figure 3.5. A considerable part of these crystal truncation rods was out of the calculated volume in reciprocal space that resulted in the oscillations close to the cube facets in the reconstruction. Out of the cube the amplitude of the reconstructed complex density function is rapidly going down. In this region the phases are not defined, therefore, the phase distribution presented in Figure 3.7(c,d) was cropped by the cube edges.

For 100 nm cube size no considerable artifacts are observed and the results are consistent with the kinematical theory. This agreement, however, brakes in the results of dynamical theory simulations performed for 1 µm crystal size, where artifacts both in the amplitude and phase distributions are clearly visible (see Figure 3.8). The bulb, which appears at the bottom of the crystal apparently originates from the coupling between the diffracted and transmitted waves in the crystal. Such artifact dramatically rises up with the increase of the ratio of the crystal size to the extinction length. Another interesting feature is the mirror symmetry with respect to z-axis i.e. the reciprocal lattice vector $\mathbf{h}$. That is rather surprising in view of the fact that the incident beam is coming from the upper left corner and elements of the scattering volume in the left and right part of the cube are not illuminated in the same way. We attribute that to the symmetry of the equations (3.5) with respect to the direction of propagation.

The attenuation of the amplitude present in the results of dynamical simulations for 1 µm crystal size can hardly be considered as the direct X-ray absorption of the wave field, since the crystal size is significantly smaller than the absorption length. On the other hand, the refraction effects are rather strong, as revealed by the phase gradient in Figure 3.8. Since this does not relate to the deformation of the lattice it can complicate the interpretation of the Bragg CXDI reconstructions. It is, however, possible to correct the obtained results for both, absorption and refraction, by estimating the corresponding optical path that the radiation passes in the crystal on the way toward the considered point and on the way out. In the next section we analyze the Tagaki-Taupin equations with the aim to demonstrate how the contributions of refraction and absorption can be separated from the results of CXDI.

3.6 Treatment of refraction and absorption

A convenient way to treat the refraction effects was demonstrated previously [103]. The phase of the reconstructed complex density map was corrected by a subtraction of the phase shift accumulated according to the corresponding optical path for every position within the scattered volume. However, it was not fully clear if that approach is correct in case of the dynamical

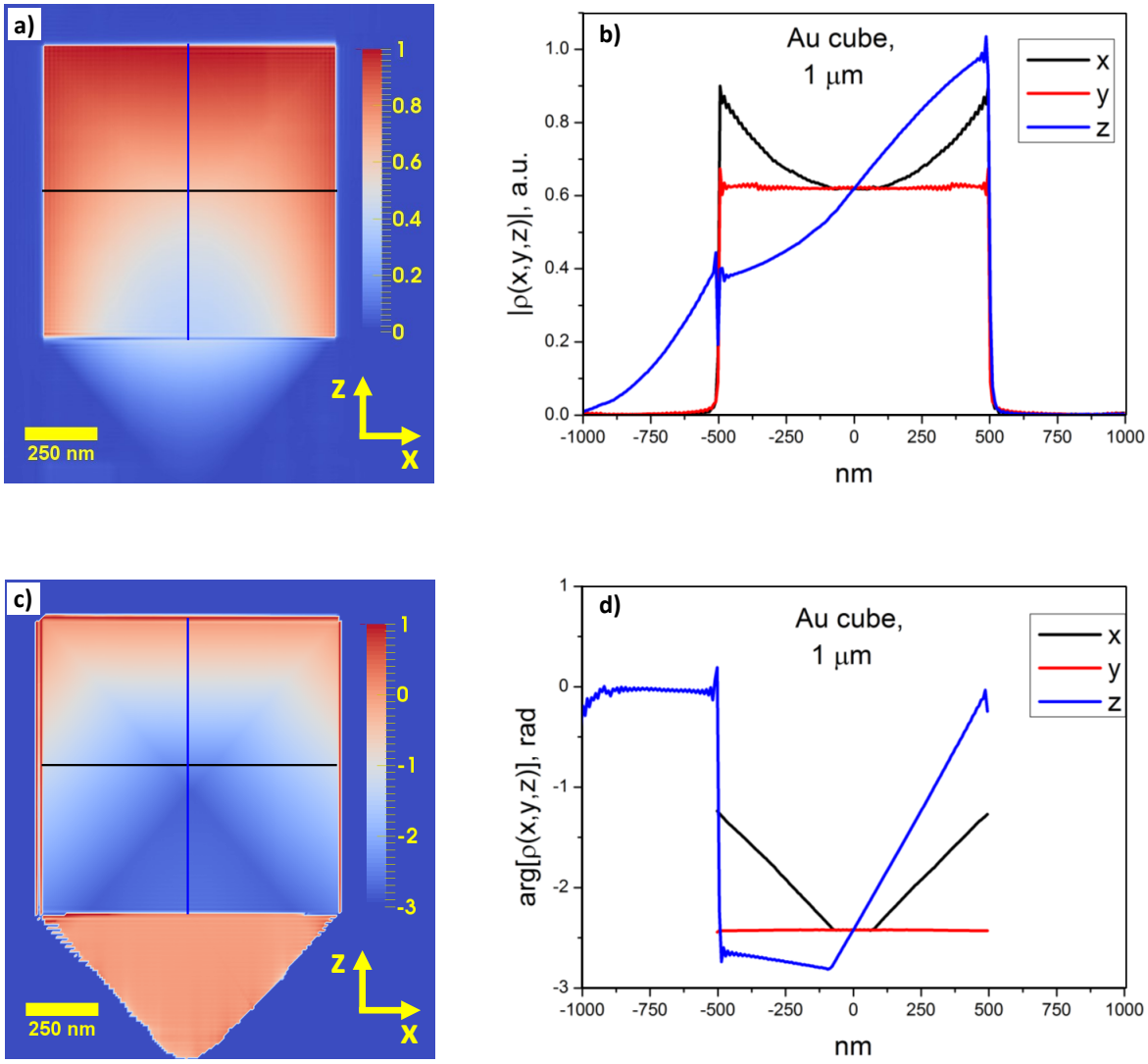

Figure 3.8: The amplitude (a, b) and the phase (c, d) of the complex electron density distribution obtained by the inversion of the 3D reciprocal space dataset calculated for a crystal size 1 μm. The xz-slices at $y = 0$ (center of the crystal) are presented on the left; in (a,c); the profiles along the x, y and z - axes are shown in (b,d).

diffraction where the interference effects of cross coupling waves takes place. Here we provide some proving analytical derivations and introduce a function for the correction of refraction and absorption in Bragg CXDI. We demonstrate how the reconstruction results might be corrected by application of this function for the simulations results, presented in the previous section.

Four terms in the equations (3.5) describe the contributions of different physical processes, which can be considered separately. The term with χ_h describes diffraction of the incident component of the wave field by a set of crystallographic planes with reciprocal vector **h**. In its turn the diffracted component undergoes diffraction by the same set of planes but from the opposite side, which is described by the term proportional to $\chi_{\bar{h}}$. These two cross components determine the mutual coupling of the incident and diffracted waves and highly depend on the structure of a unit cell and the indices of the reflection. Finally, the real and imaginary part of the term proportional to χ_0 describe refraction and absorption effects, which both waves undergo independently from each other. For a selected wavelength this parameter is determined by the averaged electron density irrespective to any symmetry in the arrangement of atoms (see equation (1.29)). In order to understand how these different physical processes may contribute to the artifacts in CXDI, we will consider the contribution of all corresponding components separately. To simplify our derivations for the correction function we rearrange the Takagi-Taupin equations (3.5) for another form, more advantageous for analytical treatment.

3.6.1 Takagi-Taupin equation with complex wave vectors

If both coupling terms are excluded from the set of equations (3.5), it turns into a couple of linear differential equations of one variable, which describe independent the transmission of the E_0 and E_h waves through the media without diffraction. In this case, the analytical solution for each of the equations is represented by an exponential function with the factor $ik\chi_0 s_{0,h}/2$. It is convenient to include these exponents into the definition of the modified amplitudes E'_0 and E'_h, so that

$$\begin{aligned} E_0(\mathbf{r}) &= E'_0(\mathbf{r}) e^{i\frac{\chi_0}{2}\mathbf{k}_0\cdot\mathbf{r}}, \\ E_h(\mathbf{r}) &= E'_h(\mathbf{r}) e^{i\frac{\chi_0}{2}\mathbf{k}_h\cdot\mathbf{r}}. \end{aligned} \tag{3.15}$$

According to the decomposition (3.1) the total wave field is expressed as

$$E(\mathbf{r}) = E'_0(\mathbf{r}) e^{i(1+\frac{\chi_0}{2})\mathbf{k}_0\cdot\mathbf{r}} + E'_h(\mathbf{r}) e^{i(1+\frac{\chi_0}{2})\mathbf{k}_h\cdot\mathbf{r}}. \tag{3.16}$$

Then, the propagation of each component can be considered as for a plane wave that has a wave number $k(1+\chi_0/2)$, so the wave vector is treated as a complex value with the directional properties given only by its real part. This transformation is often used in the dynamical theory to simplify the derivations [27]. In this approach the refraction and absorption of both diffracted

and transmitted waves are included in their definition

$$\begin{aligned}\mathbf{K}_0 &= (1+\frac{\chi_0}{2})\mathbf{k}_0,\\ \mathbf{K}_h &= (1+\frac{\chi_0}{2})\mathbf{k}_h.\end{aligned} \tag{3.17}$$

Substituting relations (3.16) into equations (3.5) one can obtain the Takagi-Taupin equations in another practically useful form

$$\begin{aligned}\frac{\partial E'_0(\mathbf{r})}{\partial s_0} &= \frac{i\pi}{\lambda}\chi_{\bar{h}}e^{i\Delta\mathbf{Q}\cdot\mathbf{r}+i\mathbf{h}\cdot\mathbf{u}}E'_h(\mathbf{r}),\\ \frac{\partial E'_h(\mathbf{r})}{\partial s_h} &= \frac{i\pi}{\lambda}\chi_h e^{-i\Delta\mathbf{Q}\cdot\mathbf{r}-i\mathbf{h}\cdot\mathbf{u}}E'_0(\mathbf{r}),\end{aligned} \tag{3.18}$$

where the complex residual wave vector is defined as

$$\Delta\mathbf{Q} = \Delta\mathbf{q} + \frac{\chi_0}{2}(\mathbf{k}_h - \mathbf{k}_0). \tag{3.19}$$

As it naturally follows from the expressions (3.15), the modified amplitudes $E'_{0,h}$ differ from $E_{0,h}$ inside the material, but are the same in vacuum. Therefore, the boundary conditions for the equations (3.18) shall be expressed as:

$$E_{0,h}^{'cryst}(\mathbf{R}_b) = E_{0,h}^{'vac}(\mathbf{R}_b)e^{i\frac{\chi_0}{2}\mathbf{k}_{0,h}\cdot\mathbf{R}_b}, \tag{3.20}$$

where $\mathbf{R}_b$ is the radius vector of a given point at the crystal-vacuum boundary; $E_{0,h}^{'vac}$ and $E_{0,h}^{'cryst}$ are the values of amplitudes in vacuum and inside the crystal. This is equivalent to the condition of continuity of the tangential component of the electric field at the interface.

3.6.2 Correction function

Let us assume that the coupling term proportional to $\chi_{\bar{h}}$ in equations (3.18) is suppressed by setting it to 0. Then the second equation is simplified to a single ordinary differential equation, which can be solved analytically similar to equation (3.8). When the boundary conditions (3.20) are applied, the expression for the exit wave amplitude takes the form

$$E_h^{out}(s_\perp, s_y) = \frac{i\pi}{\lambda}\chi_h \int e^{i\mathbf{K}_h\cdot\mathbf{R}_{out}-i\mathbf{k}_h\cdot\mathbf{R}_{out}-i\mathbf{K}_0\cdot\mathbf{R}_{in}+i\mathbf{k}_0\cdot\mathbf{R}_{in}}s(\mathbf{r})e^{-i\Delta\mathbf{Q}\cdot\mathbf{r}-i\mathbf{h}\cdot\mathbf{u}}ds_h. \tag{3.21}$$

Here $\mathbf{R}_{in} = \mathbf{R}_{in}(\mathbf{r})$ and $\mathbf{R}_{out} = \mathbf{R}_{out}(\mathbf{r})$ are the radius vectors of the points, where the incoming and outgoing rays for given element volume $\mathbf{r}$ cross the crystal boundaries. The expression under the integral can be transformed to

$$\left[e^{i\frac{\chi_0}{2}(\mathbf{k}_h\cdot\mathbf{R}_{out}-\mathbf{k}_0\cdot\mathbf{R}_{in}-\mathbf{k}_h\cdot\mathbf{r}+\mathbf{k}_0\cdot\mathbf{r})}s(\mathbf{r})e^{-i\mathbf{h}\cdot\mathbf{u}}\right]e^{-i\Delta\mathbf{q}\cdot\mathbf{r}}. \tag{3.22}$$

By the replacement

$$s'(\mathbf{r}) = s(\mathbf{r})e^{i\frac{\chi_0}{2}(\mathbf{k}_h\cdot\mathbf{R}_{out}-\mathbf{k}_0\cdot\mathbf{R}_{in}-\mathbf{k}_h\cdot\mathbf{r}+\mathbf{k}_0\cdot\mathbf{r})}, \tag{3.23}$$

the integral is reduced to the previously described case of equation (3.8). Correspondingly, the inversion of the reciprocal space dataset to real space results in a complex density distribution function, which in this case is represented by $s'(\mathbf{r})\exp(-i\mathbf{h}\cdot\mathbf{u})$. Therefore, the correction of the reconstruction results must be performed through multiplication with the correction function

$$f_c(\mathbf{r}) = e^{-\frac{i\pi}{\lambda}\chi_0\left(|\mathbf{R}_{in}-\mathbf{r}|+|\mathbf{R}_{out}-\mathbf{r}|\right)}, \tag{3.24}$$

where the total path for the incident $|\mathbf{R}_{in}-\mathbf{r}|$ and diffracted $|\mathbf{R}_{out}-\mathbf{r}|$ rays is calculated for each position $\mathbf{r}$ within the crystal. The estimate is done for a certain angular position neglecting small variations of the optical path during the rocking scan. The equation (3.24) takes into account both the phase gradient caused by refraction and attenuation, which originates from absorption.

Figure 3.9 illustrates results of such correction applied to the complex electron density distribution presented in Figure 3.8. Since the precise crystal shape and complete information about the directions of the vectors $\mathbf{k}_0$ and $\mathbf{k}_h$ are known, the function (3.24) was evaluated numerically from the reconstruction. After the correction the amplitude distribution at the lower part of the crystal increased from 0.38 to 0.52. At the same time, the upper part, where the absorption effects are much smaller due to shortness of the optical path, does not reveal any significant changes. That results in a small bending of the z-profile at the top of the crystal. However, the main characteristics of the artifacts in the amplitude distribution, such as the depletion of the electron density in the bulk and the protuberant part below the cube remain almost unchanged. From this we conclude that such artifact appears owing to cross coupling between the transmitted and diffracted waves, which is a purely dynamical effect. On the other hand, a strong phase gradient present in Figure 3.8 appeared to be effectively removed by the correction. The residual aberrations in the range from 0 rad to 0.3 rad is apparently connected to the cross-coupling of the diffracted and transmitted waves in the crystal. More specifically, they should be attributed to the imaginary part ot the Fourier components of the susceptibility χ_h and $\chi_{\bar{h}}$, that introduce a small phase shift when the wave is reflected by a crystalline plane. The Figure 3.10 shows results of calculations where that phase shift was suppressed by setting $Im[\chi_h] = 0$ and $Im[\chi_{\bar{h}}] = 0$ in equations (3.5). The phase distributions of the corrected electron density reveal zero value throughout the whole crystal, which approves our conclusion.

To make sure that the presence of cross-coupling terms does not interfere the procedure of the correction by equation (3.24) we performed complementary simulations where the contribution of refraction and absorption was suppressed by setting $\chi_0 = 0$ in equations (3.5). A comparison with the corrected results of the fully dynamical case, presented in Figure 3.9 shows that both results entirely coincide with each other.

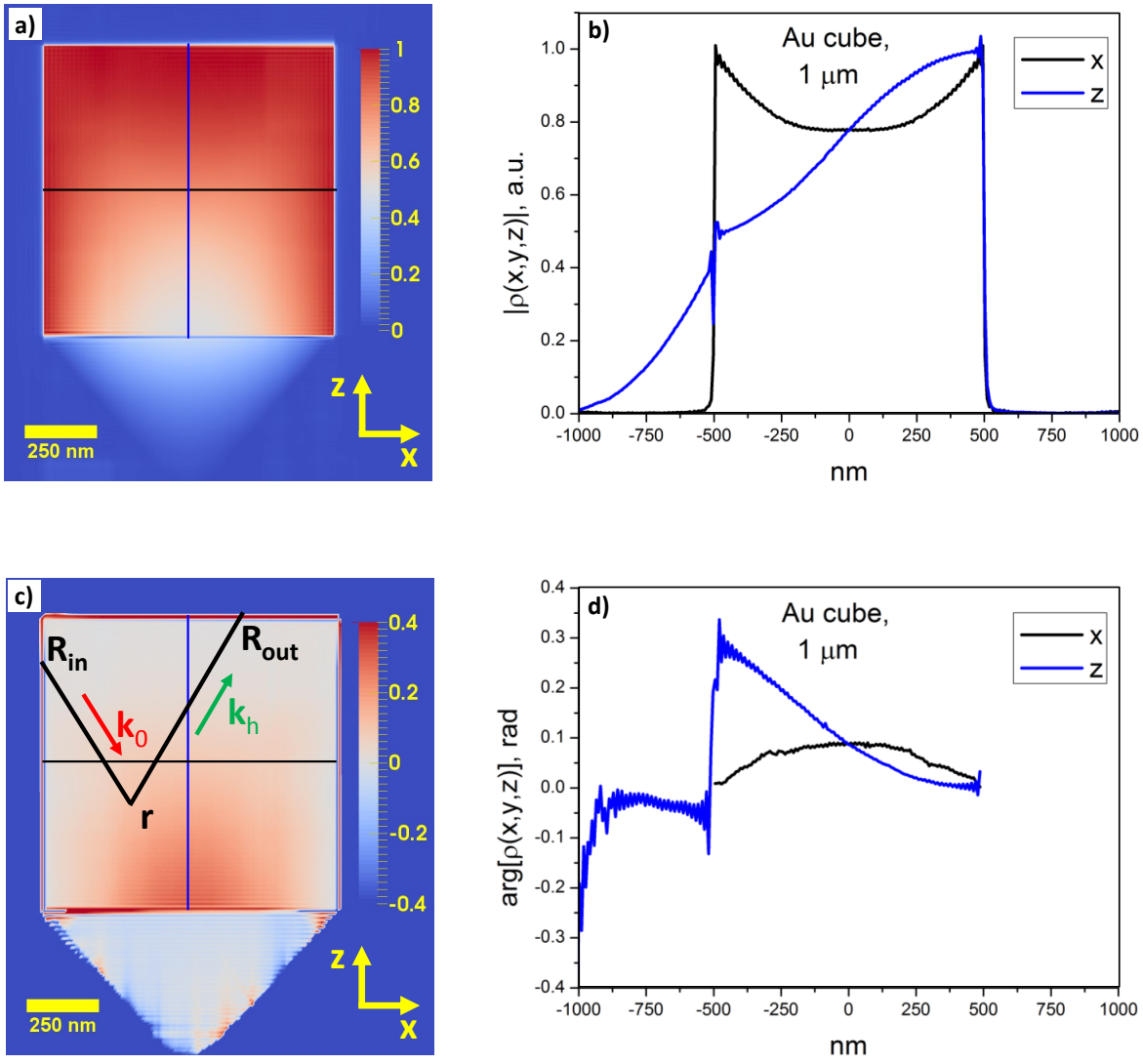

Figure 3.9: The results of simulations for 1 μm Au cube presented in Figure 3.8 after applying the correction with the function $f_c(\mathbf{r})$ (3.24). The amplitude corrected for absorption and the phase corrected for refraction are represented for the xz-slice in (a, c) and by profiles along the x and z axes in (b, d). The scheme in (c) illustrates the total optical path ($|\mathbf{R}_{in} - \mathbf{r}| + |\mathbf{R}_{out} - \mathbf{r}|$ calculated for a point given by $\mathbf{r}$.

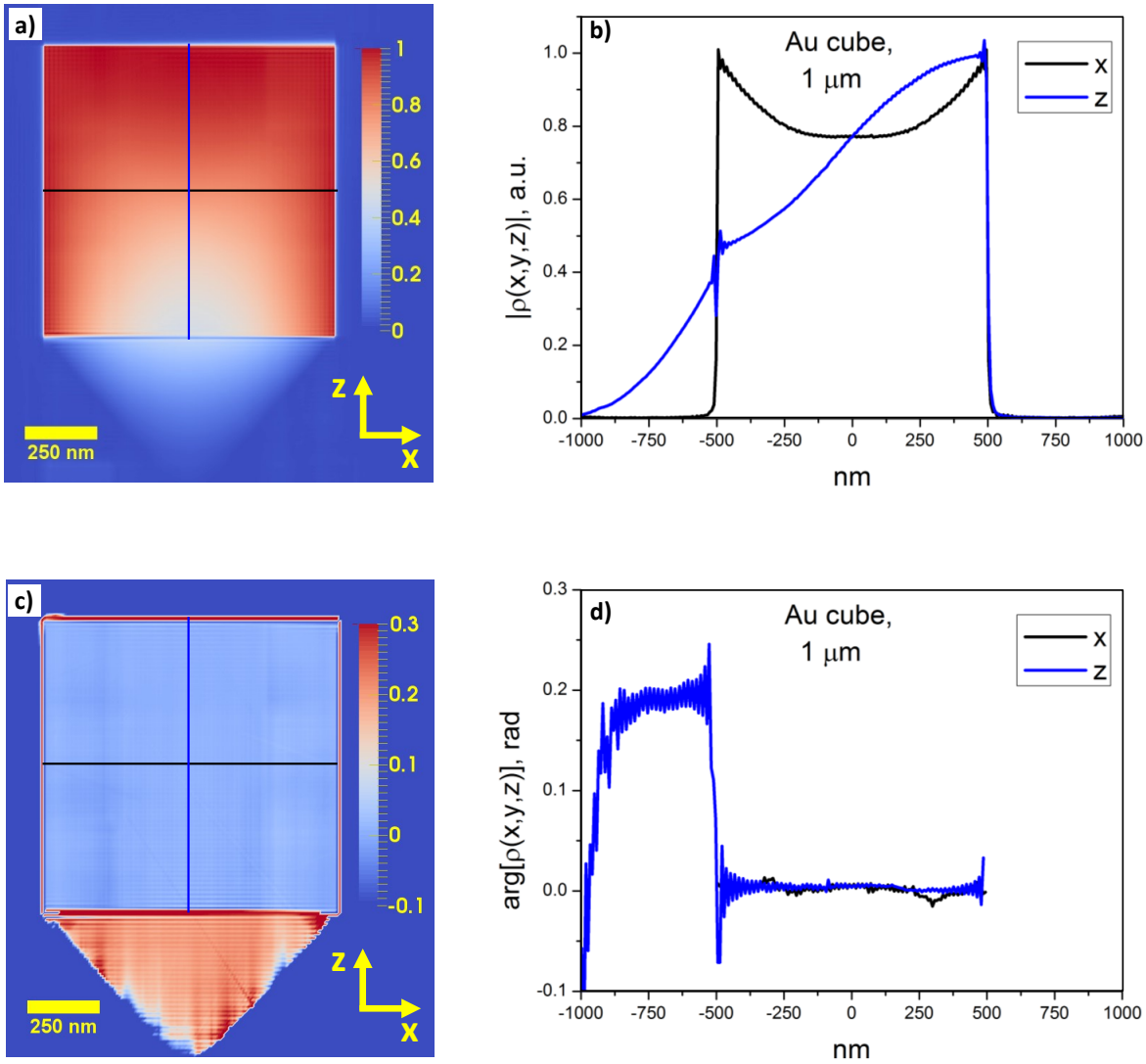

Figure 3.10: Results of simulations for 1 μm Au cube calculated with the assumption $Im[\chi_h] = 0$, $Im[\chi_{\bar{h}}] = 0$, after correction by the function $f_c(\mathbf{r})$ (3.24). The amplitude and the phase are represented for the xz-slice in (a, c) and by profiles along the x and z axes in (b, d).

3.7 Simulations for a Pb particle of hemispherical shape

The results of the simulation for a perfect cubic crystal have shown that the dynamical diffraction can lead to appearance of artifacts in the real space reconstruction. In order to estimate the contribution of the dynamical effects for a practical case, we considered experimental parameters described in References [33, 103]. In that experiment a 3D reconstruction of the Bragg CXDI data was used for characterization of the strain distribution in a hemispherical droplet of lead of $0.75\,\mu$m in diameter. The Pb(111) reflection was selected and a rotation series of 50 surrounding diffraction patterns were collected by rotating the sample in steps of $0.01°$. The droplet was coherently illuminated by a monochromatic X-ray beam of $1.38\,$Å wavelength, which corresponds to $13.79°$ of the Bragg angle for the Pb(111) reflection with $0.27\,\mu$m and $1.07\,\mu$m values of the extinction depth for the Bragg and Laue geometries, respectively.

In our simulations we considered a shape function represented by a sphere truncated from one side by $1/3$ of the diameter, as the closest model to the one described in the experiment. The faceting plane was assumed to be tilted by $27°$ with respect to the (111) crystallographic plane. The diffraction geometry from two perspectives of view is schematically shown in Figure 3.11(a,b).

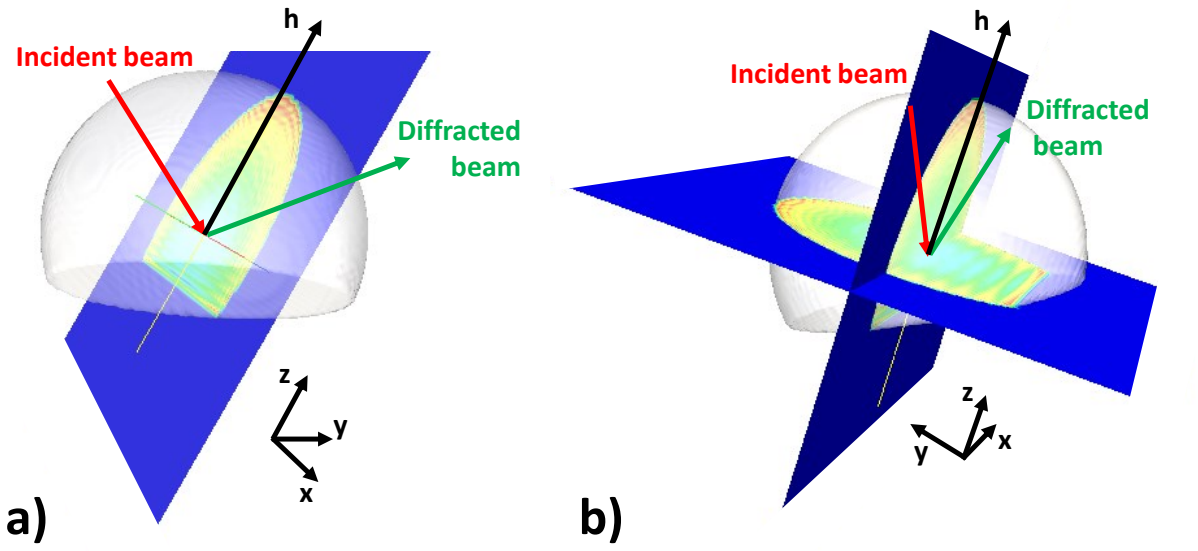

Figure 3.11: The diffraction geometry used in simulations for a Pb nanoparticle of hemispherical shape (a sphere truncated from one side by $1/3$ of the diameter) of $0.75\,\mu$m in diameter. The faceting plane is tilted by $27°$ with respect to (111) crystallographic plane. (a) and (b) show a view from two different perspectives.

The Figure 3.13 shows results of simulations performed by the dynamical theory. A series of the diffraction patterns, calculated in the angular range from $-0.83°$ to $0.83°$ with $12''$ increment, were merged into a 3D reciprocal space dataset and then inverted to real space. According to the geometry of simulation (see Figure 3.11) the cut along z-axis is not symmetric with respect to the center, but covers the range from $-d/2 + d/3 = -125\,$nm to $d/2 = 375\,$nm. The amplitude distribution shown in Figure 3.12(a,b) reveals slight depletion of the electron density

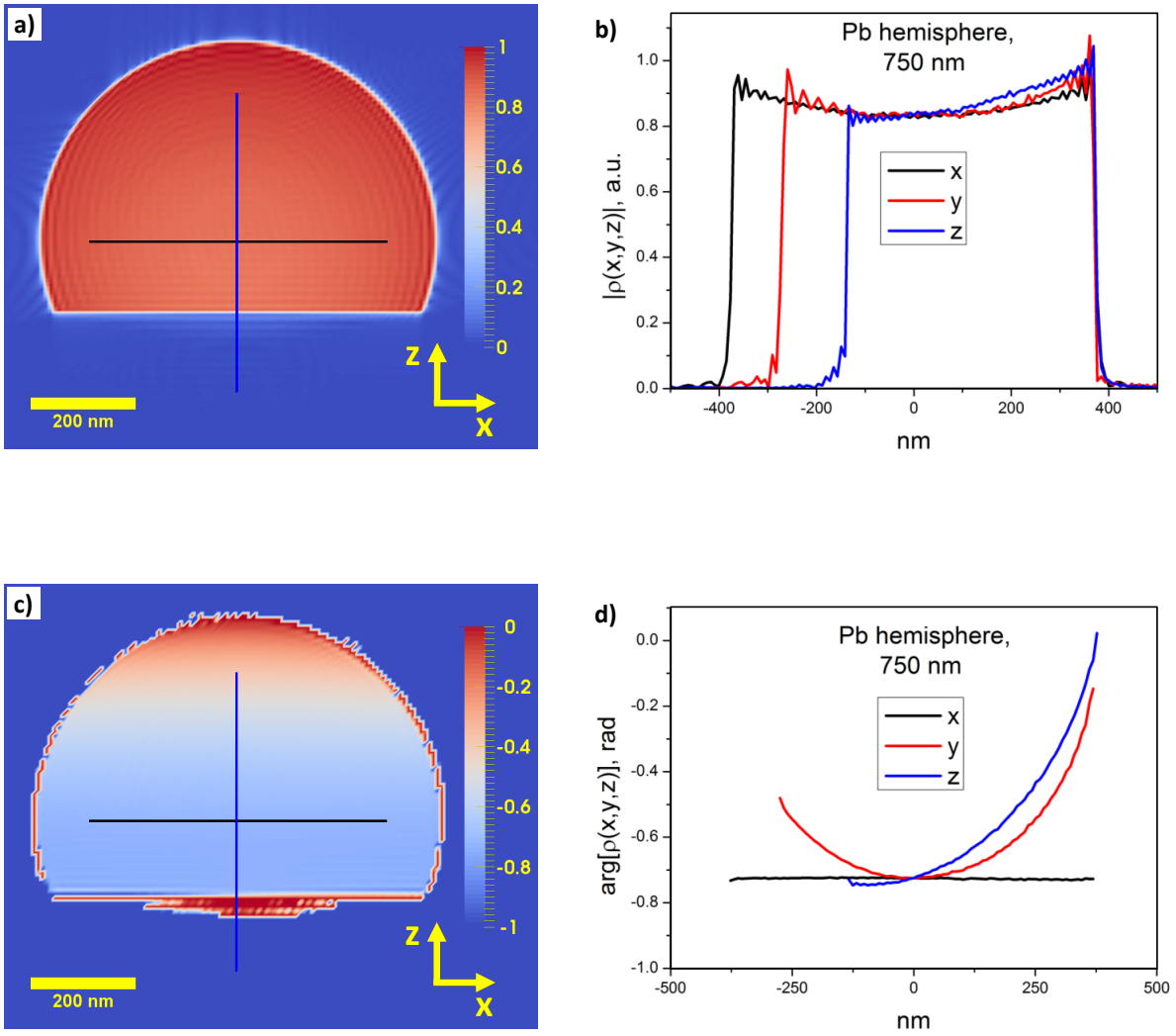

Figure 3.12: Results of simulations for a hemispherical Pb crystal $0.75\,\mu$m in size. The 3D electron density distribution was obtained by the inversion of scattered amplitudes calculated by dynamical theory. The amplitude and the phase are represented for the xz-slice in (a, c) and by profiles along the x, y and z axes in (b, d).

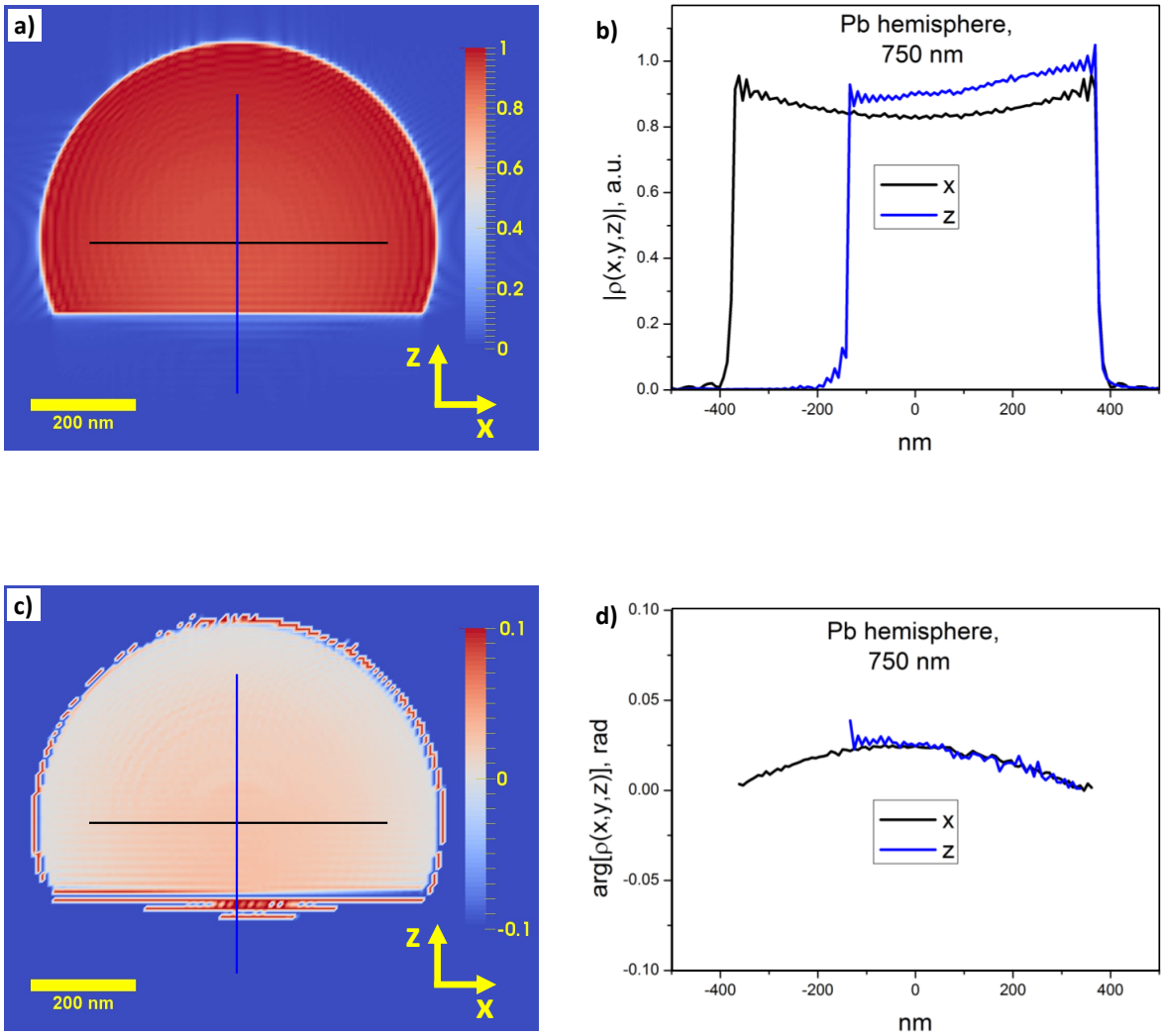

Figure 3.13: The results of the correction by the function $f_c(\mathbf{r})$ (3.24) applied to the results of simulation presented in Figure 3.12. The amplitude and the phase are represented for the xz-slice in (a, c) and by profiles along the x and z axes in (b, d).

in the central part, which corresponds to attenuation of the incident and diffracted waves in the bulk of the crystal. Nevertheless, the contribution of such an artifact appears to be relatively small (about $10\,\%$ of the average value). That approves the feasibility of the kinematical approach used by authors in their analysis. In the phase distribution (see Figure 3.12(c,d)) a considerable phase gradient with the maximum of the phase deviation about 0.7 rad is observed. Since no strain was introduced in the simulations such artifact originates from refraction and needs to be corrected.

Figure 3.13 shows results of the correction for refraction and absorption by the function $f_c(\mathbf{r})$ (3.24). As far as the contribution of absorption is small, the resulted amplitude distribution, presented in Figure 3.13(a,b), reveals no significant changes in comparison to that in Figure 3.12(a,b). Correction for refraction removed a major part of the gradient in phase distribution (see Figure 3.12(c,d)). The residual variations up to 0.03 rad can be considered as negligibly small. For comparison, the value of maximum phase deviation, which was obtained from the reconstruction of the dataset in the experiment [33] with subsequent correction for refraction, was estimated as 1.15 rad [103]. For this value of phase difference equation (3.11) gives a corresponding displacement of the surface layers by 0.52 Å relative to the bulk.

Our simulations demonstrate the applicability of our approach for modeling of the dynamical effects for parameters of a real experiment. A convenient method of the corrections for refraction and absorption was elaborated, application of this method to the reconstruction results was demonstrated. Furthermore, the developed model, can be used in rather general cases of the dynamical diffraction on finite size crystals of almost any shape.

3.8 Phase variations of the transmitted wave in case of Laue diffraction on a thin crystalline plate

In this section we apply our model for simulations of Laue diffraction on a thin crystalline plate. When the crystal thickness is sufficiently smaller than the extinction length the kinematical theory can be legitimately applied. Indeed, in the limit of a very thin crystal the results of dynamical theory converge to the kinematical one [27] (see Section 1.4 of Chapter 1 for details). However, even in this limit the interaction between the transmitted and diffracted waves may result in very small, but measurable effects, which cannot be treated in the frame of the kinematical theory, since they have purely dynamical nature. For example, a small quantity of the diffracted wave field is reflected by the back side of the same set of crystallographic planes and interferes with the transmitted component, which affects both the amplitude and phase of the transmitted wave. A direct observation of the wave field phase is impossible in conventional scattering experiments, since detectors allow to measure only the intensity of X-rays. However, the iterative phase retrieval methods, such as CXDI or ptychography, allow to retrieve the missing phase, using some additional information about the sample. Applying these methods it becomes possible to measure and characterize such small effects.

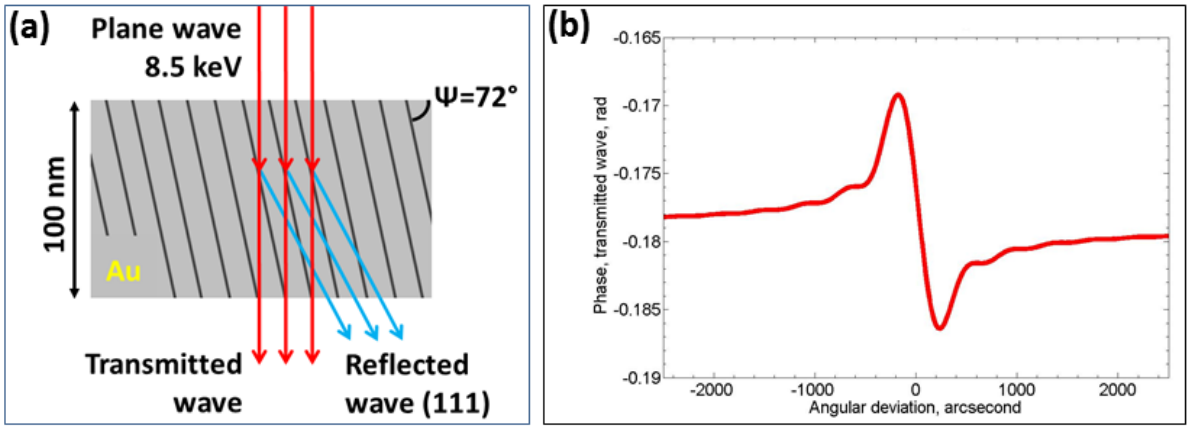

Figure 3.14: (a) A schematic view of the diffraction geometry used in simulations with an infinite crystalline plate. (b) The calculated angular dependence of the phase of the transmitted wave.

In an experiment [104] ptychography was employed to reconstruct the complex amplitude of the transmitted wave. This method allowed to measure the variations in the phase of the transmitted wave as a function of the angular deviation in the rocking scan. It was suggested to fit the parameters of this experimental curve to get information about the phase of the diffracted wave.

In this study we calculated the dependence of the transmitted beam's phase on the angular deviation from the Bragg condition using the dynamical theory. We considered the case of an experiment [104] where number of golden particles of cylindrical shape were illuminated by a coherent X-ray beam in Laue geometry. A sketch of the experiment is presented in Figure 3.14(a). The selected particle was about 100 nm thick and the (111) crystallographic planes were inclined by 72° to the entrance surface. For the selected 8.5 keV of photon energy the Bragg angle was 18°, therefore the direction of incidence was orthogonal to the crystal surface. Since the value of the extinction depth defined by equation (1.40) was about 2.1 μm, the crystal can be considered as a thin one.

In our simulations we assumed an infinite crystalline plate and performed numerical integration of equations (3.5) using the approach described in Section 1-3 of the present Chapter with the aim to calculate the phase of the transmitted amplitude on the exit surface (see Figure 3.14(a)) near the Bragg condition. The angular dependence of the transmitted phase presented in 3.14(b) reveals a small, but clearly visible variations from the constant phase ramp of 0.18 rad corresponding to the refraction phase shift for a Au plate with 100 nm thickness. These variations are about 0.016 rad in total and have a purely dynamical nature because they originate from the coupling between the transmitted and diffracted waves. The phase profile reveals steep decrease of the phase value from the maximum on the left to the minimum on the right. On the reflectivity curve that corresponds to the change of the phase of the diffracted wave over π (see Figure 1.9(a) in Section 4 of Chapter 1 for details).

The results of our simulations are in good agreement with the reconstruction of the experimental data [105]. In the Reference [105] we developed an analytical approach that gives direct

relation between the phase of transmitted wave and of the complex susceptibilities in case of a thin crystals with thickness much less than the extinction length [105].

3.9 Conclusions

A theoretical approach to the numerical solution of the Takagi-Taupin equation in the case of finite size 3D crystal of arbitrary shape is developed. A suggested modification of the Takagi-Taupin equations offers a convenient way to solve them numerically using an integration grid, which is invariable with respect to the angular deviation from the exact Bragg condition. As a result, the complex amplitude distributions of the transmitted and diffracted waves can be calculated. Propagation to the far-field gives the amplitude and phase distribution on the diffraction pattern that corresponds to a specific cross-section in reciprocal space. By performing a series of such calculations a full 3D reciprocal space dataset in the vicinity of the corresponding reciprocal lattice node can be constructed. Then, the complex function of the object in real space can be obtained by the inverse Fourier transformation.

Using this model we performed simulations of the dynamical diffraction on a perfect crystal of gold of cubic shape for $100\,\mathrm{nm}$ and $1\,\mu\mathrm{m}$ size. For a small crystal the result of our calculations was in full agreement with the kinematical theory. However, in the simulations for the large crystal artifacts both in reciprocal and real space were observed due to dynamical scattering effects. The contributions of different phenomena, such as refraction, absorption and cross-coupling between the diffracted and transmitted waves were analyzed separately. Based on the analytical derivations we developed a straightforward way to correct the results on reconstructions for the effects of refraction and absorption. Such corrections, applied to the results of the simulations, demonstrates a complete removal of corresponding contributions in the real space reconstruction. The residual artifacts in the amplitude and phase distributions are attributed to the cross-coupling of the diffracted and transmitted waves in the crystal. Additional simulation for a practical case of a Bragg CXDI experiment with a hemispherical Pb particle of $750\,\mathrm{nm}$ size was performed.

The developed model was used for a simulation of the angular dependence of the phase of the transmitted wave in the case of thin crystalline plate infinite in two dimensions. Small variations of this phase observed in the vicinity of the Bragg angle have a purely dynamical nature. Such variations are related to the structure factor, therefore, this demonstration is of importance for further development of method of obtaining such information from experimentally measured data.

Chapter 4

Nano and Mesoscopic materials

Mesoscopic physics is a sub-discipline of condensed matter physics which deals with materials of an intermediate length scale between the size of molecules and micrometres. Such systems behave very differently from large-scale objects and often have unusual physical and chemical properties, which makes them remarkably interesting to science and engineering applications. There is no rigid definition for the mesoscopic length scale, but the systems studied are normally in the range of 100 nm to 1 µm. Starting to reveal quantum mechanical properties such an object cannot be treated anymore as a continuum. The fluctuations around the average and the discrete structure must be taken into account. New categories of phenomena such as quantum confinement and charging effects provided them a variety of applications in the fields of nanofabrication and nanotechnology [106]. Receiving a growing attention, the science of mesoscopic systems holds many of well-established methods developed for studying and synthesizing such objects and this field is rapidly progressing nowadays.

In this thesis we demonstrate how methods of coherent X-ray diffraction can be applied for *in situ* structural investigation of mesoscopic materials, such as colloidal crystals. Due to their unique optical properties, these novel materials have been the focus of many investigations [107, 108, 109] and could have serious implications for modern photonics [110]. They may find applications in future solar cells, light emitting diodes, lasers, or even as the basis for circuits in optical computing and communication [111]. Perhaps, the most striking is the possibility of obtaining a complete photonic band gap, a range of energy for which the photon cannot propagate in any direction inside the structure [112, 113]. With this property, 3D colloidal crystals would allow to inhibit unwanted spontaneous emission and manipulate the flow of light [114].

Functional properties of the photonic crystals strongly depend on the crystal quality. It has been shown that by introducing defects it is possible, for example, to trap photons [109, 115], which opens the way to develop optical chips [116]. However, the manufacturing problems are still far from being solved. Lithographic methods are very effective for producing high-quality materials with any desired structure, however, the applicability of such structures is highly limited by slow and costly production processes [115]. In contrast, self-organized colloidal

crystals can be synthesized under ambient conditions by vertical deposition techniques [117, 118] and thus represent a cheap alternative class of materials which is more promising in terms of speed and production cost [111].

4.1 Colloidal crystals

Colloid is a substance consisting of particles substantially larger than atoms or ordinary molecules but too small to be visible to the unaided eye. Colloidal systems may exist as dispersions of one substance in another where microscopically dispersed insoluble particles are suspended throughout a liquid. As distinct from a solution both dispersed phase (the suspended particles) and a continuous phase (the medium of suspension) are present. The statistical mechanics of colloids is driven by the potential of mean force which depends on properties of the colloidal surface. Changing chemical properties of the solvent or adding a depletant it is possible to modify the mean force potential from steeply repulsive to deeply attractive. Due to Brownian motion colloids redistribute their kinetic energy into thermal motion of the solvent molecules and reach a thermodynamical equilibrium. Most important roles in the interaction of colloid particles are played by the following forces [119]:

Excluded volume repulsion refers to the impossibility of any overlap between hard particles.

Electrostatic interaction, which cause either repulsion or attraction that depends on electrical charge carried by both the continuous and the dispersed phases.

The van der Waals forces produced by an interaction between two dipoles that are either permanent or induced [120, 121]. A temporary dipole, which can be generated by fluctuations of the electron density even if the particles do not have a permanent dipole induces a dipole in particles nearby resulting in short-range attractive force. The van der Waals forces are always present unless the refractive indexes of the dispersed and continuous phases are matched.

Entropic forces, which are resulting from the entire system's statistical tendency to homogenize the distribution of various species in the solution and progress to a state with greater entropy [121].

Steric force between polymer-covered surfaces or in solutions containing non-adsorbing polymer can produce an additional steric repulsive force or an attractive depletion force [122].

When a saturated solution with colloidal particles evaporates particle sedimentation arises from a difference in the density of the dispersed and continuous phase. Pulled together by capillary forces the particles try to fill the least space and find a thermodynamic equilibrium state. If a crystallization nucleus is found the particles can arrange into regular lattices [123, 109, 124]. One of the finest natural examples of this ordering phenomenon can be found in

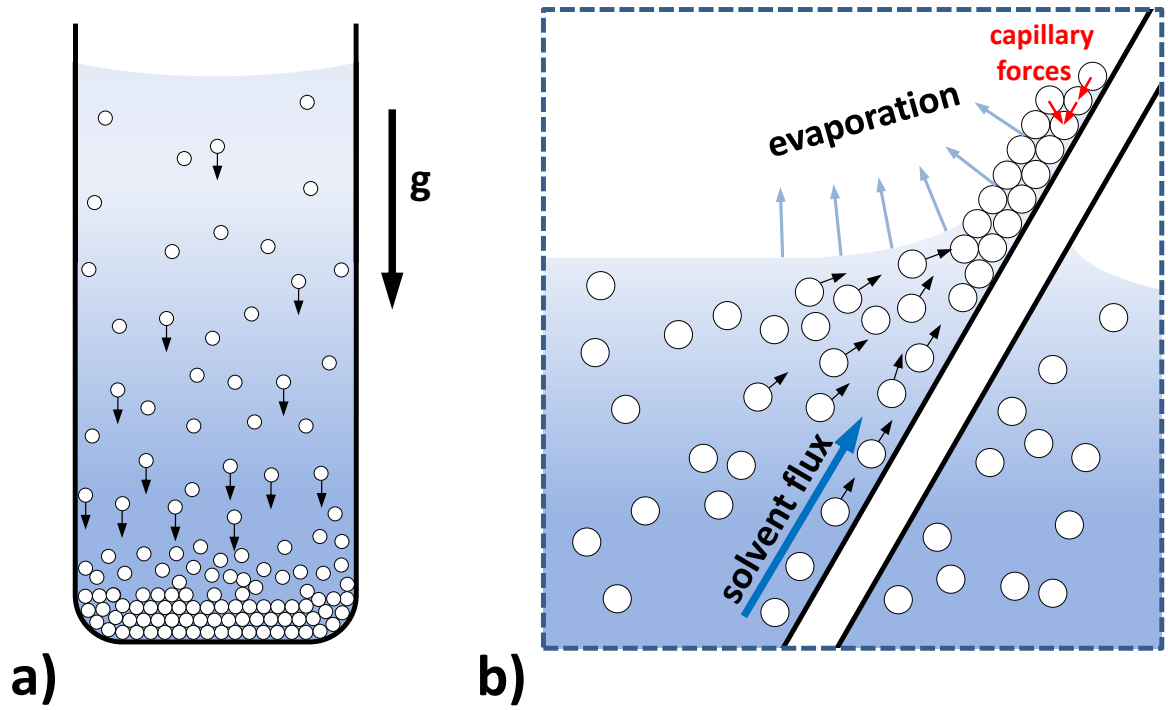

Figure 4.1: Schematic outlines of two common procedures to assemble colloids into 3D crystalline structures: (a) sedimentation in a gravitational field; (b) vertical deposition by evaporation. A convective flow causes transport of particles toward the meniscus, where the molecules from the solvent evaporate, leaving the colloidal particles behind.

precious opal, in which highly ordered close-packed arrays of amorphous colloidal spheres of silicon dioxide are formed after years of sedimentation and compression under hydrostatic and gravitational forces [125, 126]. Appearing analogous to their atomic or molecular counterparts colloidal crystals act as a natural diffraction grating for visible light waves, analogous to the scattering of X-rays in crystalline solids [127].

There are several ways to prepare artificial colloidal crystals of which the most used are sedimentation by gravity or controlled evaporation of the solvent. Figure 4.1(a) shows schematic representation of the sedimentation of colloids into close-packed 3D structures. Driven by gravitation force, particles slowly settle at the bottom of the solution in the form of dense sediments. Since the crystallization nuclei rise up at different locations the process results in a polycrystalline sample with domains of various sizes. A drawback of this method is that quality of the crystal and the the domain size highly depend on the sedimentation speed which is difficult to control.

Another commonly used growth technique is the vertical deposition by evaporation (see Figure 4.1(b)). A dispersion containing a low concentration of monodisperse colloids slowly evaporates on a substrate inducing a convective flow which transports new particles to the meniscus. Pulled together by capillary forces particles try to fill least space and form a close-packed structure [124]. This method was first introduced by Jiang *et.al.* [123] and has been improved over the years [128, 129]. It has been shown that resulting crystals reveal a tendency towards face centered cubic (FCC) stacking, which inspired detailed studies of self-assembly

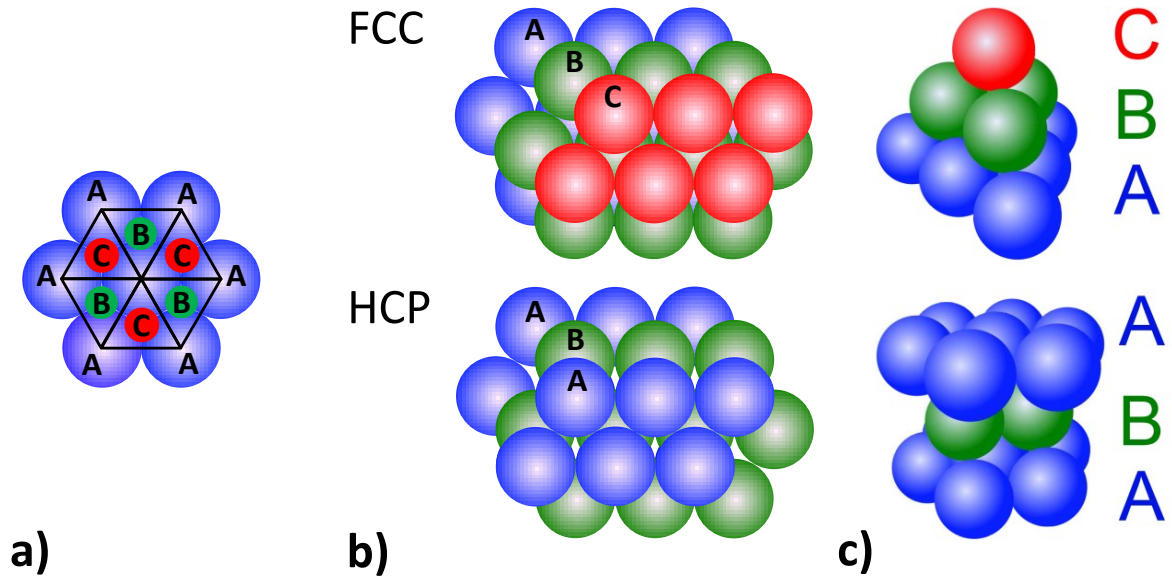

Figure 4.2: (a) Top view of three possible positions, denoted as A, B and C, in a hexagonal close-packed layers. (b) Top view of stacking of 3 close-packed layers in FCC and HCP lattices. (c) FCC and HCP structures from the side view.

process [130, 131, 132, 133].

The research presented in this thesis deals with colloidal crystalline structures formed by uniform polystyrene and silica spheres. From the theory [134] it is known, that highest averaged density in close-packed arrangements of equal spheres is achieved when they form plain hexagonal layers, which can occupy only three specific positions relative to each other, as it shown in Figure 4.2(a). Let the layer at the bottom be called A layer (colored with blue in schematic). The layer above it can be placed in two types of triangular voids, one with the apex upwards and labeled B (green color), and the other with the apex downwards and labeled C (red color). Only one of these sites can be occupied, but not both. If the second layer is B, then, similarly, the third hexagonal close-packed layer can occupy either A or C positions and so on. Any sequence of the letters, A, B and C with no two successive letters alike represents a possible manner of close-packing. In such a three-dimensional structure, each sphere is surrounded by and touches 12 other spheres.

The two most common close-packed structures which occur in nature are the hexagonal close-packed (HCP) structure with a stacking period AB, and the face-centered cubic (FCC) with a layer stacking ABC (see Figure 4.2(b,c)). In colloidal crystal the free-energy difference between HCP and FCC is rather small [11] [135, 136]. Therefore a random mixture of two stacking types, the so-called random hexagonal close-packed (RHCP) structure, is often observed [137, 138] in colloidal crystal films grown by self-assembly techniques. Even in regular crystals the ideal order of repeated sequences might be broken with one layer slipped to another

[11] According to Reference [135] the FCC structure of hard spheres is more stable than the HCP structure by a molar Gibbs free-energy difference of $\approx 0.005RT$, where R is the universal gas constant.

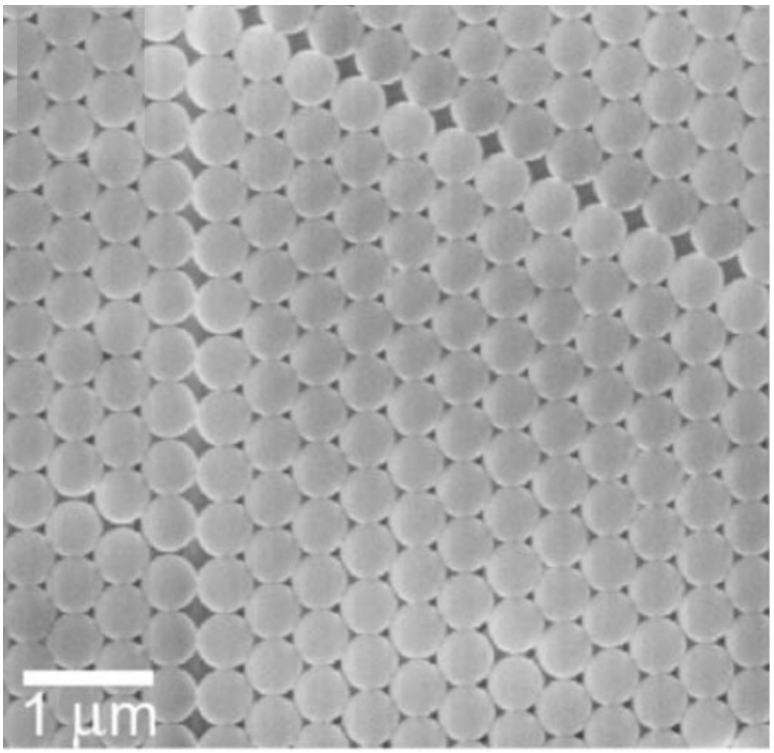

Figure 4.3: SEM image of the surface of a polystyrene colloidal crystal film revealing stacking defects. Figure was adopted from Reference [70].

position resulting in the stacking defect (see Figure 4.3). Since the important optical properties of the crystal, such as photonic band gap depend on the defects, it becomes of importance to characterize the quality of fabricated crystals.

Despite the large interest in self-organized colloidal crystals, much is still unknown about the processes governing self-assembly. That hinders the control of the intrinsic disorder present in such systems and brings the difficulty of including functional defects at desired positions. To fully understand the relations between the growth process and formation of defects detailed knowledge about the local internal structure has to be accessible.

4.2 Methods for structural characterization of colloidal crystals

The structure of colloidal systems can be examined in different ways. Among widely used techniques are optical microscopy [139, 140] and confocal laser scanning microscopy [141]. However, a range of applications of these methods is strongly reduced by limited resolution (at best 250 nm to 300 nm). Scanning electron microscopy (SEM) can provide high-quality images of the material surface with exceptional resolution [123], but fails to probe the bulk, because of low penetration depth for electrons. In addition, imaging in SEM typically involves elaborate sample preparation [142], such as drying or coating. In this respect, high-resolution hard and soft X-ray microscopy [143, 144, 145], small-angle X-ray scattering (SAXS) [146] and

small-angle neutron scattering (SANS) [147] represent complementary methods offering the advantage of high penetration depth for nondestructive studies of colloidal systems [148]. In comparison to SANS, the synchrotron based SAXS methods exploit highly intense and collimated X-ray beams, which provides microradian resolution [149, 150, 137, 151, 152, 153, 154]. The latter is essential for the characterization of the long-range positional order in colloidal crystals [155, 138, 117].

In this thesis we report on results of coherent X-ray diffraction experiments with colloidal crystals, performed in the small-angle scattering geometry. The investigated structures consisted of uniform silica or polystyrene colloidal particles of spherical form. According to the kinematical theory the coherently scattered signal measured in the far field is determined by the product of the form factor and structure factor

$$I(\mathbf{q}) = P(\mathbf{q})S(\mathbf{q}). \tag{4.1}$$

It can be shown that the form factor of uniform sphere with radius R normalized to its volume can be represented as [156]

$$P(\mathbf{q}) = \left\{ \frac{3[\sin(|\mathbf{q}|R) - |\mathbf{q}|R\cos(|\mathbf{q}|R)]}{(|\mathbf{q}|R)^3} \right\}^2. \tag{4.2}$$

Due to relatively big size of particles (200-500 nm) the modulations of the intensity given by the form factor can be measured in the small-angle scattering geometry. On the diffraction pattern such modulations are represented by a series of concentric rings (see Chapter 6 for details).

The contribution of the structure factor $S(\mathbf{q})$ results in the concentration of intensity around points which correspond to nods of the reciprocal lattice. That is observed as a regular structure of bright spots (Bragg peaks) on the diffraction picture. The positions and relative intensities of the Bragg peaks are defined by the symmetry of the crystal and lattice disorder. Furthermore, in the presence of stacking defects the some of the Bragg peaks smear into elongated rods in reciprocal space [71]. This subject will be discussed more detailed in the next chapter.

Chapter 5

CXDI experiment with a single colloidal crystal grain

An experimental demonstration of applying ideas of coherent X-ray diffractive imaging for visualization of a stacking fault in a thin colloidal crystalline film was first presented by J. Gulden et. al. [70]. In recent work [71] it was proposed to extend this method to three dimensions. The full 3D reciprocal space data from a single crystal grain was measured by collecting a diffraction patterns during the azimuthal scan. However, due to experimental challenges it was not possible to perform the 3D reconstruction of the measured dataset at that stage. Following these ideas and in a view of our previous experience we performed a sequent experiment and achieved detailed reconstruction which visualizes positions of individual particles in a single colloidal crystal grain. In this chapter we discuss the details of the experiment and data analysis. A brief review of an independent study of intensity profiles along the Bragg rods which have been observed in reciprocal space will be given.

5.1 Experimental

The samples were prepared from dried sediments of colloidal crystals that showed characteristic optical Bragg reflections [71]. The specimen studied in this work consisted of sterically stabilized silica spheres with a diameter of 230 nm dried from cyclohexane over several months. Small grains were obtained by mechanically crushing a piece of the ordered sediment. Individual grains were picked up manually using a micromanipulator and connected to the tip of a $10\,\mu$m thick carbon fiber, which was glued to a glass holder beforehand. The colloidal crystal grain used in this study was imaged with a light microscope (see Figure 5.1) and determined to have dimensions of about $2 \times 3 \times 4\ \mu\text{m}^3$.

The experiment was performed at the Coherence Beamline P10 of the high-brilliance storage ring PETRA III in Hamburg. A monochromatic coherent X-ray beam of $8\,$keV photon energy was focused at the sample at $87.7\,$m from the undulator source using the transfocator optics [157] based on compound refractive lenses (CRLs). The CRL optics was positioned at

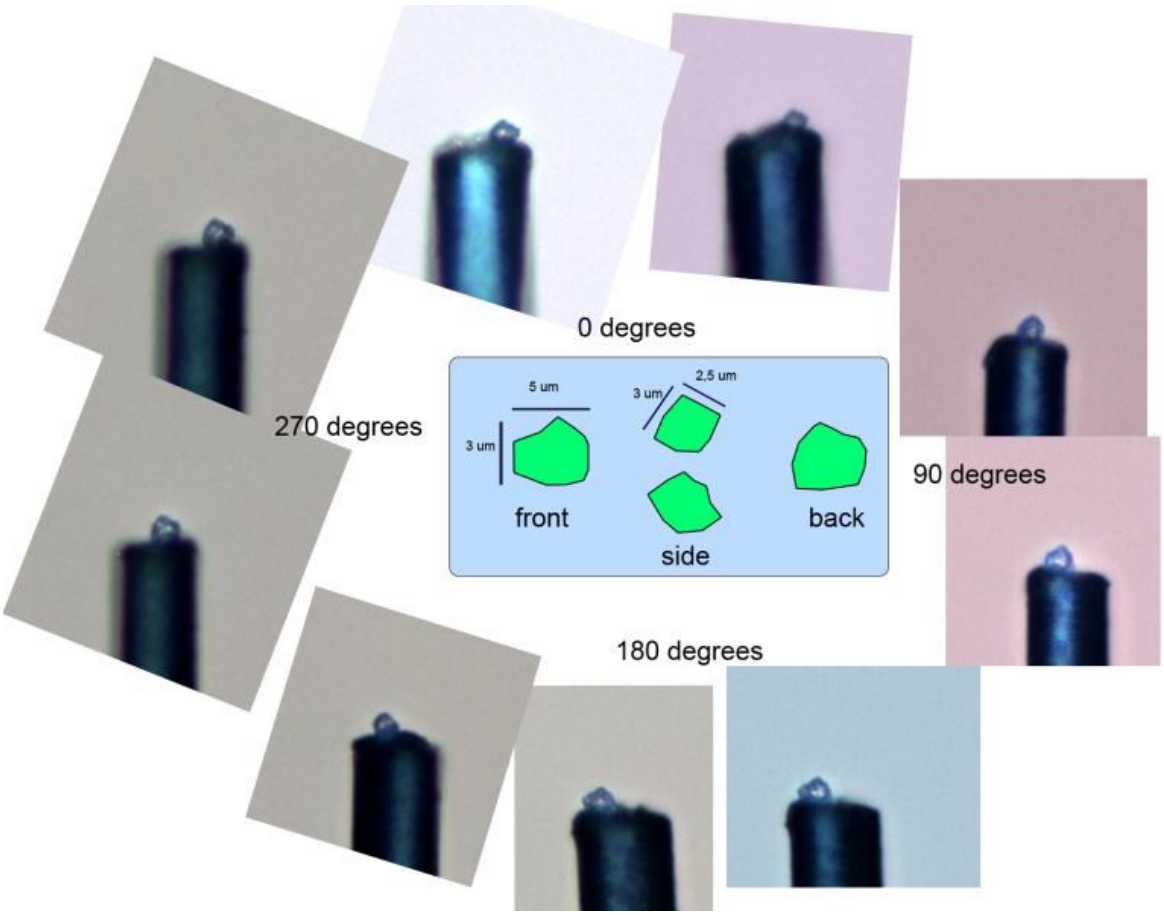

Figure 5.1: Light microscopy image of the colloidal crystal grain mounted on a carbon fiber tip.

2.2 m distance upstream from the sample (see Figure 5.2). A set of horizontal and vertical guard slits 75×75 µm^2 in size, located at 1.5 m distance before the CRL, was used to select a coherent portion of the beam. The size of the focal spot at the sample position was 5.5 µm (FWHM) in horizontal and 3.2 µm (FWHM) in the vertical directions with about 10^{11} photons per second of total intensity [157]. To inhibit the radiation damage the grain was cryo-cooled with the flow of nitrogen (about 100 K). The colloidal crystal grain was mounted on a goniometer, which allows rotation of the sample around the vertical axis. The diffraction data were recorded using a photon-counting pixel detector MAXIPIX [158] positioned in transmission geometry at 5.1 m distance downstream from the sample. In order to reduce air scattering an evacuated tube was inserted between the sample and the detector covering the major part of the optical path. The detector matrix consisted of four readout chips which can be recognized as squares separated by black cross in Figure 5.2(a,b). The total number of pixels was 516×516 and a pixel size was 55×55 µm^2. The resolution value in reciprocal space as defined by the geometry of the experiment and photon energy was $0.437\,\mu\text{m}^{-1}$. For the dimensions of the selected grain that provided the sampling rate about 4.

To access the scattering signal close to the directly transmitted beam the semitransparent beamstop, made of 300 µm thick Si foil, was installed in front of the detector. In addition to that, a Ta disk of 0.5 mm in diameter was glued on the top of the foil to absorb the direct

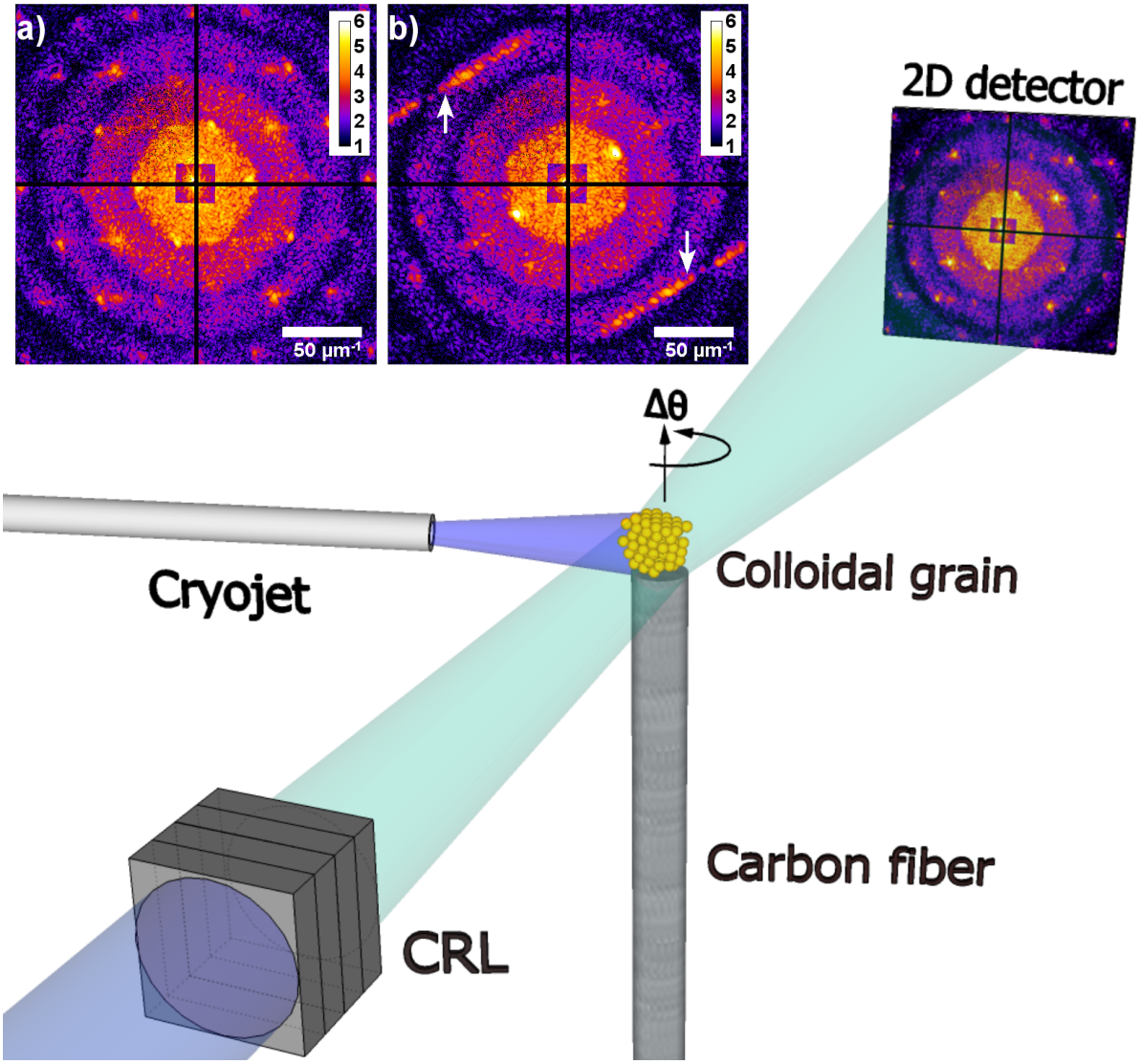

Figure 5.2: The schematic of the experimental setup used in the CXDI experiment. A compound refractive lenses focus the coherent X-ray beam at the crystal grain mounted on a top of carbon fiber. The sample was constantly cooled by a flow of nitrogen using a cryojet. The diffraction data was recorded by 2D detector positioned in the far-field. (a, b) Typical diffraction patterns measured at relative angular positions $\Delta\theta = 61°$ (a) and $\Delta\theta = 165°$ (b). Two elongated rods visible in (b) (indicated by arrows) originate from the presence of planar defects in the crystal grain.

beam completely. The semitransparent beamstop can be recognized as the shadowed area in the center of the diffraction images presented in Figure 5.2(a,b). The recorded signal in this region was multiplied by a mask, which was calculated according to the absorption length for the selected photon energy and the film thickness. The borders of the beamstop were corrupted by the cutting procedure and revealed variations of thickness. In the diffraction patterns that resulted in sharp border line (about 1-2 pixels in width) along the perimeter of the beamstop area. For each pixel in this region the mask coefficient was determined by normalization of the detected signal to the averaged value of intensity in the surrounding. To improve accuracy the results of this normalization were averaged over all diffraction patterns collected during the measurements.

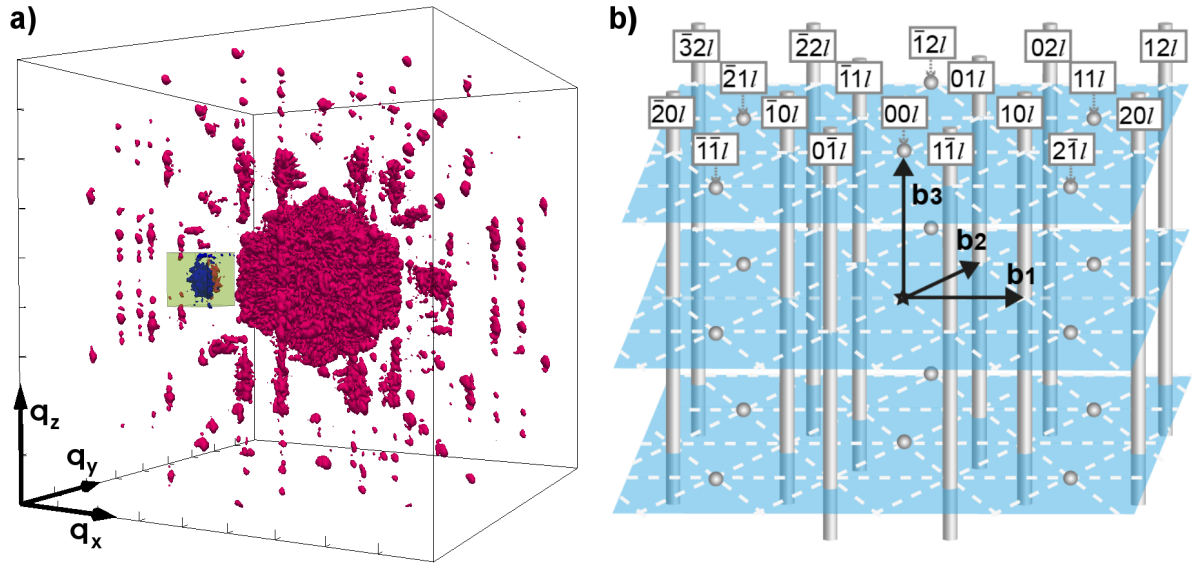

Figure 5.3: (a) 3D reciprocal space intensity map, represented by volume rendering. Length of the arrows correspond to $50\,\mu m^{-1}$. (b) A sketch of the reciprocal lattice with the basis vectors $\mathbf{b_1}$, $\mathbf{b_2}$ and $\mathbf{b_3}$. For specific hk indices, as labeled, the intensity along l is concentrated into distinct Bragg peaks (gray spheres) for $h-k$ divisible by 3, and smeared into Bragg rods (gray rods) for $h-k$ not divisible by 3.

The full dataset consisted of rotation series of 360 diffraction patterns with $0.5°$ angular increment covering the entire reciprocal space. To avoid oversturation of the detector a series of 50 images with 0.02 s of exposure time were collected and summed up for each azimuthal position. In addition to the rotation series several images were recorded with the empty-beam, i.e. when the sample was completely moved out. The average of these images was normalized to the expose time and subtracted as a background from each of the diffraction patterns in the dataset. In Figure 5.2(a,b) two examples of resulted scattering patterns are shown. They contain several Bragg peaks surrounded by the interference speckles and diffuse scattering in between. The detector size allowed to reach reflections up to the forth order measured simultaneously. The visibility

$$V = \frac{I_{max} - I_{min}}{I_{max} + I_{min}}, \tag{5.1}$$

which is a commonly used characteristic quantity of the contrast in the coherent interference pattern [51], was estimated to be about from 75 % to 80 %. It's worth to mention, that although the intensities between the Bragg peaks are rather week in comparison with that in the vicinity of the peaks, this part of recorded signal is highly important for the reconstruction. It encodes information about the relative phases of different reflections and allows to resolve positions of individual scatterers in the unit cell. The concentric circles observed in diffraction patterns represent the form factor of a single colloidal sphere and the number of such circles on the diffraction pattern can be easily converted into a sampling ratio, which results about 8 pixels per a single sphere in direct space.

In Figure 5.3(a) the full 3D reciprocal space map, represented by volume rendering, is shown. The volume of $223 \times 223 \times 223\,\mu m^{-3}$ is sampled by a regular grid of $511 \times 511 \times 511$

voxels, so the transversal size of the voxel corresponds to the pixel size of the diffraction pattern in reciprocal space. All 360 diffraction patterns collected during the rotational scan were used in the merging procedure. The q_x, q_y, q_z coordinates of each measured point in reciprocal space were determined from the transversal coordinates of the pixel on the diffraction pattern and an angular position in the rotational scan. The values of the scattered amplitude on the regular grid were calculated from all measured points in the neighborhood (about 1.5 of the voxel size) using Barnes interpolation [159].

5.2 Two distinguished types of the Bragg reflections

A remarkable feature observed in several of diffraction patterns is a pair of streaks which connect some of the Bragg peaks (see Figure 5.2(b)). These streaks indicate the presence of the plane defects in the crystalline lattice [71] and the intensity modulations along them are directly related to the exact stacking sequence. In the full 3D reciprocal space dataset (see Figure 5.3(a)), that gives rise to well-pronounced Bragg rods which connect some of the reciprocal lattice nodes. Such rodes are oriented perpendicular to the plane of the defect and therefore a specific sample orientation is required for the observation of the whole streak in a single diffraction pattern. In this section we introduce a model, developed by J.-M. Meijer et. al. [160], that describes the relation between the stacking and structure factor.

Let us assume a single crystal composed of hard equal spheres and consisted of finite number of perfect hexagonal layers which form RHCP structure (arbitrary sequence of A, B, C layers without pairs of successive letters). The positions of spheres in the lattice can be described by the hexagonal set of basis vectors $\mathbf{a}_1$, $\mathbf{a}_2$ and $\mathbf{a}_3$, as shown in Figure 5.4(a). The periodicity within single hexagonal layer is described by $\mathbf{a}_1$ and $\mathbf{a}_2$, with $|\mathbf{a}_1| = |\mathbf{a}_2| = a$, which is the interparticle distance, and the interlayer spacing is described by the vector $\mathbf{a}_3$, with $|\mathbf{a}_3| = \sqrt{\frac{2}{3}}a$. Thus, the layers are stacked along the $\mathbf{a}_3$ or [001] direction and the order of the A, B or C layer positions determines the exact stacking sequence. The translation vector which describes the displacement of the any layer with respect to the one, which is underlying, can be expressed as $(\pm\mathbf{c} + \mathbf{a}_3)$, where the in plane vector $\mathbf{c} = (2\mathbf{a}_1/3) + (\mathbf{a}_2/3)$ is taken with positive sign (+) for 'forward' transition from A to B, B to C or C to A. The negative sign (-) corresponds to the 'backward' lateral displacements: for A to C, B to A or C to B (see Figure 5.4(b)).

Based on the hexagonal set of direct space basis vectors, the reciprocal basis vectors $\mathbf{b}_1$ and $\mathbf{b}_2$ and $\mathbf{b}_3$ can be determined in the usual way (see formulas (1.19) or [161]). The scattering vector $\mathbf{q}$ is then described by $\mathbf{q} = h\mathbf{b}_1 + k\mathbf{b}_2 + l\mathbf{b}_3$. A schematic representation of the reciprocal space lattice is shown in Figure 5.3(b).

The blue planes illustrate the hexagonal layers described by $\mathbf{b}_1$ and $\mathbf{b}_2$. Owing to the two-dimensional periodicity inside each hexagonal plane, the scattering intensity in reciprocal space will be concentrated around the integer values of h and k. Stacking faults, inherent in an RHCP structure, break the interlayer periodicity, thus smearing out the diffraction features in rods

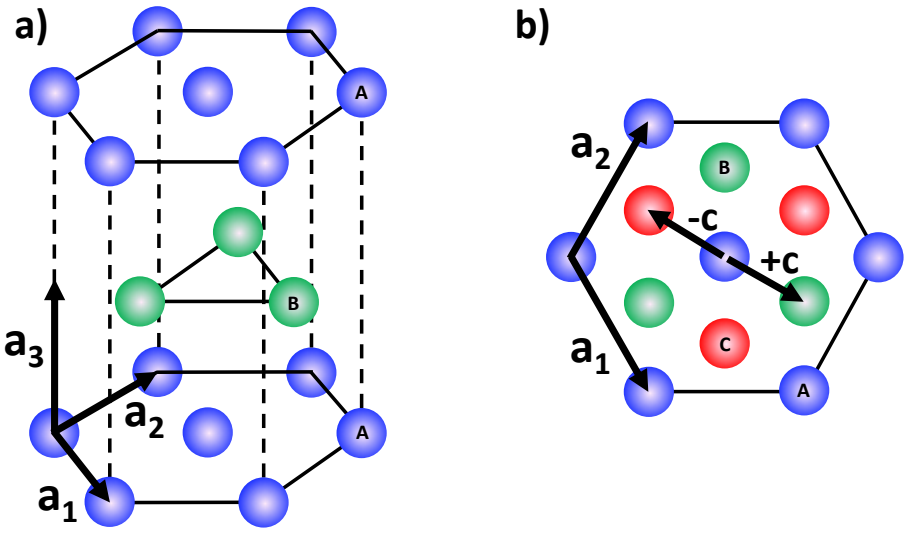

Figure 5.4: (a) The hexagonal unit cell in direct space, together with the basis vectors $\mathbf{a}_1$, $\mathbf{a}_2$ and $\mathbf{a}_3$. (b) Top view of the A, B and C positions and the lateral displacement vector $\mathbf{c}$.

along l. The diffraction amplitude of each subsequent layer along l is dependent on the layer position which, in direct space as described above, will be shifted by the vector $\mathbf{a}_3$ in the direction normal to the layers and by $\pm\mathbf{c}$ laterally. Correspondingly, in reciprocal space the contribution of the *n*th layer to the diffraction amplitude will receive a $\mathbf{q}$-dependent phase shift along l. This phase shift is described by $\exp(i\Delta\phi_n + 2\pi inl)$, where $\Delta\phi_n$ is the phase shift caused by the lateral displacement $\pm\mathbf{c}$, given by a recurrent relation

$$\Delta\phi_n = \Delta\phi_{n-1} \pm 2\pi\frac{(h-k)}{3}. \tag{5.2}$$

Using equation (5.2), we obtain an expression for $l-$profile of the structure factor $S(l)$ of a crystal containing N hexagonal layers as [160]

$$S(l) = \left|\sum_{n=0}^{N-1}\exp(i\Delta\phi_n + 2\pi inl)\right|^2. \tag{5.3}$$

Here, the first layer is $n = 0$ and always assigned an A position. It must be noted that all layers are assumed to be of the same size, i.e. contain the same number of particles. For specific hk indices such that $h-k$ is divisible by 3, the phase shift $\Delta\phi_n$ is always a multiple of 2π and $S(l)$ reduces to the usual result [161]

$$S(l) = \left|\frac{\sin(\pi Nl)}{\sin(\pi l)}\right|^2. \tag{5.4}$$

with well defined Bragg peaks around integer values of l, independent of the stacking sequence and thus resembling a perfectly regular crystal with N planes. In the following the Bragg reflections of this type will be referred as stacking independent. The positions of the stacking

independent reflections are represented by the grey spheres in Figure 5.3(b).

For the other hk indices, $h - k$ not divisible by 3, the $S(l)$ profile will depend sensitively on the exact sequence of the N layers as given by equation (5.3), and the intensity is concentrated into rods along l. These, stacking dependent, reflections are represented by grey rods in Figure 5.3(b).

5.3 Results of 3D reconstruction

The scattered intensity distribution in the vicinity of stacking independent reflections is given by the shape function of the crystal. Relying on that fact, we obtained the estimate of the grain shape, which was afterwards used as a support in further phase retrieval procedure. In reciprocal space we selected a cubic volume $35 \times 35 \times 35$ μm^{-1} surrounding (110) Bragg peak, (see Figure 5.5(a)) and performed reconstruction for this dataset [12]. The results were averaged over

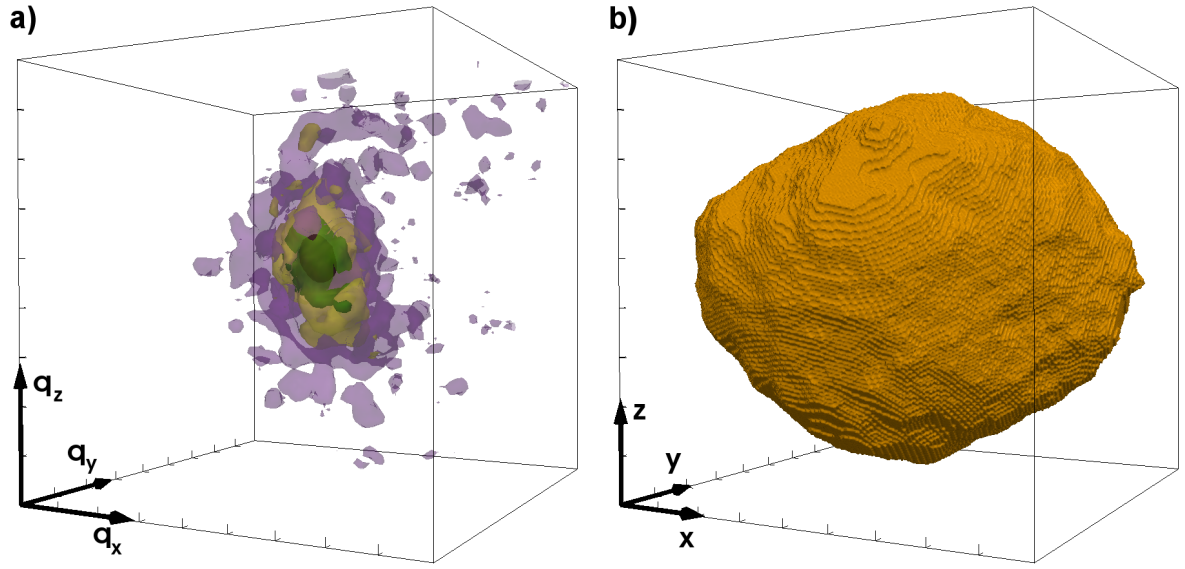

Figure 5.5: (a) 3D scattered intensity in the vicinity of the Bragg peak outlined by a green box in Figure 5.3(a). (b) Reconstruction of 3D shape of the grain in real space averaged over 6 stacking independent reflections. Length of the arrows correspond to 10 μm^{-1} in (*a*), and 1 μm in (*b*).

reconstructions of 6 different stacking independent reflections, and the obtained shape function (see Figure 5.5(b)) was used as a tight support in the reconstruction of the full 3D reciprocal space dataset. That allowed to avoid appearance of the twin image in the results and substantially facilitate the reconstruction procedure. In the phase retrieval process consisted of about 3000 iterations of HIO algorithm combined with ER, this support was several times updated by applying the Shrinkwrap method [74, 78]. The missing regions in the diffraction data were allowed to free evolve with applying an upper boundary for amplitudes which suppress them down to values obtained from the Fourier transform of the support with normalization to the measured amplitudes.

[12] That corresponds to volume of $81 \times 81 \times 81$ pixels.

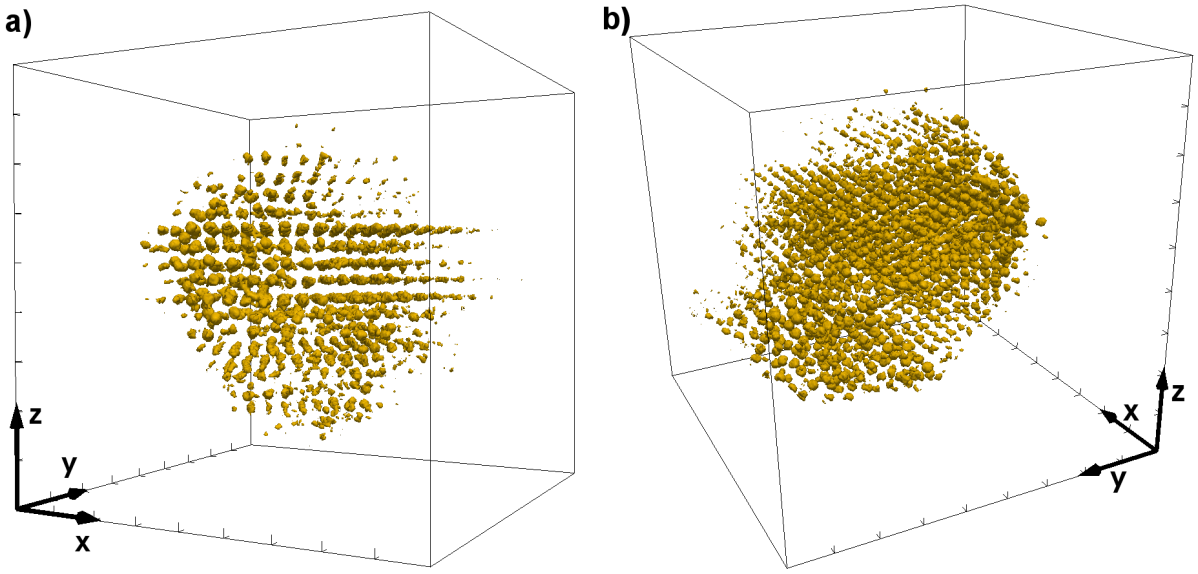

Figure 5.6: (a, b) A volume rendering of the reconstructed 3D electron density distribution in real space, a view from two different perspectives. Length of the arrows correspond 1 µm.

Reconstructed electron density, shown in Figure 5.6 reveals periodic behavior which corresponds to positions of colloidal particles in the crystal grain. In Figure 5.7(a) a slice through one of the layers observed in Figure 5.6(a) is presented. Positions of individual colloidal spheres are clearly resolvable and show perfect hexagonal symmetry. To determine the layer sequence we projected the reconstructed electron density on the $[1\bar{1}0]$ crystallographic direction (see Figure 5.7(b)). In this figure each layer is represented by a horizontal row of periodic electron density. Since the lateral displacement vector **c** belongs to the projection plane, the lateral position of each layer can be directly identified. The first well pronounced layer at the top of the crystal was defined as A layer and the next layer below that as B layer. Then, according to its lateral shift the third layer appears to be C layer, and in this way, all 14 layers were identified. We did not consider the most top layer as well as the most bottom one because they consist of much less number of particles and apparently not well resolved. The resulted stacking sequence $ABCBABCBABCB\underline{CA}$ (from the top to bottom) reveals almost perfect double hexagonal close-packed (DHCP) structure that consists of repeating $ABCB$ compositions and can be represented as alternating A/C layers in an HCP environment. The last two layers, which are underlined, reveal a single stacking fault where the perfect DHCP order is broken.

The determined periodicity in the stacking sequence is a remarkable result because the DHCP structure has not been observed before in colloidal crystals of spheres. In recent work by J.-M. Meijer et.al. [162], it was suggested that the growth of a sedimentary crystal with an RHCP structure probably occurs via the sequential nucleation of hexagonal layers. The interactions are limited to neighbouring layers and, therefore, the DHCP structure could be just one of the many random coincidental realizations of the RHCP structure. Alternatively, it could be an effect of the drying process, in which capillary forces of significant strength act on the colloids [163].

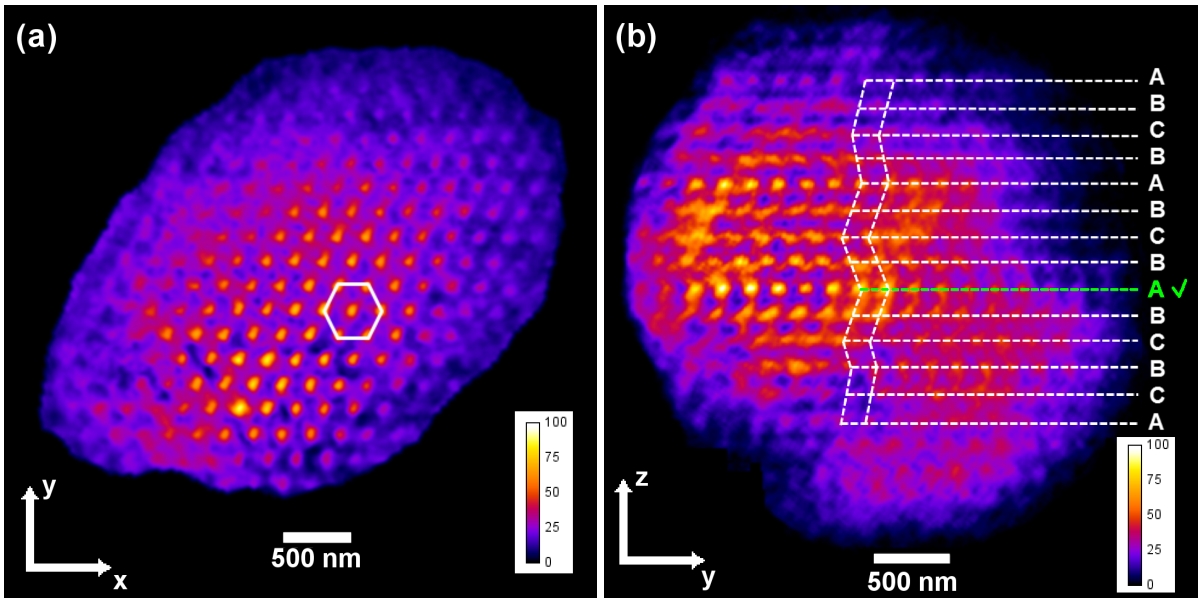

Figure 5.7: (a) Slice through the crystalline plane marked with checkmark and green color in the projection on the right. Well pronounced hexagonal symmetry is outlined by a white hexagon. (b) Projection of the electron density on the $[1\bar{1}0]$ crystallographic direction. Each of the layers is marked by corresponding letter, the saw-like diagram illustrates lateral displacements in the stacking sequence of layers.

5.4 Bragg rod intensity distribution used for determination of the stacking sequence

The intensity modulations along the Bragg rod can be used for determination of the specific stacking sequence by fitting a simple model for a finite number of hexagonally close-packed layers. That enables direct access to structural information of finite-sized crystals on the basis of coherent diffraction measurements, but without the challenging phase retrieval data analysis typical for CXDI. This approach was developed and demonstrated by J.-M. Meijer et. al. [160], where the Bragg rod intensity profiles, extracted form the 3D dataset presented in Figure 5.3(a), were analyzed.

According to the equation (5.3) the contribution of the structure factor $S(l)$ is only dependent on the stacking sequence. Therefore, groups of hkl rods with the same contribution of the form factor given by equation (4.2) can be classified into a general family, for example all rods $10l$, $01l$, $\bar{1}0l$, $0\bar{1}l$, $11l$ and $1\bar{1}l$ belong to the $10l$ family.

Using this model, authors of work [160] performed analysis of the intensity profiles of 3 Bragg rodes extracted from the three-dimensional dataset in reciprocal space. The l values were determined by locating the middle of the rod with respect to the center of the incident beam and scaled with the q value of the (001) Bragg peak, as this is located at $l = 1$. The intensity profiles for the selected Bragg rod families $10l$, $20l$ and $21l$ are plotted in Figure 5.8, where the intensity modulations can clearly be seen. For each profile, the peak positions are similar while the peak amplitudes differ significantly. This is expected, because for each hk combination of indices the structure factor $S(l)$ is the same, while the form factors $P_{hk}(l)$ are

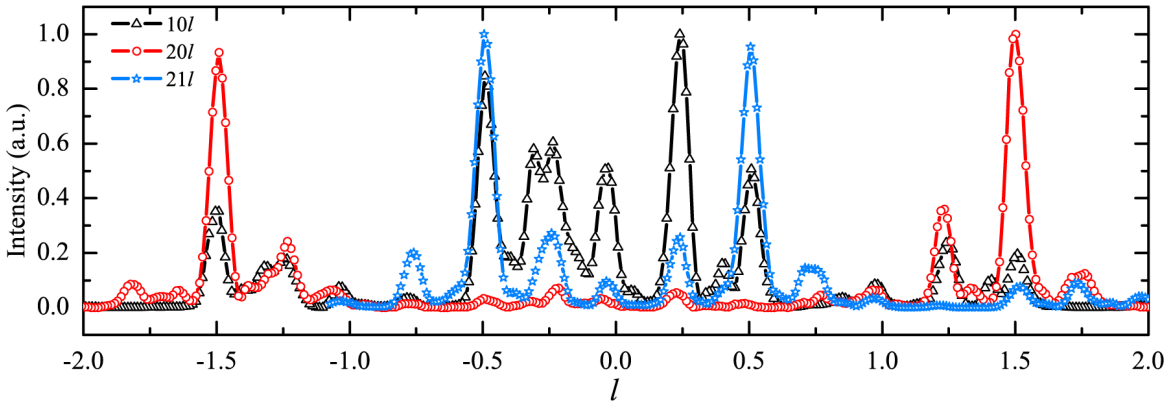

Figure 5.8: Normalized experimental Bragg rod profiles of the $10l$, $20l$ and $21l$ families (lines + symbols), showing distinct intensity modulations along l. The peak positions of the families correspond well, while their amplitudes differ because of the different form-factor and structure factor contributions at the specific hk indices.

different.

The total number of layers N in the studied crystal grain determined by fitting the width of the Bragg peaks along the $11l$ rod was found to be 12. The first layer was defined as A. After careful examination of all possible combinations of A, B, C layers, two sequences that yielded the best match to the experimental profiles were found. Figure 5.9 shows the experimental Bragg rod profiles for the $10l$, $20l$ and $21l$ Bragg rod families, as well as the best fits calculated for the two found sequences. The first stacking sequence, $ABCBABCBABCB$, is a perfect DHCP structure. The second sequence, $ABCBABCB\underline{CA}CB$, is similar to the first one with the exception of the two underlined layers. These two layers cause a stacking defect in the perfect DHCP sequence, and change the repeating B layer to a repeating C layer. The calculated $I(l)$ profiles for the two considered DHCP sequences are very similar in terms of peak positions, shapes and amplitudes and describe all three experimental Bragg rod profiles very well. Small deviations between the experimental data and the model could be explained by our simplified approach to determining $I(l)$. The overall good agreement obtained using the simple model for $I(l)$ shows that the DHCP structure is the dominant packing arrangement of the colloidal spheres present in the studied crystal grain.

These results are very similar to the DHCP stacking that were determined from the 3D reconstruction. The small difference in the number of layers can be explained by the finite size of the grain. The Bragg rod model assumes equal contribution from each layer, while the reconstructed grain clearly shows that the layers at the top and bottom of the grain are much smaller than the those in the center.

5.5 Conclusions

Coherent X-ray diffractive imaging experiment with a single colloidal crystal grain was performed. Coherent X-ray diffraction data which included several Bragg reflections together with

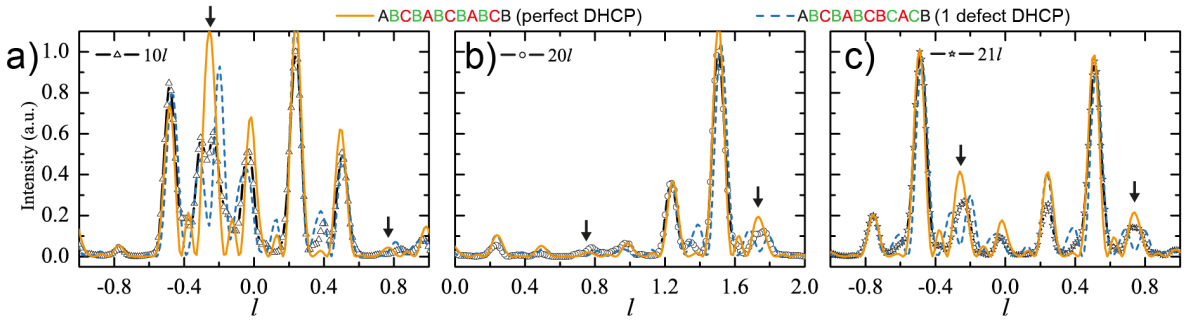

Figure 5.9: Normalized experimental Bragg rod profiles (black lines + symbols) for (a) the $10l$, (b) the $20l$ and (c) the $21l$ families, and modeled profiles for two DHCP structures, a perfect sequence (orange lines) and a sequence with a single stacking fault (blue dashed lines). The specific layer sequence is represented by the A, B and C sequences (given along the top), where each layer can be in either an HCP environment (red) or an FCC environment (green). Arrows indicate the region where the two DHCP model profiles mismatch the most and have a single or double peak, respectively.

surrounding speckles and intensities between them was measured by a rotation series of 2D far-field diffraction patterns. The obtained 3D dataset in reciprocal space was inverted into the electron density distribution in real space using the phase retrieval approach. In the obtained reconstruction positions of individual colloidal particles were resolved in three dimensions. The crystalline structure of the sample was characterized in terms of close-packing of perfect hexagonal layers. The determined stacking sequence revealed 14 layers with almost perfect double hexagonal close-packed structure. This is a remarkable result because the DHCP structure has not been observed for colloidal crystals before. The stacking defect in the lattice was visualized in the projection of the reconstructed electron density on the $[1\bar{1}0]$ crystallographic direction.

The reconstruction results were compared with an independent analysis of the reciprocal space data, based on the theoretical model for a scattered intensity along the Bragg rod for an exact stacking sequence of a finite number of hexagonally close-packed layers. Using this model two stacking sequences of the double hexagonal close-packed type with 12 layers were found to match the experimental data. Both of them are in good agreement with the results of the phase retrieval which shows that the suggested method is a feasible new route for the analysis of finite-size objects.

Our results are of a significant importance for the further progress and developments of CXDI methods with an aim to resolve the three-dimensional structure of nanocrystals with atomic resolution. They are remarkably related to the phase problem in crystallography. In essence, this is a successful experimental realization of the idea suggested by Sayre [65] (for details see Section 2 in Chapter 2), which before that was never applied for X-rays.

Chapter 6

Coherent X-ray diffraction studies of colloidal crystals upon heating

6.1 Heating and annealing treatment of colloidal crystalline structures

An important aspect of possible applications of colloidal systems in photonics and nanolithography is their behavior under heating treatment [164, 165, 166, 167, 168, 169]. On one hand, it has been shown that occasional appearance of defects in a three-dimensional colloidal crystal leads to significant degradation of its optical characteristics [170]. On the other hand, the photonic band gap properties can be deliberately modified by sintering and annealing at elevated temperatures [171, 172, 173]. Furthermore, the glass transition temperature for polymers is known to be greatly influenced by free surfaces [174, 175, 176]. After transferring a free-standing polystyrene film to a substrate, and thus reducing the free-surface-to-volume ratio by a factor of two, an increase of 50 K of the glass transition temperature has been observed [176]. In a range of temperatures below the glass transition temperature of a polymer, the crystal retains a long-range order and undergoes a blue shift of the optical attenuation bands. The temperature region beyond the long range-ordered phase, when the crystal starts to deteriorate, is not well studied, although it has important technological aspects regarding the tolerable temperature range of a photonic device.

Structural studies of spin-coated polystyrene (PS) colloidal thin films during annealing using a combination of grazing incidence small-angle X-ray scattering and optical ellipsometry have been reported by Herzog et al. [168]. It was observed that colloidal particles flatten during annealing, and it was suggested [166] that a coalescence process takes place. Similar observations were made in the work of Chen et al. [167] where the structural evolution of latex films was studied as a function of annealing time using SAXS. Two main effects due to dry sintering were identified: particle deformation and aggregation of particles due to interdiffusion of polymer chains.

Presently, it is not well studied what happens with a 3D assembly of colloidal particles in

a crystal upon heating. We can generally assume that the glass transition temperature of the polymer should directly influence the melting temperature of the colloidal crystal. The physical processes taking place during heating and annealing of the colloidal crystal involve particle shape change, thermal shrinkage, interpolymer diffusion and particle melting [171, 172, 166]. In the present work, we aim at a quantitative investigation of lattice distortions and particle shape changes in colloidal crystals upon heating treatment. For this purpose, we perform a detailed analysis of Bragg peaks in diffraction patterns of PS colloidal crystals measured in situ during incremental heating in a range of temperatures below and above the glass transition temperature of bulk polystyrene (373 K).

6.2 Experimental setup

PS colloidal crystal films were prepared using the vertical deposition method [117, 123]. PS spheres were obtained by polymerization of the aqueous solution of styrene using potassium persulfate as the initiator. The obtained atactic polymer with no control of the side group orientation possesses the typical glass transition temperature T_G of about 373 K [177]. Polydispersity of colloidal particles as measured by dynamic light scattering (DLS) was 2.1 %. Thin glass substrates were inserted into colloidal suspensions contained particles at 1 % volume fraction in water and subsequently dried at 323 K for at least 24 hours. The grown colloidal crystal films consisted of 40 to 50 monolayers of PS spherical particles, depending on the position on a film along the growth direction. Typically, the colloidal crystal films exhibit a cracked texture consisting of single-crystal regions with an average size of several tens of micrometers (as shown in the inset of Figure 6.1).

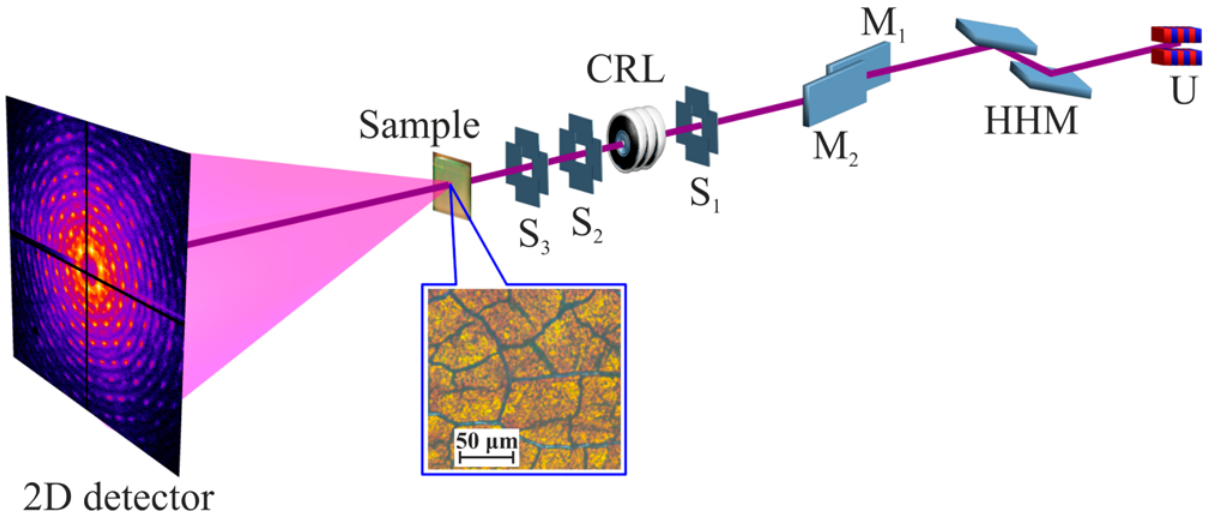

Figure 6.1: Schematic view of the experimental setup: U, undulator source; HHM, high heat load monochromator; M_1, M_2, pair of flat X-ray mirrors; S_1, S_2, S_3, slit systems; CRL, compound refractive lenses. Inset at the sample position: an optical micrograph of the colloidal crystal.

X-ray diffraction experiments were performed at the Coherence Beamline P10 of the PETRA III synchrotron facility at DESY, Hamburg [178]. A sketch of the experimental setup is

shown in Figure 6.1. The synchrotron beam from the undulator source (U) was monochromatized by a high heat load monochromator (HHM) exploiting Si(111) reflection. A pair of flat Si-coated mirrors (M_1, M_2) was used to reject higher harmonics from the undulator spectrum. The slit system (S_1) was used to define the beam size at the entrance of focusing optics. The focusing optics based on compound refractive lenses (CRLs) can be optionally inserted in the beam path at 1.57 m distance upstream the sample position [157]. Two collimating slits (S_2, S_3)were located at 0.8 and 0.3 m upstream a sample and were used to define the size of unfocused beam. The sample was positioned inside a vacuum chamber at 87.7 m distance from the source. Diffraction patterns were recorded by using the 2D detector MAXIPIX with total area of 516×516 pixels and a pixel size of 55×55 μm^2. The detector was positioned at 5.1 m distance downstream the sample. To eliminate parasitic background due to air scattering, an evacuated flight tube was used between sample and detector. In order to protect the detector from the primary beam, the beamstop made of a tungsten cylinder of 3 mm diameter was positioned inside the flight tube.

The glass substrates of colloidal samples were cut to 3×6 mm^2 pieces and mechanically attached to a copper holder plate. The copper plate was fixed to a copper block designed as an insert flange of the sample chamber. The heating of the copper block was supplied via two heating elements connected in parallel and built in the copper block. To provide controlled heat exchange, the copper block with heating elements was separated by a Peltier element from the outer copper part. The latter was connected to a water cooling cycle and acted as a heat sink. The temperature of the sample holder was monitored using two PT100 temperature sensors integrated in the copper block. Temperature and heating power were adjusted using a LakeShore 340 temperature controller. The temperature of the samples was increased incrementally starting from room temperature (T_R = 293 K). Prior to the data collection, a waiting time of 5 minutes was applied at each temperature to reach thermal equilibrium.

We performed two X-ray diffraction experiments (denoted below as experiment A and experiment B) on PS colloidal crystal films grown in similar conditions, but consisting of spherical particles with different size. For both experiments, the size of PS colloidal particles at room temperature was determined by transmission electron microscopy (TEM) and by the Bragg peak and form factor analysis performed in this work (see Table 6.1).

	Particle diameter D, nm		Average lattice parameter $\langle a_{[110]} \rangle$, nm
Experiment	TEM	Form factor analysis (this work)	Bragg peak analysis (this work)
A	415 ± 8	416± 0.2	417± 1
B	386± 8	-	392± 2

Table 6.1: Diameter of PS spherical particles D and average lattice parameter $\langle a_{[110]} \rangle$ determined by different methods at room temperature.

Experiment A was performed at a photon energy of 15 keV using an unfocused beam of

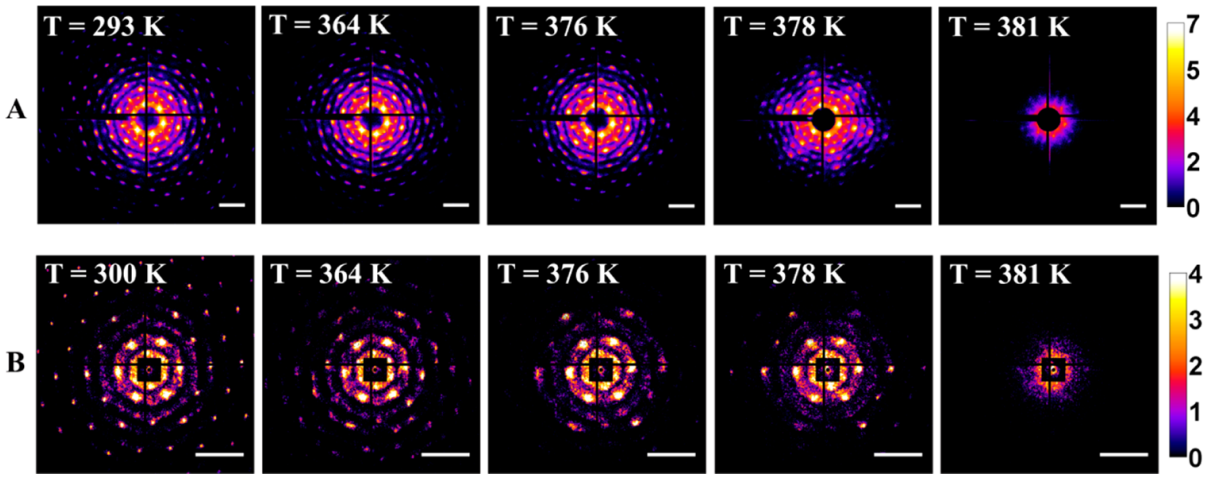

Figure 6.2: X-ray diffraction patterns measured in situ during incremental heating of the PS colloidal crystals in experiments A (top row) and B (bottom row) (see text for details). Intensity values are presented in logarithmic color scale. Scale bar shown for each pattern is $50\,\mu m^{-1}$.

50×50 μm^2 in size, which was chosen to approximately match the single-crystal domain area in a colloidal crystal. At each temperature value, data were collected from the same position on a sample by acquiring a series of 300 frames with exposure time of 0.03 s per frame. The resulting diffraction patterns were obtained by summing up all frames in a series.

The conditions of experiment B were chosen in order to collect ptychographic coherent diffraction patterns from the PS colloidal crystal. Ptychography [85, 86] is a recently developed coherent diffraction imaging technique which enables the study of extended objects with coherent X-rays and involves the scanning of the object in an X-ray beam across the desired field of view. The analysis of ptychographic data collected in experiment B will be reported in a separate publication. In this experiment, a photon energy of 8 keV was selected and the beam was focused at the sample position to a spot size of 2.8(v) $\times$ 3.5(h) μm^2 (vertical $\times$ horizontal) using the CRL focusing optics. To obtain a high degree of transverse coherence in the focused beam, the entrance slits (S_1) in front of the CRL optics were set to a size of 100(v) $\times$ 75(h) μm^2. In order to collect data over a large sample area, the diffraction patterns were measured by raster scanning of a sample on a rectangular grid with 1 μm step size over 11×11 points and acquiring five frames of 0.5 s exposure at each scanned point. Under these experimental conditions, the resolution values in reciprocal space as defined by the incoming beam divergence and photon energy were 0.43 and 2.49 μm^{-1} for experiments A and B, respectively.

6.3 Results

The diffraction patterns measured in experiments A and B under incremental heating of PS colloidal crystals are shown in Figure 6.2. Due to the relatively large unit cell of the colloidal crystals, a number of Bragg peaks can be observed in a single diffraction pattern measured in transmission geometry. In experiment A, Bragg peaks up to the 11th diffraction order were observed at room temperature. For lower photon energy used in experiment B, we observed

seven diffraction orders at room temperature. Due to high spatial coherence of the incoming focused beam used in experiment B, the observed diffraction peaks were broadened and had a complicated internal structure known as X-ray speckles [179] (see Figure 6.2, bottom row). Speckles are produced when the illuminating beam is highly coherent and different regions of the sample introduce different phase shifts. The average speckle size is inversely proportional to the coherently illuminated area of a sample, which is defined by the beam size. Speckle features were not present in the diffraction patterns of experiment A where partially coherent illumination was used.

Inspection of the diffraction patterns presented in Figure 6.2 shows that at temperatures below glass transition temperature T_G there are no strong changes in the structure of diffraction peaks. Only a slight decrease of intensity of higher order Bragg peaks can be observed at elevated temperatures. However, at $T > T_G$, the diffraction patterns evolve very rapidly with temperature. Higher order diffraction peaks gradually decrease in their intensity which indicates the decay of long-range order in the colloidal crystal upon heating. Additionally, we observed a 6-fold modulation of both the intensity of Bragg peaks and the diffuse scattering background in diffraction patterns for experiment A (see Figure 6.2, top row, T = 378 K). This indicates that spherical particles in a colloidal crystal transform to a faceted shape upon dry sintering.

In addition to Bragg peaks, distinct intensity modulations appearing as concentric rings can be observed in the experimental diffraction patterns. These modulations originate from the form factor of a spherical colloidal particle. We extracted the form factor contributions averaged over azimuthal angle for each of the experimental diffraction patterns (see Appendix B for details of an analysis of form factor curves). The form factor curves of PS spherical particles measured from colloidal crystal samples at different temperatures during heating are presented in Figure 6.3 for both experiments. On the one hand, one can observe large number of intensity

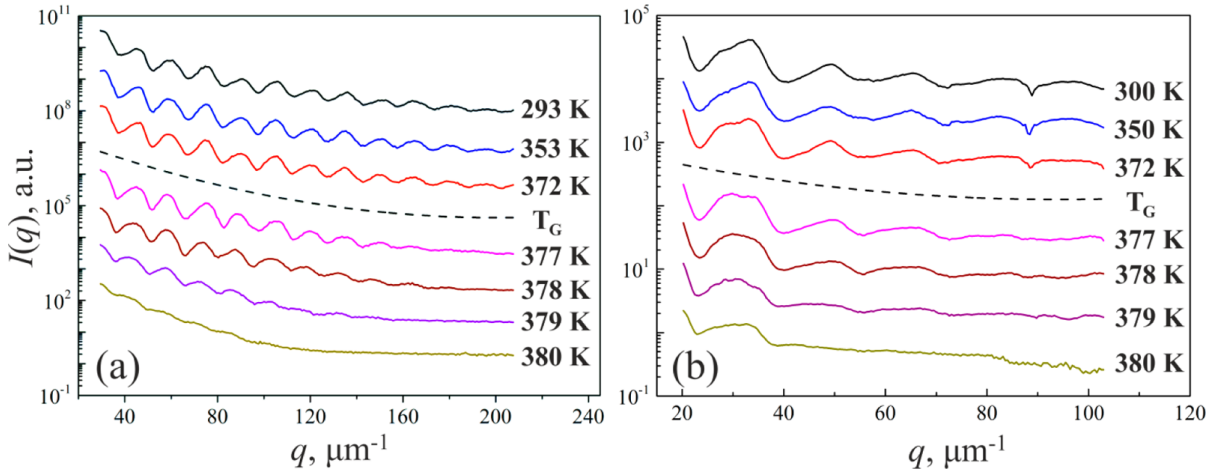

Figure 6.3: Temperature evolution of the form factor curves $I(q)$ of PS spherical particles measured from colloidal crystal samples in experiment A (a) and experiment B (b). The glass transition temperature of PS T_G = 373 K is indicated by the dashed curve.

oscillations in these curves at room temperature. This means that the colloidal particles under study can be well described as hard spheres with a narrow size distribution. On the other hand,

the contrast of intensity oscillations of the form factor curves at high q-values decreases with temperature. This effect can be induced by the particle deformation toward nonspherical shape as well as the broadening of a size distribution of particles.

In order to improve the accuracy of an analysis of Bragg peaks, the scattering signal corresponding to the form factor contribution was subtracted from measured diffraction patterns (see Figure 6.4). The resulting diffraction patterns contain the diffraction peaks typical for re-

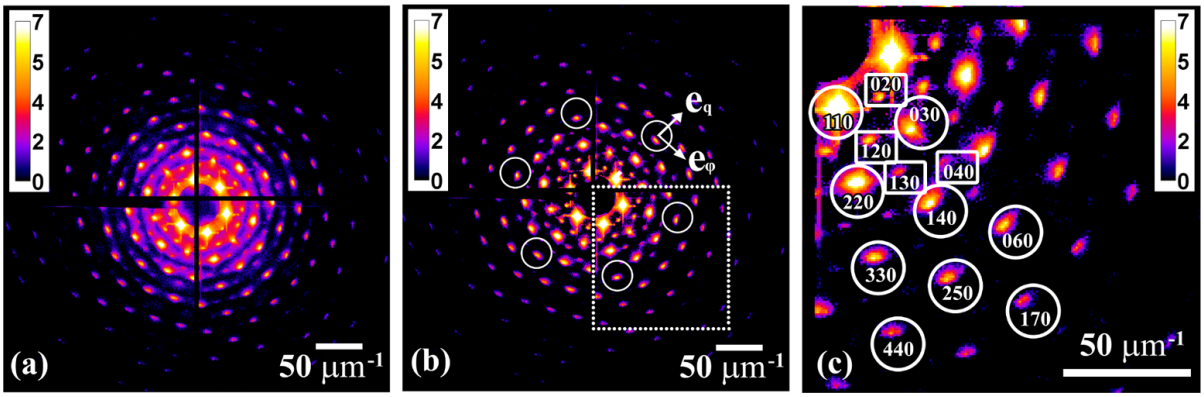

Figure 6.4: (a) X-ray diffraction pattern measured in experiment A at room temperature. (b) Same pattern after subtracting the form factor contribution. (c) Enlarged area of the diffraction pattern highlighted by the dashed square in (b). The analyzed FCC and RHCP peaks are marked by circles and rectangles, respectively. Intensity levels are presented in logarithmic color scale.

flections present in colloidal crystals fabricated by vertical deposition technique. Such crystals often consist of stacked hexagonal close-packed layers which are parallel to the substrate and contain some degree of stacking disorder [117].

The following nomenclature of Bragg peaks indexing was adopted. We consider a hexagonal lattice with the crystal lattice vectors $\mathbf{a}$ and $\mathbf{b}$ lying in the colloidal crystal film and vector $\mathbf{c}$ normal to the film. For the transmission geometry shown in Figure 6.1, an incident beam is perpendicular to the colloidal crystal film, and the Miller index l is always zero. Thus, only indexes h and k can be used for Bragg peak indexing. We will distinguish the two types of $hk0$ reflections: when $(h-k)$ is divisible by three (as indicated in Figure 6.4(c) by circles) and when $(h-k)$ is not divisible by three (as indicated in Figure 6.4(c) by squares) [160]. The reflections of the first type have higher intensity and are stacking-independent, which will be referred as FCC reflections. The reflections of the second type are induced by stacking disorder. These are weaker and will be referred as RHCP reflections. For experiment A, the total number of nine orders of FCC Bragg peaks were considered for the analysis (see Figure 6.4(c)), and for experiment B four FCC orders were analyzed. For both experiments, four orders of RHCP Bragg peaks were evaluated.

6.4 Discussion

To investigate the structural evolution of PS colloidal crystals during heating, we performed a detailed analysis of the measured diffraction patterns shown in Figure 6.2. The following four

parameters of Bragg peaks as a function of temperature were analyzed: Bragg peak position q_B, integrated intensity, and full widths at half-maximum (FWHMs) in radial (w_q) and azimuthal (w_ϕ) directions in reciprocal space. The details of the data processing and Bragg peak evaluation procedures are given in Appendix C. The results of Bragg peak analysis for experiments A and B are shown in Figures 6.5 and 6.6, respectively. The determined widths of Bragg peaks for experiment B were corrected for the instrumental broadening (see Appendix C for details), while for experiment A such a correction was negligible.

According to our results, we can identify four stages of structural evolution of PS colloidal crystals upon heating which are indicated in Figures 6.5 and 6.6 as regions I, II, III, and IV. In the first stage of heating from room temperature to preannealing temperature, T_{PA} = 323 K, no significant variations of peak parameters can be observed. The peak positions q_B slightly decrease due to thermal expansion of the crystal lattice. Interestingly, in this region, the width of higher order peaks in the radial direction (w_q) increases with the increase of the temperature, while the width in the azimuthal direction (w_ϕ) decreases. This indicates a slight increase of the lattice positional disorder along with an annealing effect when crystalline domains become more angular ordered in the plane of a film.

The second stage corresponds to the temperature range between T_{PA} and annealing temperature T_A = 355 K. Within this stage, the Bragg peak positions q_B for both experiments continue to decrease. For experiment A, this decrease is about 0.9 ± 0.5 μm^{-1}, which means that the crystal lattice expands by about 1 % within the second stage of heating treatment. The strongest changes are observed in the temperature evolution of FWHMs of Bragg peaks in the radial and azimuthal directions $w_{q,\phi}$ (see Figures 6.5(c,d) and 6.6(c,d)). Both parameters strongly increase to a maximum at annealing temperature T_A = 355 K. At this temperature, the maximum values of w_q and w_ϕ exceed the room temperature values by 15 – 50%. This increase of peak widths indicates a strong enhancement of the lattice disorder and mosaic spread in the colloidal crystal film at these temperatures. The second temperature range can be referred to as preannealing stage [180].

The third stage corresponds to the temperature interval from T_A to T_G. In this temperature interval, the peak widths $w_{q,\phi}$ drop down from their maximum values, reaching a local minimum at about T_G (see Figures 6.5(c,d) and 6.6(c,d)). The decrease of peak widths at $T_A < T < T_G$ is apparently caused by the relaxation of a PS crystal film and the reduction of the structural disorder due to annealing.

In the last stage of heating from T_G to the melting temperature T_M = 381 K, the PS colloidal crystal film undergoes a fast melting transition. The melting process occurs in a narrow temperature range and ends finally when the Bragg peaks completely disappear at a temperature of T_M. Within this stage, the peak positions q_B increase rapidly and integrated intensities sharply decrease (see Figures 6.5(a,b) and 6.6(a,b)). We attribute this behavior to a coalescence of PS colloidal particles taking place with the increase of temperature. This is further confirmed by the reduction of interparticle distances as it will be seen from the discussion below.

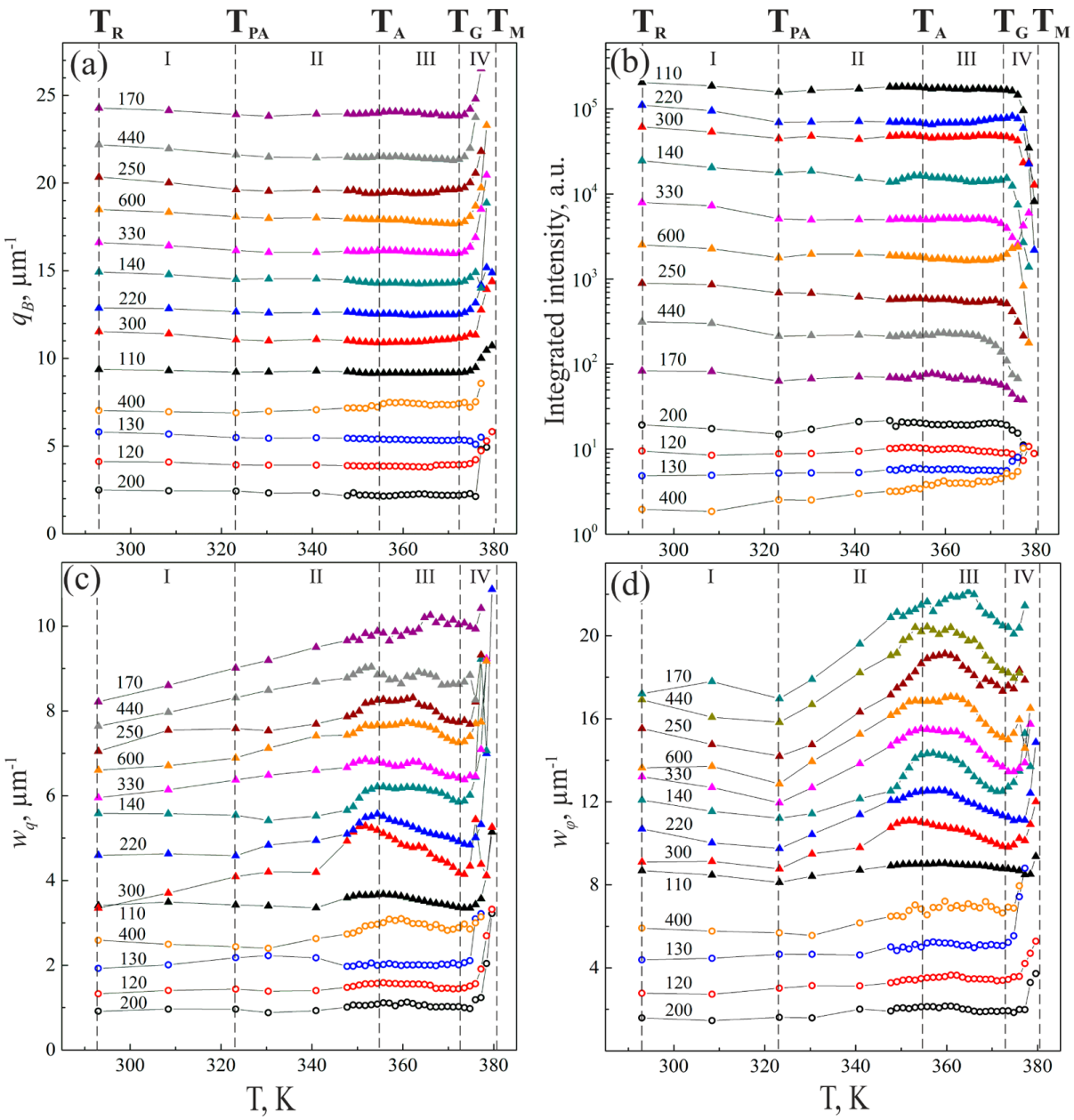

Figure 6.5: Experiment A. Temperature evolution of Bragg peak parameters: peak positions q_B (a), integrated intensities (b), and FWHMs in radial w_q (c) and azimuthal w_ϕ (d) directions. For visibility, all curves were shifted vertically. Reflections of FCC and RHCP types are displayed by triangles and circles, respectively. The curves in (a), (c), and (d) are arranged in the ascending order of the momentum transfer value q; the curves in (b) are in the descending order of the q value.

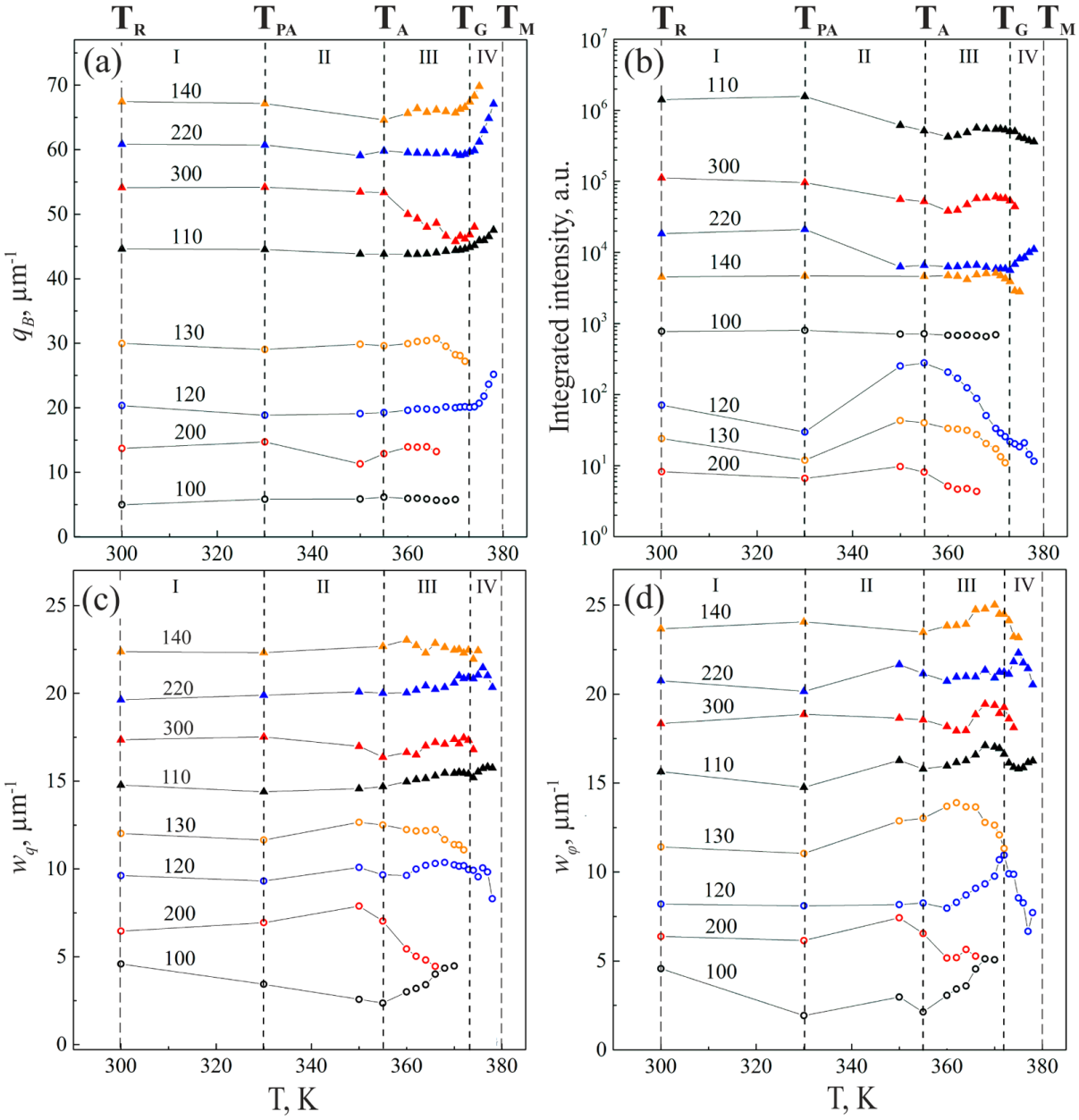

Figure 6.6: Experiment B. Temperature evolution of Bragg peak parameters: peak positions q_B (a), integrated intensities (b), and FWHMs in radial w_q (c) and azimuthal w_ϕ (d) directions. For visibility, all curves were shifted vertically. Reflections of FCC and RHCP types are displayed by triangles and circles, respectively. The curves in (a), (c), and (d) are arranged in the ascending order of the momentum transfer value q; the curves in (b) are in the descending order of the q value.

6.4.1 Williamson–Hall analysis

To perform a quantitative analysis of disorder in colloidal crystal films induced by the thermal treatment we applied the Williamson–Hall (WH) method [35] based on a mosaic block model to our Bragg peak evaluation. This method assumes that the size $L_{q,\phi}$ of the coherently scattering domain (CSD) and the lattice distortions $g_{q,\phi}$ provide independent contributions to the total width $w_{q,\phi}$ of a Bragg peak. For a normal distribution of these parameters, the following relation holds for the total width of a diffraction peak [181]

$$w^2_{q,\phi}(q) = \left\{\frac{2\pi}{L_{q,\phi}}\right\}^2 + (g_{q,\phi}q)^2. \tag{6.1}$$

The WH method was applied to four orders of $hh0$ reflections measured in experiment A (see Figure 6.7(a,b)). The FWHM values used in this analysis were obtained as a result of averaging

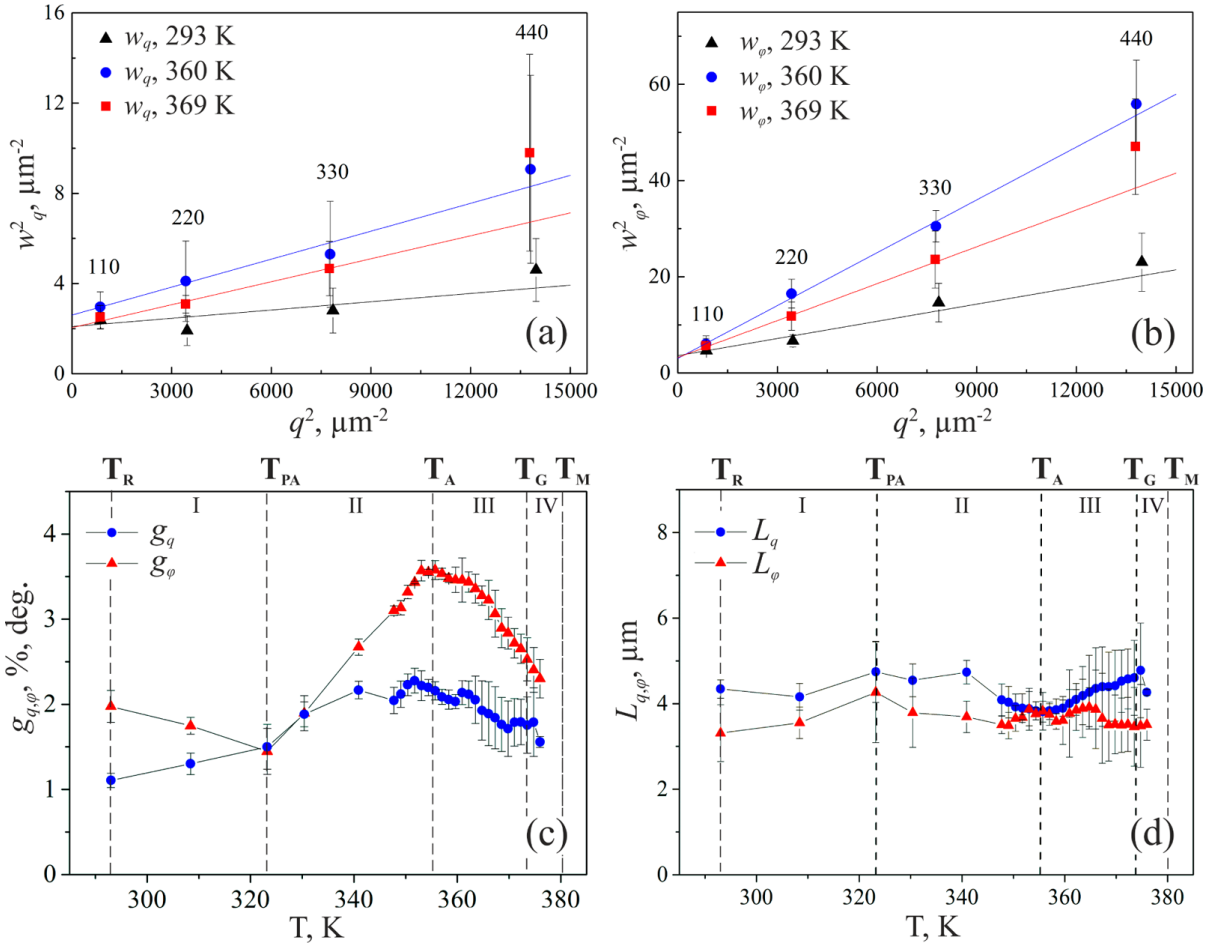

Figure 6.7: (a, b) Williamson–Hall plots obtained using FWHMs of four orders of FCC reflections in radial (a) and azimuthal (b) directions at different temperatures. Solid lines in (a) and (b) represent linear fits to the experimental data. (c) Temperature dependence of the lattice parameter g_q (in percent) and domain misorientation parameter g_ϕ (in degrees). (d) Temperature dependence of the averaged size of CSD $L_{q,\phi}$.

over six equivalent crystallographic directions.

The average values of lattice distortions (g_q), domain misorientations (g_ϕ), and size of CSDs

($L_{q,\phi}$) as a function of temperature are presented in Figure 6.7(c,d). As can be seen in Figure 6.7(c), the temperature evolution of the lattice distortions (g_q) and domain misorientations (g_ϕ) exhibits the four well distinguished temperature intervals discussed earlier. In the first stage, we observe a slight increase of lattice distortions by about 30 % and simultaneous decrease of domain misorientations by about the same amount. In the preannealing stage, both parameters g_q and g_ϕ exhibit especially strong changes: they steadily increase and reach their maxima at the annealing temperature T_A = 355 K. The maximal values of parameters g_q and g_ϕ exceed the corresponding room temperature values by almost 100 %.

The third stage exhibits decrease of parameters g_q and g_ϕ due to a partial annealing process up to the glass transition temperature T_G = 373 K. At the same time the size of CSDs ($L_{q,\phi}$) stays almost constant within the whole temperature range. Both domain sizes were determined to be in the range of 3–5 μm.

Domain sizes evaluated in experiment A prevented us from applying the WH method to experiment B because the illuminated spot on a sample of a few micrometers was about the size of a CSD. Under these conditions, the measured data contain no statistical averaging and WH method could not provide adequate information.

6.4.2 Particle diameter

To determine the temperature evolution of the size of PS spherical particles, we performed an analysis of the form factor curves obtained from experiment A and shown in Figure 6.3(a). With an assumption of hard sphere model, we obtained a linear growth of the particle diameter from room temperature to glass transition temperature T_G (see Figure 6.8). The value of thermal expansion coefficient of $(6.96 \pm 0.35) \times 10^{-5}$ K^{-1} was determined from the results of linear fitting. The obtained value is in excellent agreement with the thermal expansion value of 7×10^{-5} K^{-1} reported in literature [182]. However, at higher temperatures, $T > T_G$, it was not possible to obtain reliable results in the frame of the hard sphere model. We attribute this to the softening of boundaries and shape transformation of initially spherical particles, which was not taken into account in our fitting procedure. Unfortunately, it was not possible to perform similar analysis of the form factor data for experiment B (Figure 6.3(b)) that we attribute to instrumental broadening of Bragg peaks due to beam focusing and higher polydispersity of colloidal particles in this particular sample.

We determined the temperature evolution of an average lattice parameter $\langle a_{[110]} \rangle$ for the [110] crystallographic direction in our colloidal sample shown in Figure 6.8 by analyzing equivalent $hh0$ reflections (see Appendix C for details). As it follows from our analysis, the average lattice parameter value $\langle a_{hh0} \rangle$= 417±1 nm at room temperature is slightly larger than the particle diameter D determined from the form factor data (see Table 6.1). In the temperature range $T_R < T < T_A$, the lattice parameter first increases slightly faster and after T_A changes linearly according to the temperature expansion law of PS spheres (Figure 6.8). However, after reaching the glass transition temperature T_G, the lattice parameter drops down rapidly, indicating a fast

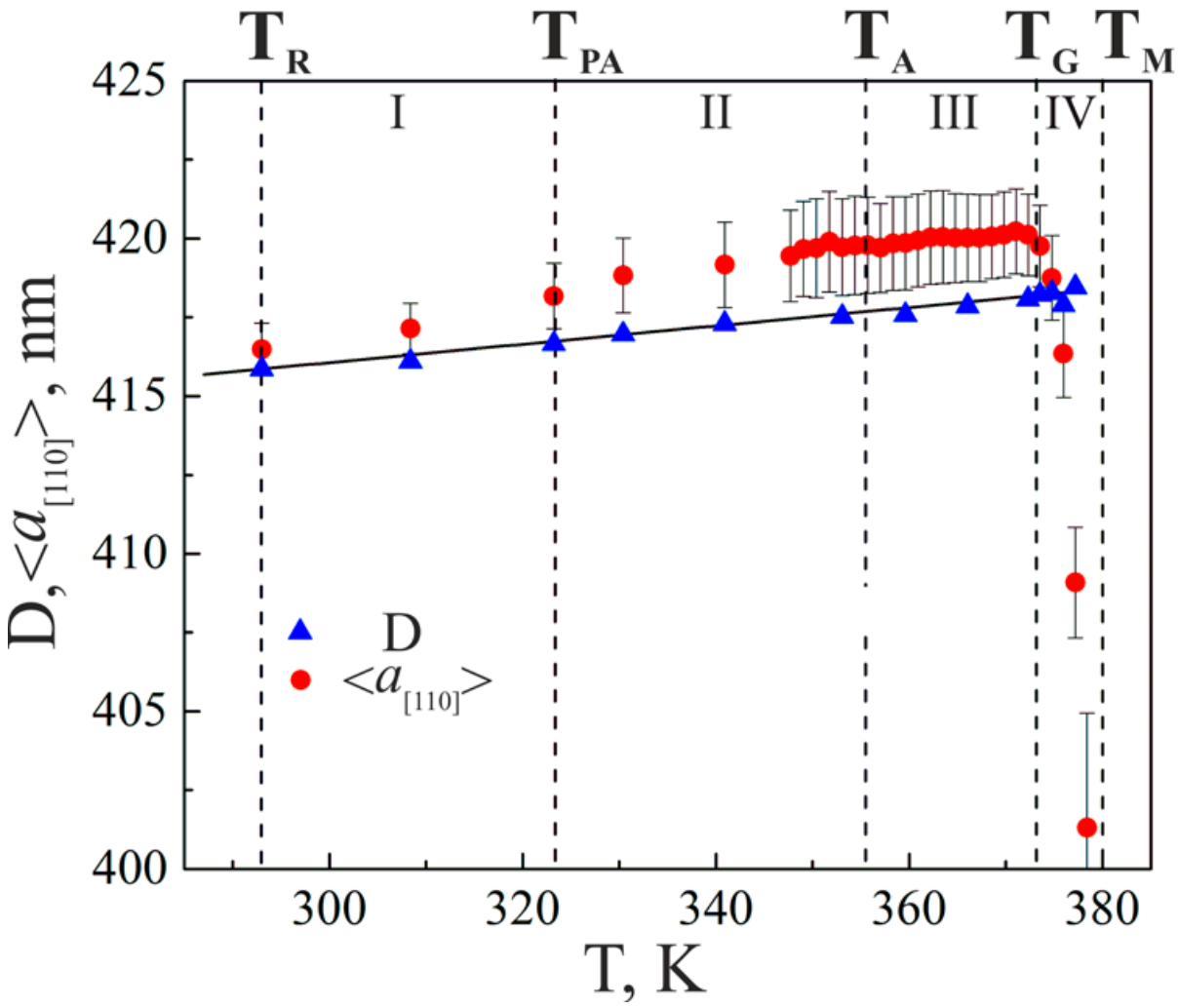

Figure 6.8: Temperature evolution of the PS particle diameter D (shown by blue triangles) and average lattice parameter $\langle a_{[110]} \rangle$ in [110] crystallographic direction (shown by red circles) for experiment A. Thermal expansion function fitted to $D(T)$ is shown by a solid line. The coefficient of linear thermal expansion of PS was determined to be $(6.96 \pm 0.35) \times 10^{-5}$ K^{-1}. Error bars for the particle diameter D are within the symbol size.

shrinkage of the colloidal crystal lattice and coalescence of colloidal particles.

6.4.3 Model of temperature evolution of colloidal crystal

Our analysis of the Bragg peaks and form factor curves suggests the following model of the colloidal crystal evolution during incremental heating (see Figure 9). Two length scales, nanoscopic and mesoscopic, need to be considered. The nanoscopic length scale is about the size of a colloidal particle that is in the range of few hundred nanometers in our case (Figure 6.9, top row). The mesoscopic length scale is related to the size of a coherently scattering domain that is about a few micrometers for colloidal crystals under study (Figure 6.9, bottom row).

On the nanoscopic length scale, we observed linear growth of the average lattice parameter in the wide temperature range $T_R < T < T_G$ that is directly induced by the thermal expansion of closed packed colloidal spheres (see Figure 6.8). At temperatures higher than T_G, the PS

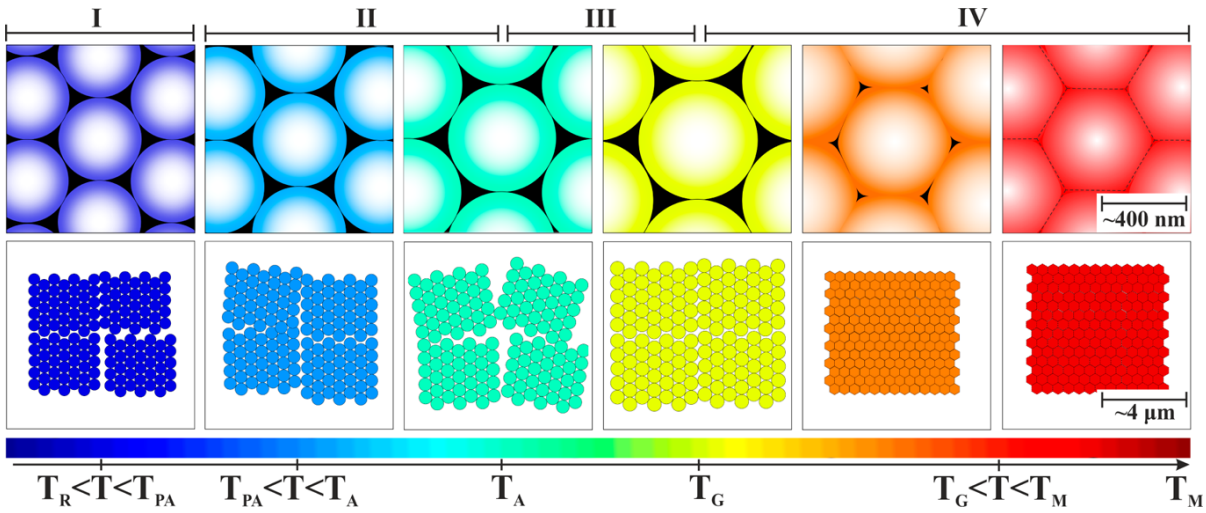

Figure 6.9: Schematic diagram of the structural evolution in a colloidal crystal film under incremental heating at nanoscopic (top row) and mesoscopic (bottom row) length scales.

particles soften and change their shape by flattening in the directions where they touch each other (see Figure 6.9), that leads to the observation of six-fold symmetry in the diffraction pattern shown in Figure 6.2 (top row at T = 378 K). At the same time, this process is statistical in nature and each particle is deformed differently, that leads to the decrease of the long-range order in the crystalline film and is observed as a decrease of intensity of higher order Bragg peaks with the raise of the temperature (see Figure 6.2, $T > 376$ K). At higher temperatures, $T > T_G$, the lattice parameter rapidly decreases that indicates fast shrinkage of the lattice until the crystalline structure completely disappears at the melting temperature T_M= 381 K.

On the mesoscopic length scale of a few micrometers, we did not observe any particular changes in the temperature interval $T_R < T < T_{PA}$, while for higher temperatures $T_{PA} < T < T_G$ the structure of the colloidal film undergoes significant changes (see Figure 6.7(c)). We suggest that, due to the presence of cracks and other microscopic defects in the colloidal crystal film, the orientational correlations of mosaic blocks first increase with temperature. Then at $T > T_A$, a partial annealing process occurs and the crystal lattice becomes more relaxed. At $T > T_G$, the lattice parameter and integrated intensities of Bragg peaks sharply decrease. We attribute such behavior to the coalescence of PS particles with an increase of temperature that is revealed by the decrease of interatomic distances as discussed earlier. This is a consequence of softening of colloidal spheres at the glass transition temperature T_G = 373 K accompanied by interdiffusion of polymer chains [167, 183].

6.5 Temperature evolution of anisotropic properties

In addition to isotropic characteristics, which can be determined through averaging over all accessible crystallographic directions, the diffraction pattern can provide information about anisotropy in the crystal structure. Figure 6.10 shows the temperature dependence of the lattice parameter calculated separately for $[110]$, $[2\bar{1}0]$ and$[\bar{1}20]$ directions, that reveals anisotropic

thermal expansion of the crystal lattice. For each of the directions the corresponding diffraction vector was determined from the positions of all the reflections which belong to this crystallographic direction in a similar way as it was done in previous section. For example, the averaging for $\langle q_{[110]} \rangle$ was performed over ..., $(\bar{2}\bar{2}0)$, $(\bar{1}\bar{1}0)$, (110), (220), ... reflections. The error bars were calculated from standard deviation of a set of data values for the diffraction vector. When the temperature rises up the Bragg peaks disappear starting from higher orders leading to an increase of error of the mean value.

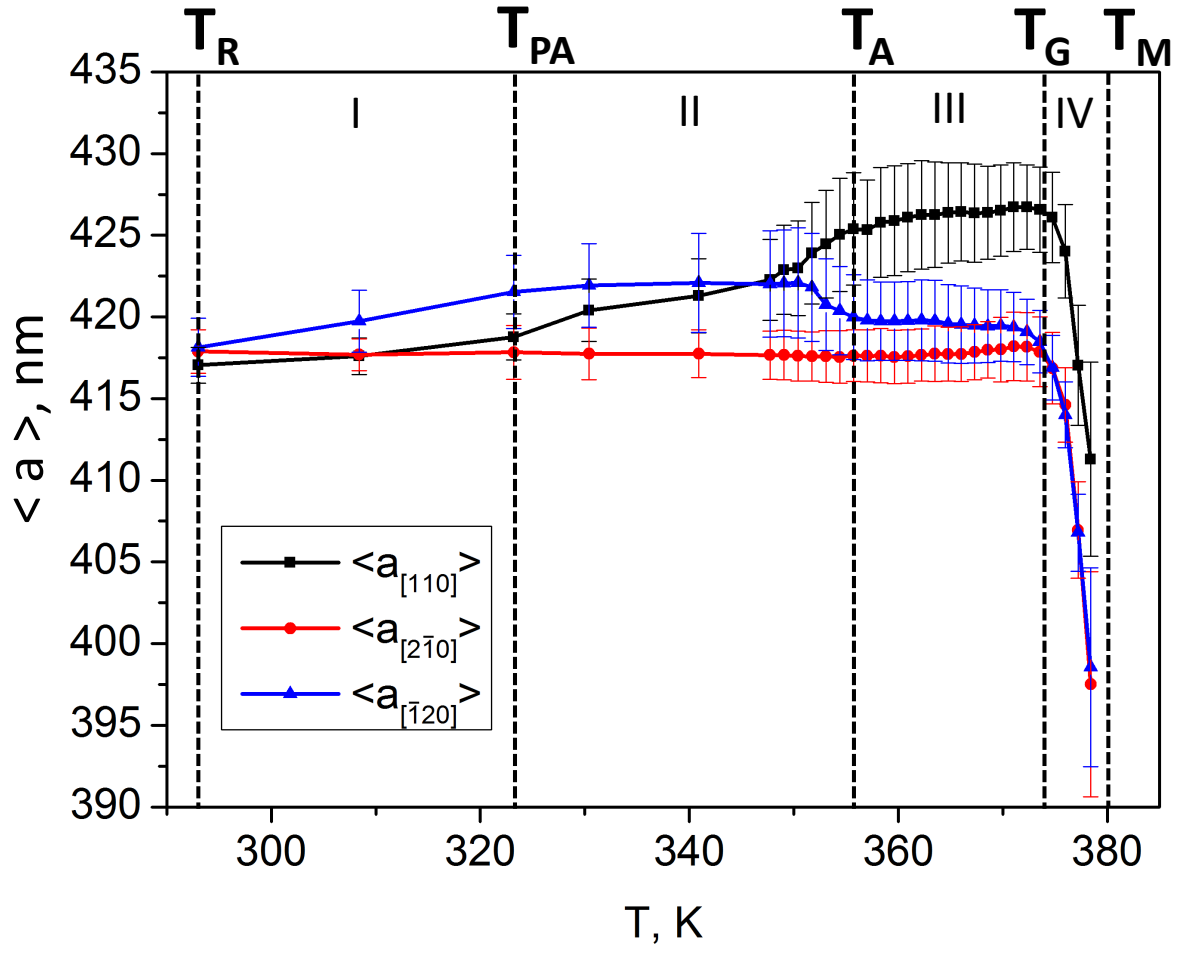

Figure 6.10: Experiment A. Temperature evolution of the average lattice parameter calculated for a family of crystallographic directions, equivalent to $[110]$. The values for measured temperature points higher than 379 K are not shown, because of rather large error bars (> 10 nm).

At room temperature the lattice is rather isotropic and provides value 417 ± 1nm of the lattice parameter which is consistent with the particle diameter, calculated from the form factor analysis (see Table 6.1). Small variations between different directions are within the limits of error (about ± 1 nm) for room temperature T_R. However, with increase of the temperature the lattice parameters behave differently for different directions. The variations start to diverge, gradually at the first stage ($T_R < T < T_{PA}$) and rather rapidly at the second stage ($T_{PA} <$

$T < T_A$). Subsequent expansion (third stage, $T_A < T < T_G$) and shrinking (fourth stage, $T_G < T < T_M$) occur in nearly isotropic way. That matches to the results of the WH analysis, presented in Figure 6.7, which reveals increase of the distortion and domain misorientation parameters at first two stages, and relaxation of the lattice at the third stage. The relaxation process does not lead to anisotropic changes, which can be explained by irreversible character of the lattice deformation occurred at previous stages. Remarkably, the lattice parameter in $[2\bar{1}0]$ direction does not reveal significant increment at the first three stages. We attribute this to constriction of crystal that prevent expansion in this direction. Gradual vanishing of higher order diffraction peaks observed at the fourth stage is a consequence of the decay of long-range order in the crystal lattice. In Figure 6.5(b) that can be recognized as a steep decrease of the integrated intensity starting from higher order Bragg peaks.

In addition to these characteristics, averaged over all Bragg peaks within each order, we have analyzed the temperature dependence of the reflections intensities separately. Figure 6.11 shows the diagrams of the ratios between intensity at the Bragg peaks and the form factor (the values of the form factor was taken from the curves presented in Figure 6.3 (a)). In other words, this approach allows to separate the Bragg diffraction from the contribution of the form-factor. The resulted diagram can be considered as being directly connected to the structure factor and its temperature evolution illustrates structural changes in the crystalline order in the colloidal film. Due to the presence of a long-range order such a diagram calculated for the room temperature displays a lot of intense high order peaks (see Figure 6.11(a)). With increase of the temperature such pattern reveals no essential changes up to the glass transition point T_G, where it becomes asymmetric (see Figure 6.11(b)). At this temperature, higher order Bragg peaks in the horizontal direction start to disappear which indicates an anisotropic decay of the long-range order. The subsequent degradation occurs mainly in the 'median' crystallographic direction such as [100], [010] and $[\bar{1}10]$, while the 'main' directions, such as [110], $[2\bar{1}0]$ and $[\bar{1}20]$ reveal more resistance. That leads to the star-like pattern in the next diagram corresponding to $378\,\mathrm{K}$ (see Figure 6.11(c)). Such 'star' shape behavior can be also a strong indication of the shape change of the colloidal particles due to dry sintering as depicted in Figure 6.9 (top row). At the last presented temperature, $380\,\mathrm{K}$, almost all diffraction peaks are gone (see Figure 6.11(d)). Notably, the pattern becomes highly asymmetric, which indicates that the final deterioration of the crystalline lattice occurs not simultaneously for different crystallographic directions.

6.6 Conclusions

In situ X-ray diffraction studies of structural evolution of colloidal crystal films formed by polystyrene spherical particles upon incremental heating are reported. The Bragg peak parameters, such as peak position, integrated intensity, and radial and azimuthal widths were analyzed as a function of temperature. A quantitative study of colloidal crystal lattice distortions and mosaic spread as a function of temperature was carried out using Williamson–Hall plots based

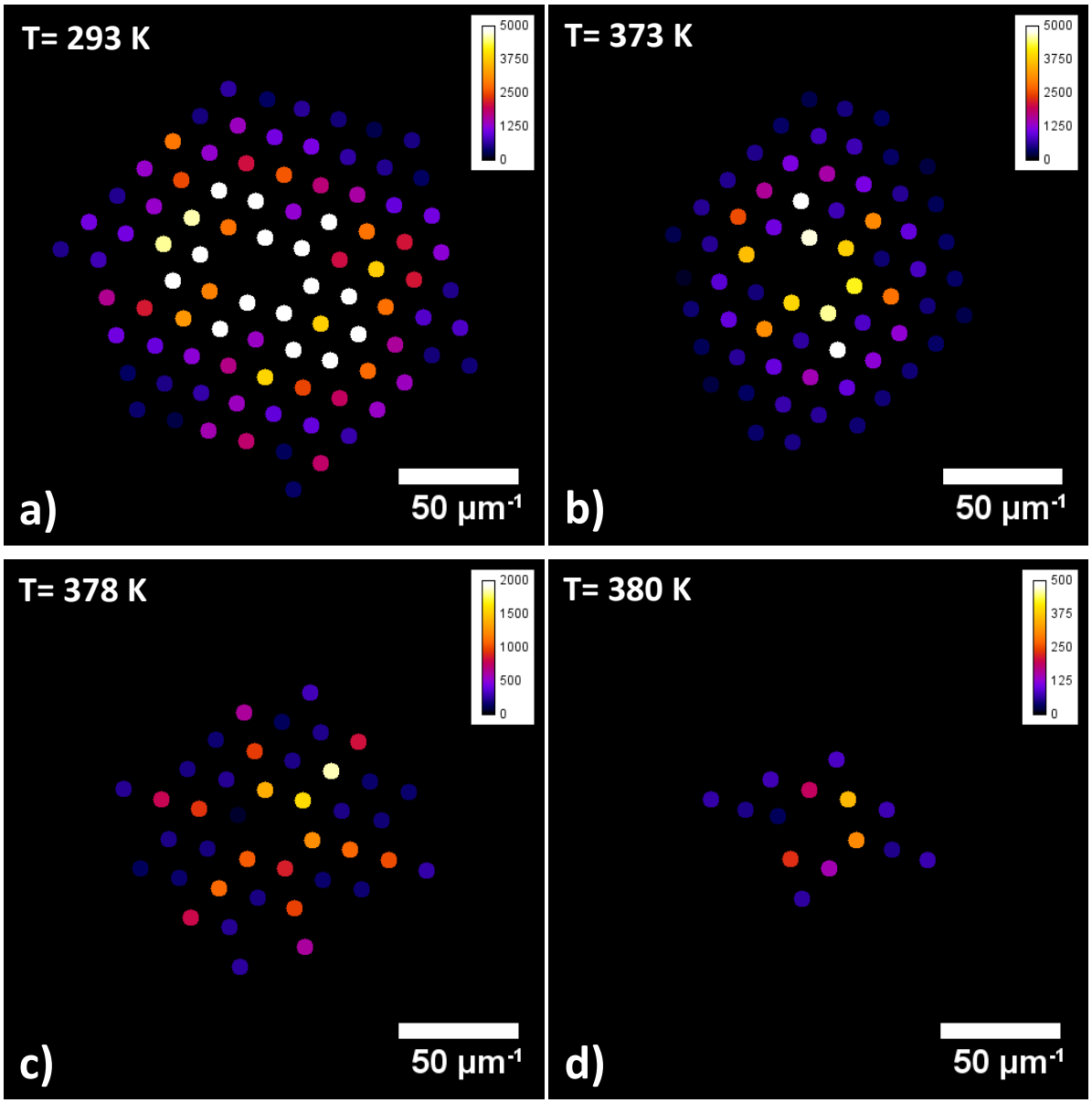

Figure 6.11: Experiment A. Diagrams of the ratio of intensity at the Bragg peaks and diffuse scattering around each peak. Four different temperatures are shown.

on mosaic block model. The temperature dependence of the diameter of polystyrene particles was obtained through the analysis of Bragg peaks, and the form factor contribution extracted from the diffraction patterns. Four stages of structural evolution in a colloidal crystal upon heating were identified. Based on this analysis, a model of the heating and melting process in the colloidal crystal film is suggested.

In situ X-ray diffraction studies of structural evolution of colloidal crystal films at different temperatures were performed using the high resolution X-ray scattering setup at the P10 beamline of the PETRA III synchrotron source. The high quality colloidal crystal films formed by polystyrene spherical particles were investigated upon incremental heating in a wide temperature range from 293 to 381 K.

The structural changes in the colloidal crystal induced by incremental heating were revealed by a detailed analysis of the measured Bragg peaks. The parameters of diffraction peaks, such as the position of the peak, integrated intensity, and the peak widths in radial and azimuthal directions of reciprocal space, were analyzed as a function of temperature. The Williamson–Hall method based on a mosaic block model was applied to determine the lattice distortions and the angular spread of crystalline domains in a colloidal crystal film. A significant increase of lattice distortion and domain misorientation parameters in a polystyrene colloidal crystal was revealed around the annealing temperature of 355 K. From the analysis of the form factor scattering signal and Bragg peak positions, we observed a linear behavior of the thermal expansion of PS spherical particles. The determined coefficient of thermal expansion is in good agreement with the literature. As a result of our analysis, we have identified four stages of structural evolution of a colloidal crystal upon heating: steady state, preannealing, shape transformation, and crystal melting. We finally proposed a model of structural evolution of a colloidal crystal upon incremental heating on the nanoscopic and mesoscopic length scales.

The results of our investigation provide valuable information for fabrication process of photonic devices based on colloidal crystals and tuning their properties by changing the operating temperature. In our future work, we are aiming for the detailed study of defect behavior [184] under incremental heating of colloidal crystals. Of special interest are dynamics studies of colloidal crystals in the pump–probe experiments [185], which could provide unique information on dynamics of the colloidal crystal film as well as on the ultrafast melting process of the polystyrene.

Chapter 7

Summary

This thesis discusses different theoretical and experimental aspects of structural investigation of mesoscopic materials using coherent X-rays. The results of three independent studies are presented.

In the first study a theoretical approach to the numerical solution of the Takagi-Taupin equation in the case of finite size 3D crystal of arbitrary shape is developed. A suggested modification of the Takagi-Taupin equations offers a convenient way to solve them numerically using an integration grid, which is invariable with respect to the angular deviation from the exact Bragg condition. As a result, the complex amplitude distributions of the transmitted and diffracted waves can be calculated. Propagation to the far-field gives the amplitude and phase distribution on the diffraction pattern that corresponds to a specific cross-section in reciprocal space. By performing a series of such calculations a full 3D reciprocal space dataset in the vicinity of the corresponding reciprocal lattice node can be constructed. Then, the complex function of the object in real space can be obtained by the inverse Fourier transformation.

Using this model we performed simulations of the dynamical diffraction on a perfect crystal of gold of cubic shape for $100\,\mathrm{nm}$ and $1\,\mu\mathrm{m}$ size. For a small crystal the result of our calculations was in full agreement with the kinematical theory. However, in the simulations for the large crystal artifacts both in reciprocal and real space were observed due to dynamical scattering effect. The contributions of different phenomena, such as refraction, absorption and cross-coupling between the diffracted and transmitted waves were analyzed separately. Based on the analytical derivations we developed a straightforward way to correct the results of reconstructions for the effects of refraction and absorption. Such corrections, applied to the results of the simulations, demonstrates a complete removal of corresponding contributions in the real space reconstruction. The residual artifacts in the amplitude and phase distributions are attributed to the cross-coupling of the diffracted and transmitted waves in the crystal. Additional simulation for a practical case of a Bragg CXDI experiment with a hemispherical Pb particle of $750\,\mathrm{nm}$ size was performed.

The developed model was used for a simulation of the angular dependence of the phase of the transmitted wave in the case of thin crystalline plate infinite in two dimensions. Small

variations of this phase observed in the vicinity of the Bragg angle have a purely dynamical nature. Such variations are related to the structure factor, therefore, this demonstration is of importance for further development of method of obtaining such information from experimentally measured data.

In the second part, CXDI experiment with a single colloidal crystal grain was performed. Coherent X-ray diffraction data which included several Bragg reflections together with surrounding speckles and intensities between them was measured by a rotation series of 2D far-field diffraction patterns. The obtained 3D dataset in reciprocal space was inverted into the electron density distribution in real space using the phase retrieval approach. In the obtained reconstruction positions of individual colloidal particles were resolved in three dimensions. The crystalline structure of the sample was characterized in terms of close-packing of perfect hexagonal layers. The determined stacking sequence revealed 14 layers with almost perfect double hexagonal close-packed structure. This is a remarkable result because the DHCP structure has not been observed for colloidal crystals before. The stacking defect in the lattice was visualized in the projection of the reconstructed electron density on the $[1\bar{1}0]$ crystallographic direction.

The reconstruction results were compared with an independent analysis of the reciprocal space data, based on the theoretical model for a scattered intensity along the Bragg rod for an exact stacking sequence of a finite number of hexagonally close-packed layers. Using this model two stacking sequences of the double hexagonal close-packed type with 12 layers were found to match the experimental data. Both of them are in good agreement with the results of the phase retrieval which shows that the suggested method is a feasible new route for the analysis of finite-size objects.

Our results are of a significant importance for the further progress and developments of CXDI methods with an aim to resolve the three-dimensional structure of nanocrystals with atomic resolution. They are remarkably related to the phase problem in crystallography. In fact, this is a successful experimental realization of the ideas suggested by Sayre [65].

In the third part in situ X-ray diffraction studies of structural evolution of colloidal crystal films formed by polystyrene spherical particles upon incremental heating are reported. The Bragg peak parameters, such as peak position, integrated intensity, and radial and azimuthal widths were analyzed as a function of temperature. A quantitative study of colloidal crystal lattice distortions and mosaic spread as a function of temperature was carried out using Williamson–Hall plots based on mosaic block model. The temperature dependence of the diameter of polystyrene particles was obtained through the analysis of Bragg peaks, and the form factor contribution extracted from the diffraction patterns. Four stages of structural evolution in a colloidal crystal upon heating were identified. Based on this analysis, a model of the heating and melting process in the colloidal crystal film is suggested.

In situ X-ray diffraction studies of structural evolution of colloidal crystal films at different temperatures were performed using the high resolution X-ray scattering setup at the P10 beamline of the PETRA III synchrotron source. The high quality colloidal crystal films formed by polystyrene spherical particles were investigated upon incremental heating in a wide tempera-

ture range from 293 to 381 K.

The structural changes in the colloidal crystal induced by incremental heating were revealed by a detailed analysis of the measured Bragg peaks. The parameters of diffraction peaks, such as the position of the peak, integrated intensity, and the peak widths in radial and azimuthal directions of reciprocal space, were analyzed as a function of temperature. The Williamson–Hall method based on a mosaic block model was applied to determine the lattice distortions and the angular spread of crystalline domains in a colloidal crystal film. A significant increase of lattice distortion and domain misorientation parameters in a polystyrene colloidal crystal was revealed around the annealing temperature of 355 K. From the analysis of the form factor scattering signal and Bragg peak positions, we observed a linear behavior of the thermal expansion of PS spherical particles. The determined coefficient of thermal expansion is in good agreement with the literature. As a result of our analysis, we have identified four stages of structural evolution of a colloidal crystal upon heating: steady state, preannealing, shape transformation, and crystal melting. We finally proposed a model of structural evolution of a colloidal crystal upon incremental heating on the nanoscopic and mesoscopic length scales. The results of our investigation provide valuable information for fabrication process of photonic devices based on colloidal crystals and tuning their properties by changing the operating temperature.

Chapter 8

List of Abbreviations

SASE	Self Amplification of Spontaneous Emission
XFEL	X-ray free-electron laser
3D	Three-dimensional
2D	Two-dimensional
FWHM	Full width at half maximum
EXAFS	Extended X-ray Absorption Fine Structure
XANES	X-ray Absorption Near-Edge Structure
KB	Kirkpatrick-Baez (mirrors)
CRL	Compound refractive lens
FZP	Fresnel zone plate
SEM	Scanning electron microscopy
SAXS	Small-angle X-ray scattering
SANS	Small-angle neutron scattering
CXDI	Coherent X-Ray Diffractive Imaging
ESW	Exit surface wave
ER	Error Reduction algorithm
HIO	Hybrid Input-Output algorithm
GHIO	Guided Hybrid Input-Output algorithm
PRTF	Phase retrieval transfer function
PIE	Ptychographic Iterative Engine
ePIE	Extended Ptychographic Iterative Engine
FTH	Fourier Transform Holography
FCC	Face centered cubic (structure)
HCP	Hexagonal close-packed (structure)
RHCP	Random hexagonal close-packed (structure)
DHCP	Double hexagonal close-packed (structure)
DLS	Dynamic light scattering
PS	Polystyrene
WH	WilliamsonHall (method)
CSD	Coherently scattering domain

Acknowledgements

First of all I thank my parents for supporting me throughout my studies. I would like to express gratitude for my advisors, Dr. Ivan Vartaniants and Prof. Dr. Edgar Weckert for their supervision and useful ideas concerning my work. Oleksandr Yefanov, Max Rose and Oleg Gorobtsov are thanked for carefully reading of my thesis. I appreciate amicable support of Dina Sheyfer, Pavel Lytaev and Svitozar Serkez during the manuscript preparation.

I would like to thank Oleksandr Yefanov for his invaluable support and useful ideas concerning my work on the simulations of dynamical effects on a finite size crystals. Edgar Weckert and Vladimir A. Bushuev are thanked for many fruitful discussions. The simulations of the phase of the transmitted amplitude were performed together with Oleg Gorobtsov.

The work on the 3D Coherent X-ray diffraction imaging with a single colloidal crystal grain is the result of a close collaboration with the van't Hoff Laboratory for Physical and Colloidal Chemistry at the Utrecht University, The Netherlands. I would like to express gratitude for Janne-Mieke Meijer and Andrei V. Petukhov for the sample preparation, analysis of the Bragg rod intensity profiles and help during the measurements. DESY is gratefully acknowledged for the beamtimes allocation. The P10 beamline stuff is thanked for the excellent technical support. I appreciate the contribution from all my colleagues at The Coherent X-Ray Scattering and Imaging Group at DESY in Hamburg, in particular, Roman Dronyak. Oleksandr Yefanov is thanked for his contribution to the measurements, providing the software for the phase retrieval and invaluable support in the data analysis. The experiment would not be possible without the GINI-X setup [186], kindly provided by Institut für Röntgenphysik, Göttingen, Germany. Sebastian Kalbfleisch and Tim Salditt are thanked for the technical support.

The coherent X-ray diffraction studies upon heating were performed in a close collaboration with the Shubnikov Institute of Crystallography of Russian Academy of Science and the van't Hoff Laboratory for Physical and Colloidal Chemistry at the Utrecht University, The Netherlands. I would like to express gratitude for Elena A. Sulyanova for invaluable contribution to the data analysis; Alexey Zozulya for very productive ideas and successful experimental realization; Janne-Mieke Meijer for the sample preparation and helpful discussions. Michael Sprung and Sergey Bondarenko are thanked for the excellent technical support. I appreciate the contribution from all my colleagues at The Coherent X-Ray Scattering and Imaging Group at DESY in Hamburg, in particular, Sergey Lazarev. We acknowledge the support of the project and fruitful discussions with Edgar Weckert, support in the use of GNOM program provided by Vladimir V. Volkov, and fruitful discussions with Vladimir M. Kaganer and Petr V. Konarev. Partial funding by the Russian Foundation for Basic Research (Grant 14-22-00098) is acknowledged.

This work was supported by BMBF Proposal 05K10CHG Coherent Diffraction Imaging and Scattering of Ultrashort Coherent Pulses with Matter in the framework of the German-Russian collaboration Development and Use of Accelerator-Based Photon Sources and the Virtual Institute VH-VI-403 of the Helmholtz Association.

Chapter 9

Own publications

Publications directly related to the thesis

1. A. V. Zozulya, J.-M. Meijer, A. G. Shabalin, A. Ricci, F. Westermeier, R. P. Kurta, U. Lorenz, A. Singer, O. Yefanov, A. V. Petukhov, M. Sprung, and I. A. Vartanyants. In situ X-ray crystallographic study of the structural evolution of colloidal crystals upon heating. J. Appl. Cryst. **46**, 903 (2013).

2. J.-M. Meijer, A. G. Shabalin, R. Dronyak, O. M. Yefanov, A. Singer, R. P. Kurta, U. Lorenz, O. Gorobtsov, D. Dzhigaev, J. Gulden, D. V. Byelov, A. V. Zozulya, M. Sprung, I. A. Vartanyants and A. V. Petukhov. Double hexagonal close-packed structure revealed in a single colloidal crystal grain by Bragg rod analysis. J. Appl. Cryst. **47**, 1199 (2014).

3. E. A. Sulyanova, A. G. Shabalin, A. V. Zozulya, J.-M. Meijer, D. Dzhigaev, O. Gorobtsov, R. P. Kurta, U. Lorentz, A. Singer, O. M. Yefanov, I. Zaluzhnii, I. Besedin, M. Sprung, A. V. Petukhov, and I. A. Vartanyants. Structural evolution of colloidal crystal films in the vicinity of the melting transition revealed by Bragg peak analysis. Langmuir, **31**, 5274 (2015).

4. A. G. Shabalin, O. M. Yefanov, V. Nosik, I. A. Vartanyants. Dynamical effects in coherent X-ray scattering on a finite crystal.(*Close to submission*)

5. A. G. Shabalin, J.-M. Meijer, R. Dronyak, O. M. Yefanov, A. Singer, R. Kurta, U. Lorenz, O. Gorobtsov, D. Dzhigaev, S. Kalbfleisch, J. Gulden, A. Zozulya, M. Sprung, A. V. Petukhov, and I. A. Vartanyants. 3D Coherent X-ray Diffraction Imaging of a single colloidal crystal grain. (*Close to submission*)

6. M. Civita, A. Diaz, O. Gorobtsov, A. G. Shabalin, I. A. Vartanyants and I. K. Robinson. Direct determination of the phase of a Structure Factor by Ptychographic Imaging. (*In preparation*)

7. D. Dzhigaev, A. G. Shabalin, O. M. Yefanov, R. Dronyak, F. Seiboth, T. Stankevič, R. P. Kurta, A. Singer, G. Falkenberg, C. G. Schroer, R. Feidenhans, and I. A. Vartanyants. Imaging of a single InP nanowire using Bragg Ptychography and CXDI. (*In preparation*)

Publications not directly related to the thesis

1. R. P. Kurta, B. I. Ostrovskii, A. Singer, O. Y. Gorobtsov, A. G. Shabalin, D. Dzhigaev, O. M. Yefanov, A. V. Zozulya, M. Sprung, and I. A. Vartanyants. X-ray cross-correlation analysis of liquid crystal membranes in the vicinity of the hexatic-smectic phase transition. Phys. Rev. E **88**, 044501 (2013).

2. A. Singer, U. Lorenz, F. Sorgenfrei, N. Gerasimova, J. Gulden, O. M. Yefanov, R. P. Kurta, A. Shabalin, R. Dronyak, R. Treusch, V. Kocharyan, E. Weckert, W. Wurth, and I. A. Vartanyants. Hanbury BrownTwiss Interferometry at a Free-Electron Laser. Phys. Rev. Lett. **111**, 034802 (2013).

3. A. Singer, U. Lorenz, A. Marras, A. Klyuev, J. Becker, K. Schlage, P. Skopintsev, O. Gorobtsov, A. G. Shabalin, H.-C. Wille, H. Franz, H. Graafsma and I. A. Vartanyants. Intensity Interferometry of Single X-ray Pulses from a Synchrotron Storage Ring. Phys. Rev. Lett. **113**, 064801 (2014).

4. A. V. Zozulya, A. G. Shabalin, H. Schulte-Schrepping, J. Heuer, M. Spiwek, I. Sergeev, I. Besedin, I. A. Vartanyants, and M. Sprung. Wavefront preserving channel-cut optics for coherent x-ray scattering experiments at the P10 beamline at PETRAIII. Journal of Physics: Conference Series **499**, 012003 (2014).

5. D. Dzhigaev, U. Lorenz, R. P. Kurta, F. Seiboth, T. Stankevič, S. Mickevicius, A. Singer, A. G. Shabalin, O. M. Yefanov, M. N. Strikhanov, G. Falkenberg, C. G. Schroer, R. Feidenhans'l, and I. A. Vartanyants. Ptychographical imaging of the phase vortices in the x-ray beam formed by nanofocusing lenses. Journal of Physics: Conference Series **499**, 012020 (2014).

6. I. A. Zaluzhnyy, R. P. Kurta, E. A. Sulyanova, O. Y. Gorobtsov, A. G. Shabalin, A. V. Zozulya, A. P. Menushenkov, M. Sprung, B. I. Ostrovskii and I. A. Vartanyants. Spatially resolved x-ray studies of liquid crystals with strongly developed bond-orientational order., Phys. Rev. E. **91**, 042506 (2015).

7. P. Skopintsev, A. Singer, J. Bach, L. Müller, B. Beyersdorff, S. Schleitzer, O. Gorobtsov, A. G. Shabalin, R. P. Kurta, D. Dzhigaev, O. M. Yefanov, L. Glaser, A. Sakdinawat, G. Grübel, R. Frömter, H. P. Oepen, J. Viefhaus, and I. A. Vartanyants. Characterization of spatial coherence of synchrotron radiation with non-redundant arrays of apertures. J. Synchrotron Rad. **21**, 722 (2014).

8. M. Rose, P. Skopintsev, D. Dzhigaev, O. Gorobtsov, T. Senkbeil, A. von Gundlach, T. Gorniak, A. G. Shabalin, J. Viefhaus, A. Rosenhahn and I. A. Vartanyants. Water Window Ptychographic Imaging with Characterized Coherent X-rays. J. Synchrotron Rad. **22**, 503 (2015).

9. T. Stankevič, D. Dzhigaev, Z. Bi, M. Rose, A. G. Shabalin, J. Reinhardt, A. Mikkelsen, L. Samuelson, G. Falkenberg, I. A. Vartanyants, and J. Viefhaus. Strain mapping in individual InGaN/GaN nanowire using nano-focused X-ray beam. Appl. Phys. Lett. **107**, 103101 (2015).

Bibliography

[1] Adapted from IPCS website (www.inchem.org).

[2] W. C. Röntgen. Über eine neue Art von Strahlen. *Annalen der Physik*, 300(1):1–11, 1898.

[3] W. Friedrich, M. Knipping, and M. Laue. Interferenzerscheinungen bei Röntgenstrahlen. *Annalen der Physik*, 41, 1913.

[4] W. H. Bragg and W. L. Bragg. The reflection of X-rays by crystals. *Proc. Roy. Soc.*, A88, 1913.

[5] G. N. Kulipanov. Ginzburg's invention of undulators and their role in modern synchrotron radiation sources and free electron lasers. *UFN*, 177(4):384–393, 2007.

[6] H. Motz. Applications of the radiation from fast electron beams. *Journal of Applied Physics*, 22(5):527–535, 1951.

[7] D. Attwood. *Soft X-rays and extreme ultraviolet radiation: principles and applications*. Cambridge university press, 1999.

[8] J. M. Madey. Stimulated emission of bremsstrahlung in a periodic magnetic field. *Journal of Applied Physics*, 42(5):1906–1913, 1971.

[9] A. M. Kondratenko and E. L. Saldin. Generation of coherent radiation by a relativistic-electron beam in an undulator. In *Soviet Physics Doklady*, volume 24, page 986, 1979.

[10] R. Bonifacio, C. Pellegrini, and L. M. Narducci. Collective instabilities and high-gain regime in a free electron laser. *Optics Communications*, 50(6):373–378, 1984.

[11] P. Schmüser, M. Dohlus, and J. Rossbach. *Ultraviolet and soft X-ray free-electron lasers: introduction to physical principles, experimental results, technological challenges*, volume 229. Springer, 2008.

[12] A. Thompson, D. Attwood, E. Gullikson, M. Howells, K. J. Kim, J. Kirz, J. Kortright, I. Lindau, P. Pianetta, A. Robinson, J. Scofield, J. Underwood, D. Vaughan, and G. Williams. X-ray Data Booklet (Lawrence Berkeley National Laboratory, Berkeley, CA).

[13] J. Als-Nielsen and D. McMorrow. *Elements of Modern X-ray Physics: Second Edition*. John Wiley & Sons, Inc., Hoboken, NJ, USA, 2011.

[14] Adapted from the European XFEL website (www.XFEL.eu).

[15] R. A. Quinn and C. C. Sigl. *Radiography in modern industry*. Eastman Kodak, 1980.

[16] G. Michael. X-ray computed tomography. *Physics Education*, 36(6):442, 2001.

[17] A. H. Compton. A quantum theory of the scattering of X-rays by light elements. *Physical Review*, 21(5):483, 1923.

[18] J. D. Jackson and J. D. Jackson. *Classical electrodynamics*, volume 3. Wiley New York etc., 1962.

[19] B. E. Warren. *X-ray Diffraction*. Courier Dover Publications, 1969.

[20] D. C. Koningsberger and R. Prins. X-ray absorption: principles, applications, techniques of EXAFS, SEXAFS, and XANES. 1988.

[21] E. Prince, A. Wilson, T. Hahn, and U. Shmueli. *International tables for crystallography*. International Union of Crystallography, 1999.

[22] D. M. Paganin. *Coherent X-ray optics*. Oxford University Press, 2006.

[23] M. Blume. Magnetic scattering of X-rays. *Journal of Applied Physics*, 57(8):3615–3618, 1985.

[24] D. A. Long and D. A. Long. *Raman spectroscopy*, volume 206. McGraw-Hill New York, 1977.

[25] M. Born and E. Wolf. *Principles of optics: electromagnetic theory of propagation, interference and diffraction of light*. CUP Archive, 1999.

[26] M. Eckert. Max von Laue and the discovery of X-ray diffraction in 1912. *Annalen der Physik*, 524(5):A83–A85, 2012.

[27] A. Authier. *Dynamical Theory of X-ray Diffraction*. IUCr Crystallographic Symposia Series. Oxford University Press, 2001.

[28] G. Gilli. Fundamentals of Crystallography, edited by C. Giacovazzo, 2002.

[29] I. A. Vartanyants and O. M. Yefanov. Coherent x-ray diffraction imaging of nanostructures. In the book *X-ray Diffraction. Modern Experimental Techniques*. Edited by O. H. Seeck and B. M. Murphy. pages 341–384. Pan Stanford Publishing, Singapore, 2015.

[30] A. Papoulis. *Signal analysis*, volume 191. McGraw-Hill, 1977.

[31] P. Debye. Interference of X-rays and thermal motion. *Annalen der Physik*, 43:49–95, 1914.

[32] I. A. Vartanyants and I. K. Robinson. Partial coherence effects on the imaging of small crystals using coherent X-ray diffraction. *Journal of Physics: Condensed Matter*, 13(47):10593–10611, 2001.

[33] M. Pfeifer, G. Williams, I. A. Vartanyants, R. Harder, and I. K. Robinson. Three-dimensional mapping of a deformation field inside a nanocrystal. *Nature*, 442(7098):63–66, 2006.

[34] I. A. Robinson and R. Harder. Coherent X-ray diffraction imaging of strain at the nanoscale. *Nature Materials*, 8(4):291–8, 2009.

[35] G. K. Williamson and W. H. Hall. X-ray line broadening from filed aluminium and wolfram. *Acta Metallurgica*, 1(1):22–31, 1953.

[36] H. P. Klug and L. E. Alexander. *X-ray diffraction procedures*, volume 2. Wiley New York, 1954.

[37] T. L. Blundell and L. N. Johnson. Protein crystallography. *Academic Press*, 1976.

[38] P. P. Ewald. The crystal-optics of X-rays (I). *Ann. Phys.(Leipzig)*, 54:519–556, 1917.

[39] M. von Laue. Ergebnisse der exakten naturwissenschaften. *Naturwissenschaften*, 10:207–284, 1931.

[40] Max von Laue. *Röntgenstrahlinterferenzen*. Akad. Verl.-Ges., 1960.

[41] B. W. Batterman and H. Cole. Dynamical Diffraction of X-rays by Perfect Crystals. *Reviews of Modern Physics*, 36(3):681–717, 1964.

[42] Z. G. Pinsker. *Dynamical Scattering of X-rays in Crystals*, volume 3. Springer-Verlag Berlin, 1978.

[43] W. H. Zachariasen. Theory of X-ray Diffraction by Crystals. *New York*, 1945.

[44] B. W. Batterman. Dynamical theory of X-ray diffraction. *Acta Crystallographica Section A*, 58(4):412, 2002.

[45] S. Takagi. A dynamical theory of diffraction for a distorted crystal. *Journal of the Physical Society of Japan*, 26(5):1239–1253, 1969.

[46] D. Taupin. Prévision de quelques images de dislocations par transmission des rayons X (cas de Laue symétrique). *Acta Crystallographica*, 23(1):25–35, 1967.

[47] W. H. Zachariasen. A general theory of X-ray diffraction in crystals. *Acta Crystallographica*, 23(4):558–564, 1967.

[48] A. M. Afanas'ev and V. G. Kohn. Dynamical theory of X-ray diffraction in crystals with defects. *Acta Crystallographica Section A*, 27(5):421–430, 1971.

[49] G. Borrmann. Absorption of Röntgen rays in the case of interference. *Phys. Z.*, 127:297–323, 1950.

[50] L. Mandel and E. Wolf. *Optical coherence and quantum optics*. Cambridge university press, 1995.

[51] J. Goodman. *Introduction to Fourier Optics*, volume 2. McGraw-hill New York, 1968.

[52] W. Chao, B. D. Harteneck, J. A. Liddle, E. H. Anderson, and D. Attwood. Soft X-ray microscopy at a spatial resolution better than 15 nm. *Nature*, 435(7046):1210–1213, 2005.

[53] W. Chao, J. Kim, S. Rekawa, P. Fischer, and E. H. Anderson. Demonstration of 12 nm resolution Fresnel zone plate lens based soft X-ray microscopy. *Optics Express*, 17(20):17669–17677, 2009.

[54] P. Kirkpatrick and A. V. Baez. Formation of optical images by X-rays. *JOSA*, 38(9):766–773, 1948.

[55] A. Snigirev, V. Kohn, I. Snigireva, and B. Lengeler. A compound refractive lens for focusing high-energy X-rays. *Nature*, 384(6604):49–51, 1996.

[56] E. Fabrizio, F. Romanato, M. Gentili, S. Cabrini, B. Kaulich, J. Susini, and R. Barrett. High-efficiency multilevel zone plates for keV X-rays. *Nature*, 401(6756):895–898, 1999.

[57] K. A. Nugent. Coherent methods in the X-ray sciences. *Advances in Physics*, 59(1):1–99, 2010.

[58] H. N. Chapman and K. A. Nugent. Coherent lensless X-ray imaging. *Nature Photonics*, 4(12):833–839, 2010.

[59] J. D. Jackson and R. F. Fox. Classical electrodynamics. *American Journal of Physics*, 67(9):841–842, 1999.

[60] A. Schropp, P. Boye, J. M. Feldkamp, R. Hoppe, J. Patommel, D. Samberg, S. Stephan, K. Giewekemeyer, R. N. Wilke, and T. Salditt. Hard X-ray nanobeam characterization by coherent diffraction microscopy. *Applied Physics Letters*, 96(9):91102, 2010.

[61] H. Nyquist. Certain topics in telegraph transmission theory. *American Institute of Electrical Engineers, Transactions of the*, 47(2):617–644, 1928.

[62] C. E. Shannon. Communication in the presence of noise. *Proceedings of the IRE*, 37(1):10–21, 1949.

[63] C. Caleman, M. Bergh, H. A. Scott, J. Spence, H. N. Chapman, and N. Tîmneanu. *Journal of Modern Optics*, 58(16):1486–1497, 2011.

[64] A. Ulvestad, A. Singer, H.-M. Cho, J. N. Clark, R. Harder, J. Maser, Y. S. Meng, and O. G. Shpyrko. Single Particle Nanomechanics in Operando Batteries via Lensless Strain Mapping. *Nano Letters*, 14(9):5123–5127, 2014.

[65] D. Sayre. The squaring method: a new method for phase determination. *Acta Crystallographica*, 5(1):60–65, 1952.

[66] J. Gulden, O. M. Yefanov, E. Weckert, and I. A. Vartanyants. Imaging of Nanocrystals with Atomic Resolution Using High-Energy Coherent X-rays. In *THE 10TH INTERNATIONAL CONFERENCE ON X-RAY MICROSCOPY*, volume 1365, pages 42–45. AIP Publishing, 2011.

[67] J. M. Zuo, I. A. Vartanyants, M. Gao, R. Zhang, and L. A. Nagahara. Atomic resolution imaging of a carbon nanotube from diffraction intensities. *Science*, 300(5624):1419–1421, 2003.

[68] R. Dronyak, K. S. Liang, J.-S. Tsai, Y. P. Stetsko, T.-K. Lee, and F.-R. Chen. Electron coherent diffraction tomography of a nanocrystal. *Applied Physics Letters*, 96(22):221907, 2010.

[69] C.-C. Chen, C. Zhu, E. R. White, C.-Y. Chiu, M. C. Scott, B. C. Regan, L. D. Marks, Y. Huang, and J. Miao. Three-dimensional imaging of dislocations in a nanoparticle at atomic resolution. *Nature*, 496(7443):74–7, 2013.

[70] J. Gulden, O. M. Yefanov, A. P. Mancuso, V. V. Abramova, J. Hilhorst, D. Byelov, I. Snigireva, A. Snigirev, A. V. Petukhov, and I. A. Vartanyants. Coherent X-ray imaging of defects in colloidal crystals. *Physical Review B*, 81(22):224105, 2010.

[71] J. Gulden, O. M. Yefanov, A. P. Mancuso, R. Dronyak, A. Singer, V. Bernátová, A. Burkhardt, O. Polozhentsev, A. Soldatov, M. Sprung, and I. A. Vartanyants. Three-dimensional structure of a single colloidal crystal grain studied by coherent X-ray diffraction. *Optics Express*, 20(4):4039–49, 2012.

[72] R. P. Millane. Phase retrieval in crystallography and optics. *JOSA A*, 7(3):394–411, 1990.

[73] R. W. Gerchberg and W. O. Saxton. A practical algorithm for the determination of the phase from image and diffraction plane pictures. *Optik (Jena)*, 35:237, 1972.

[74] J. R. Fienup. Phase retrieval algorithms: a comparison. *Applied optics*, 21(15):2758–69, 1982.

[75] S. Marchesini. Invited article: A unified evaluation of iterative projection algorithms for phase retrieval. *Review of Scientific Instruments*, 78(1):11301, 2007.

[76] R. P. Millane and W. J. Stroud. Reconstructing symmetric images from their undersampled Fourier intensities. *JOSA A*, 14(3):568–579, 1997.

[77] C.-C. Chen, J. Miao, C. Wang, and T. Lee. Application of optimization technique to noncrystalline X-ray diffraction microscopy: Guided hybrid input-output method. *Physical Review B*, 76(6):064113, 2007.

[78] S. Marchesini, H. He, H. N. Chapman, S. P. Hau-Riege, A. Noy, M. R. Howells, U. Weierstall, and J. C. H. Spence. X-ray image reconstruction from a diffraction pattern alone. *Physical Review B*, 68(14):140101, 2003.

[79] P. Thibault, V. Elser, C. Jacobsen, D. Shapiro, and D. Sayre. Reconstruction of a yeast cell from X-ray diffraction data. *Acta Crystallographica Section A: Foundations of Crystallography*, 62(4):248–261, 2006.

[80] N. E. Hurt. *Phase retrieval and zero crossings: mathematical methods in image reconstruction*, volume 52. Springer Science & Business Media, 2001.

[81] G. R. Morrison and M. T. Browne. Dark-field imaging with the scanning transmission X-ray microscope. *Review of Scientific Instruments*, 63(1):611–614, 1992.

[82] A. V. Martin, N. D. Loh, C. Y. Hampton, R. G. Sierra, F. Wang, A. Aquila, S. Bajt, M. Barthelmess, C. Bostedt, and J. D. Bozek. Femtosecond dark-field imaging with an X-ray free electron laser. *Optics Express*, 20(12):13501–13512, 2012.

[83] R. H. T. Bates. Fourier phase problems are uniquely solvable in mute than one dimension. I: Underlying theory. *Optik(Stuttgart)*, 61:247–262, 1982.

[84] W. Hoppe. Beugung im inhomogenen Primärstrahlwellenfeld. I. Prinzip einer Phasenmessung von Elektronenbeugungsinterferenzen. *Acta Crystallographica Section A*, 25(4):495–501, 1969.

[85] J. Rodenburg, A. Hurst, A. Cullis, B. Dobson, F. Pfeiffer, O. Bunk, C. David, K. Jefimovs, and I. Johnson. Hard-X-Ray Lensless Imaging of Extended Objects. *Physical Review Letters*, 98(3):034801, 2007.

[86] P. Thibault, M. Dierolf, A. Menzel, O. Bunk, C. David, and F. Pfeiffer. High-resolution scanning X-ray diffraction microscopy. *Science*, 321(5887):379–382, 2008.

[87] M. Dierolf, O. Bunk, S. Kynde, P. Thibault, I. Johnson, A. Menzel, K. Jefimovs, C. David, O. Marti, and F. Pfeiffer. Ptychography & lensless X-ray imaging. *Europhysics News*, 39(1):22–24, 2008.

[88] M. Dierolf, A. Menzel, P. Thibault, P. Schneider, C. Kewish, R. Wepf, O. Bunk, and F. Pfeiffer. Ptychographic X-ray computed tomography at the nanoscale. *Nature*, 467(7314):436–439, 2010.

[89] H. M. Quiney, K. A. Nugent, and A. G. Peele. Iterative image reconstruction algorithms using wave-front intensity and phase variation. *Optics Letters*, 30(13):1638–1640, 2005.

[90] G. J. Williams, H. M. Quiney, B. B. Dhal, C. Q. Tran, K. A. Nugent, A. G. Peele, D. Paterson, and M. D. de Jonge. Fresnel Coherent Diffractive Imaging. *Physical Review Letters*, 97(2):025506, 2006.

[91] G. J. Williams, H. M. Quiney, A. G. Peele, and K. A. Nugent. Coherent diffractive imaging and partial coherence. *Physical Review B*, 75(10):104102, 2007.

[92] L. W. Whitehead, G. J. Williams, H. M. Quiney, D. J. Vine, R. A. Dilanian, S. Flewett, K. A. Nugent, A. G. Peele, E. Balaur, and I. McNulty. Diffractive imaging using partially coherent X-rays. *Physical Review Letters*, 103(24):243902, 2009.

[93] S. Eisebitt, J. Lüning, W. F. Schlotter, M. Lörgen, O. Hellwig, W. Eberhardt, and J. Stöhr. Lensless imaging of magnetic nanostructures by X-ray spectro-holography. *Nature*, 432(7019):885–888, 2004.

[94] V. Chamard, J. Stangl, G. Carbone, A. Diaz, G. Chen, C. Alfonso, C. Mocuta, and T. H. Metzger. Three-dimensional X-ray Fourier transform holography: The Bragg case. *Physical Review Letters*, 104(16):165501, 2010.

[95] I. McNulty, J. Kirz, C. Jacobsen, E. H. Anderson, M. R. Howells, and D. P. Kern. High-resolution imaging by Fourier transform X-ray holography. *Science*, 256(5059):1009–1012, 1992.

[96] W. Leitenberger and A. Snigirev. Microscopic imaging with high energy X-rays by Fourier transform holography. *Journal of Applied Physics*, 90(2):538–544, 2001.

[97] I. K. Robinson, I. A. Vartanyants, G. J. Williams, M. A. Pfeifer, and J. A. Pitney. Reconstruction of the shapes of gold nanocrystals using coherent x-ray diffraction. *Physical Review Letters*, 87(19):195505, 2001.

[98] G. J. Williams, M. A. Pfeifer, I. A. Vartanyants, and I. K. Robinson. Three-dimensional imaging of microstructure in Au nanocrystals. *Physical Review Letters*, 90(17):175501, 2003.

[99] J. Gronkowski. Propagation of X-rays in distorted crystals under dynamical diffraction. *Physics Reports*, 206(1):1–41, 1991.

[100] Y. Epelboin and P. Riglet. Boundary Conditions in the Numerical Integration of Takagi-Taupin Equations. Application to the Laue and Bragg Cases. *Physica Status Solidi (a)*, 54(2):547–556, 1979.

[101] V. Mocella, W.-K. Lee, G. Tajiri, D. Mills, C. Ferrero, and Y. Epelboin. A new approach to the solution of the Takagi-Taupin equations for X-ray optics: application to a thermally deformed crystal monochromator. *Journal of Applied Crystallography*, 36(1):129–136, 2003.

[102] S. I. Kolosov and V. I. Punegov. Numerical integration methods for the Takagi-Taupin equations for crystals of rectangular cross section. *Crystallography Reports*, 50(3):357–362, 2005.

[103] R. Harder, M. Pfeifer, G. Williams, I. A. Vartaniants, and I. K. Robinson. Orientation variation of surface strain. *Physical Review B*, 76(11):115425, 2007.

[104] M. Civita, A. Diaz, O. Gorobtsov, A. Shabalin, I. A. Vartanyants, and I. K. Robinson. Direct determination of the phase of a Structure Factor by Ptychographic Imaging. *(in preparation)*, 2015.

[105] O. Gorobtsov, A. Shabalin, and I. A. Vartanyants. Dynamical phase correction for nanocrystals and near-kinematical approximation. *(in preparation)*, 2015.

[106] R Paolesse, F Mandoj, A Marini, and C Di Natale. Encyclopedia of nanoscience and nanotechnology, vol. x. *American Scientific Publisher*, 2003.

[107] N. D. Denkov, O. D. Velev, P. A. Kralchevsky, I. B. Ivanov, H. Yoshimura, and K. Nagayama. Two-dimensional crystallization. *Nature*, 361:26, 1993.

[108] A. Blanco, E. Chomski, S. Grabtchak, M. Ibisate, S. John, S. Leonard, C. Lopez, F. Meseguer, H. Miguez, J. Mondia, G. Ozin, O. Toader, and van Driel HM. Large-scale synthesis of a silicon photonic crystal with a complete three-dimensional bandgap near 1.5 micrometres. *Nature*, 405(6785):437–40, 2000.

[109] Yu. A. Vlasov, X.-Z. Bo, J. C. Sturm, and D. J. Norris. On-chip natural assembly of silicon photonic bandgap crystals. *Nature*, 414(6861):289–293, 2001.

[110] J. F. Galisteo-López, M. Ibisate, R. Sapienza, L. Froufe-Pérez, A. Blanco, and C. López. Self-assembled photonic structures. *Advanced Materials*, 23(1):30–69, 2011.

[111] A. Scherer, T. Doll, E. Yablonovitch, H. Everitt, and J. A. Higgins. Guest Editorial: Electromagnetic crystal structures, design, synthesis, and applications. *Journal of Lightwave Technology*, 17(11):1928–1930, 1999.

[112] S. John. Strong localization of photons in certain disordered dielectric superlattices. *Physical Review Letters*, 58(23):2486, 1987.

[113] E. Yablonovitch. Inhibited spontaneous emission in solid-state physics and electronics. *Physical Review Letters*, 58(20):2059, 1987.

[114] S. G. Johnson and J. D. Joannopoulos. *Photonic crystals: the road from theory to practice*. Springer Science & Business Media, 2002.

[115] O. Painter, R. Lee, A. Scherer, A. Yariv, J. O'Brien, P. Dapkus, and I. Kim. Two-dimensional photonic band-gap defect mode laser. *Science (New York, N.Y.)*, 284(5421):1819–21, 1999.

[116] M. Soljačić, C. Luo, J. D. Joannopoulos, and S. Fan. Nonlinear photonic crystal microdevices for optical integration. *Optics Letters*, 28(8):637–639, 2003.

[117] J. Hilhorst, V. Abramova, A. Sinitskii, N. Sapoletova, K. Napolskii, A. Eliseev, D. V. Byelov, N. Grigoryeva, A. Vasilieva, W. G. Bouwman, K. Kvashnina, A. Snigirev, S. V. Grigoriev, and A. V. Petukhov. Double stacking faults in convectively assembled crystals of colloidal spheres. *Langmuir*, 25(17):10408–12, 2009.

[118] J.-M. Meijer, F. Hagemans, L. Rossi, D. V. Byelov, S. I. R. Castillo, A. Snigirev, I. Snigireva, A. P. Philipse, and A. V. Petukhov. Self-assembly of colloidal cubes via vertical deposition. *Langmuir*, 28(20):7631–7638, 2012.

[119] W. Hess and R. Klein. Generalized hydrodynamics of systems of Brownian particles. *Advances in Physics*, 32(2):173–283, 1983.

[120] P. C. Hiemenz. The role of van der Waals forces in surface and colloid chemistry. *Journal of Chemical Education*, 49(3):164, 1972.

[121] T. Tadros. General principles of colloid stability and the role of surface forces. *Colloid Stability: The Role of Surface Forces - Part I*, 1, 2007.

[122] G. Fritz, V. Schädler, N. Willenbacher, and N. J. Wagner. Electrosteric stabilization of colloidal dispersions. *Langmuir*, 18(16):6381–6390, 2002.

[123] P. Jiang, J. Bertone, K. Hwang, and V. Colvin. Single-crystal colloidal multilayers of controlled thickness. *Chemistry of Materials*, 11(8):2132–2140, 1999.

[124] D. J. Norris, E. G. Arlinghaus, L. Meng, R. Heiny, and L. E. Scriven. Opaline Photonic Crystals: How Does Self-Assembly Work? *Advanced Materials*, 16(16):1393–1399, 2004.

[125] J. B. Jones, J. V. Sanders, and E. R. Segnit. Structure of opal. *Nature Publishing Group*, 1964.

[126] P. J. Darragh, A. J. Gaskin, and J. V. Sanders. Opals. *Scientific American*, 234:84–95, 1976.

[127] P. Pieranski. Colloidal crystals. *Contemporary Physics*, 24(1):25–73, 1983.

[128] J. Zhang, Z. Sun, and B. Yang. Self-assembly of photonic crystals from polymer colloids. *Current Opinion in Colloid & Interface Science*, 14(2):103–114, 2009.

[129] Z. Zhou and X. S. Zhao. Opal and inverse opal fabricated with a flow-controlled vertical deposition method. *Langmuir*, 21(10):4717–4723, 2005.

[130] S. H. Im, M. H. Kim, and O. Park. Thickness control of colloidal crystals with a substrate dipped at a tilted angle into a colloidal suspension. *Chemistry of Materials*, 15(9):1797–1802, 2003.

[131] L. Meng, H. Wei, A. Nagel, B. J. Wiley, L. E. Scriven, and D. J. Norris. The role of thickness transitions in convective assembly. *Nano Letters*, 6(10):2249–2253, 2006.

[132] D. Brewer, J. Allen, M. Miller, J. de Santos, S. Kumar, D. J. Norris, M. Tsapatsis, and L. E. Scriven. Mechanistic principles of colloidal crystal growth by evaporation-induced convective steering. *Langmuir*, 24(23):13683–13693, 2008.

[133] H. Cao, D. Lan, Y. Wang, A. A. Volinsky, L. Duan, and H. Jiang. Fracture of colloidal single-crystal films fabricated by controlled vertical drying deposition. *Physical Review E*, 82(3):31602, 2010.

[134] P. Krishna and D. Pandey. *Close-packed structures*. International Union of Crystallography by University College Cardi Press. Cardi, Wales, 1981.

[135] L. V. Woodcock. Entropy difference between the face-centred cubic and hexagonal close-packed crystal structures. *Nature Publishing Group*, 1997.

[136] P. G. Bolhuis, D. Frenkel, S.-C. Mau, and D. A. Huse. Entropy difference between crystal phases. *Nature*, 388(6639):235–236, 1997.

[137] A. V. Petukhov, I. Dolbnya, D. Aarts, G. Vroege, and H. Lekkerkerker. Bragg Rods and Multiple X-Ray Scattering in Random-Stacking Colloidal Crystals. *Physical Review Letters*, 90(2):028304, 2003.

[138] I. P. Dolbnya, A. V. Petukhov, D. Aarts, G. J. Vroege, and H. Lekkerkerker. Coexistence of rhcp and fcc phases in hard-sphere colloidal crystals. *Europhysics Letters*, 72(6):962, 2005.

[139] A. D. Dinsmore, E. R. Weeks, V. Prasad, A. C. Levitt, and D. A. Weitz. Three-dimensional confocal microscopy of colloids. *Applied Optics*, 40(24):4152–4159, 2001.

[140] P. Schall, I. Cohen, D. A. Weitz, and F. Spaepen. Visualization of dislocation dynamics in colloidal crystals. *Science*, 305(5692):1944–1948, 2004.

[141] P. Schall. Laser diffraction microscopy. *Reports on Progress in Physics*, 72(7):76601, 2009.

[142] Y.-H. Ye, T. S. Mayer, I.-C. Khoo, I. B. Divliansky, N. Abrams, and T. E. Mallouk. Self-assembly of three-dimensional photonic-crystals with air-core line defects. *J. Mater. Chem.*, 12(12):3637–3639, 2002.

[143] A. Bosak, I. Snigireva, K. S. Napolskii, and A. Snigirev. High-resolution transmission X-ray microscopy: A new tool for mesoscopic materials. *Advanced Materials*, 22(30):3256–3259, 2010.

[144] J. Hilhorst, M. M. van Schooneveld, J. Wang, E. de Smit, T. Tyliszczak, J. Raabe, A. P. Hitchcock, M. Obst, F. de Groot, and A. V. Petukhov. Three-dimensional structure and defects in colloidal photonic crystals revealed by tomographic scanning transmission X-ray microscopy. *Langmuir*, 28(7):3614–20, 2012.

[145] D. V. Byelov, J.-M. Meijer, I. Snigireva, A. Snigirev, L. Rossi, E. van den Pol, A. Kuijk, A. Philipse, A. Imhof, A. van Blaaderen, G. J. Vroege, and A. V. Petukhov. In situ hard X-ray microscopy of self-assembly in colloidal suspensions. *RSC Adv.*, 3(36):15670, 2013.

[146] E. B. Sirota, H. D. Ou-Yang, S. K. Sinha, P. M. Chaikin, J. D. Axe, and Y. Fujii. Complete phase diagram of a charged colloidal system: A synchrotron X-ray scattering study. *Physical Review Letters*, 62(13):1524, 1989.

[147] L. B. Chen, M. K. Chow, B. J. Ackerson, and C. F. Zukoski. Rheological and microstructural transitions in colloidal crystals. *Langmuir*, 10(8):2817–2829, 1994.

[148] M. M. van Schooneveld, J. Hilhorst, A. V. Petukhov, T. Tyliszczak, J. Wang, B. M. Weckhuysen, F. de Groot, and E. de Smit. Scanning Transmission X-Ray Microscopy as a Novel Tool to Probe Colloidal and Photonic Crystals. *Small*, 7(6):804–811, 2011.

[149] H. Versmold, S. Musa, Ch. Dux, and P. Lindner. On the Structure of Shear-Ordered Colloidal Dispersions: Bragg-Rod Intensity Distribution. *Langmuir*, 15(15):5065–5067, 1999.

[150] A. V. Petukhov, D. Aarts, I. Dolbnya, E. de Hoog, K. Kassapidou, G. Vroege, W. Bras, and H. Lekkerkerker. High-Resolution Small-Angle X-Ray Diffraction Study of Long-Range Order in Hard-Sphere Colloidal Crystals. *Physical Review Letters*, 88(20):208301, 2002.

[151] A. V. Petukhov, J. Thijssen, A. Imhof, A. van Blaaderen, I. .P Dolbnya, A. Snigirev, A. Moussaid, and I. Snigireva. Microradian X-ray diffraction in colloidal photonic crystals. *Journal of Applied Crystallography*, 39(2):137–144, 2006.

[152] J. Thijssen, A. V. Petukhov, D. C. t Hart, A. Imhof, C. H. M. van der Werf, R. E. I. Schropp, and A. van Blaaderen. Characterization of Photonic Colloidal Single Crystals by Microradian X-ray Diffraction. *Advanced Materials*, 18(13):1662–1666, 2006.

[153] A. Sinitskii, V. Abramova, N. Grigorieva, S. Grigoriev, A. Snigirev, D. V. Byelov, and A. V. Petukhov. Revealing stacking sequences in inverse opals by microradian X-ray diffraction. *EPL (Europhysics Letters)*, 89(1):14002, 2010.

[154] D. V. Byelov, J. Hilhorst, I. Snigireva, A. Snigirev, G. Vaughan, G. Portale, and A. V. Petukhov. Diffuse scattering in random-stacking hexagonal close-packed crystals of colloidal hard spheres. *Phase Transitions*, 83(2):107–114, 2010.

[155] M. Vos, W.and Megens, C. van Kats, and P. Bösecke. X-ray Diffraction of Photonic Colloidal Single Crystals. *Langmuir*, 13(23):6004–6008, 1997.

[156] J. S. Pedersen. *Modelling of small-angle scattering data from colloids and polymer systems*. North Holland, Elsevier: Amsterdam, 2002.

[157] A. V. Zozulya, S. Bondarenko, A. Schavkan, F. Westermeier, G. Grübel, and M. Sprung. Microfocusing transfocator for 1d and 2d compound refractive lenses. *Optics Express*, 20(17):18967–18976, 2012.

[158] A. Schavkan, F. Westermeier, A. Zozulya, S. Bondarenko, G. Grübel, C. Schroer, and M. Sprung. Using the MAXIPIX detector for coherent X-ray scattering applications. *Journal of Physics: Conference Series*, 425(20):202004, 2013.

[159] S. L. Barnes. A technique for maximizing details in numerical weather map analysis. *Journal of Applied Meteorology*, 3(4):396–409, 1964.

[160] J.-M. Meijer, A. Shabalin, R. Dronyak, O. M. Yefanov, A. Singer, R. P. Kurta, U. Lorenz, O. Gorobstov, D. Dzhigaev, J. Gulden, D. V. Byelov, A. V. Zozulya, M. Sprung, I. A. Vartanyants, and A. V. Petukhov. Double hexagonal close-packed structure revealed in a single colloidal crystal grain by Bragg rod analysis. *Journal of Applied Crystallography*, 47(4):1199–1204, 2014.

[161] A. Guinier. *X-ray diffraction in crystals, imperfect crystals, and amorphous bodies*. Courier Corporation, 1994.

[162] J.-M. Meijer, V. de Villeneuve, and A. V. Petukhov. In-plane stacking disorder in polydisperse hard sphere crystals. *Langmuir*, 23(7):3554–3560, 2007.

[163] N. Denkov, O. Velev, P. Kralchevski, I. Ivanov, H. Yoshimura, and K. Nagayama. Mechanism of formation of two-dimensional crystals from latex particles on substrates. *Langmuir*, 8(12):3183–3190, 1992.

[164] A. Kosiorek, W. Kandulski, H. Glaczynska, and M. Giersig. Fabrication of nanoscale rings, dots, and rods by combining shadow nanosphere lithography and annealed polystyrene nanosphere masks. *Small*, 1(4):439–444, 2005.

[165] S. Hu, J. Rieger, S. V. Roth, R. Gehrke, R. J. Leyrer, and Y. Men. GIUSAXS and AFM Studies on Surface Reconstruction of Latex Thin Films during Thermal Treatment. *Langmuir*, 25(7):4230–4234, 2008.

[166] S. Hu, J. Rieger, Z. Yi, J. Zhang, X. Chen, S. V. Roth, R. Gehrke, and Y. Men. Structural evolution of a colloidal crystal fiber during heating and annealing studied by in situ synchrotron small angle X-ray scattering. *Langmuir*, 26(16):13216–20, 2010.

[167] X. Chen, S. Fischer, Z. Yi, V. Boyko, A. Terrenoire, F. Reinhold, J. Rieger, X. Li, and Y. Men. Structural Reorganization of a Polymeric Latex Film During Dry Sintering at Elevated Temperatures. *Langmuir*, 27(13):8458–8463, 2011.

[168] G. Herzog, M. A. K. Mottakin, G. Benecke, A. Buffet, R. Gehrke, J. Perlich, M. Schwartzkopf, V. Körstgens, R. Meier, M. A. Niedermeier, M. Rawolle, M. A. Ruderer, P. Müller-Buschbaum, W. Wurth, and S. V. Roth. Influence of nanoparticle surface functionalization on the thermal stability of colloidal polystyrene films. *Langmuir*, 28(21):8230–8237, 2012.

[169] C. Geng, L. Zheng, J. Yu, Q. Yan, T. Wei, X. Wang, and D. Shen. Thermal annealing of colloidal monolayer at the air/water interface: a facile approach to transferrable colloidal masks with tunable interstice size for nanosphere lithography. *Journal of Materials Chemistry*, 22(42):22678–22685, 2012.

[170] Yu. A. Vlasov, V. N. Astratov, A. V. Baryshev, A. A. Kaplyanskii, O. Z. Karimov, and M. F. Limonov. Manifestation of intrinsic defects in optical properties of self-organized opal photonic crystals. *Physical Review E*, 61(5):5784, 2000.

[171] Hernán Míguez, Francisco Meseguer, Cefe López, A Blanco, José S Moya, Joaquín Requena, Amparo Mifsud, and Vicente Fornés. Control of the Photonic Crystal Properties of fcc-Packed Submicrometer SiO(2) Spheres by Sintering. *Advanced Materials*, 10(6):480–3, 1998.

[172] B. Gates, S. H. Park, and Y. Xia. Tuning the Photonic Bandgap Properties of Crystalline Arrays of Polystyrene Beads by Annealing at Elevated Temperatures. *Advanced Materials*, 12(9):653–656, 2000.

[173] T. Deng, J.-Y. Zhang, K.-T. Zhu, Q.-F. Zhang, and J.-L. Wu. Temperature-modified photonic bandgap in colloidal photonic crystals fabricated by vinyl functionalized silica spheres. *Materials Chemistry and Physics*, 129(1-2):540–546, 2011.

[174] J. L. Keddie, R. A. L. Jones, and R. A. Cory. Size-Dependent Depression of the Glass Transition Temperature in Polymer Films. *Europhysics Letters (EPL)*, 27(1):59–64, 1994.

[175] J. Forrest, K. Dalnoki-Veress, J. Stevens, and J. Dutcher. Effect of Free Surfaces on the Glass Transition Temperature of Thin Polymer Films. *Physical Review Letters*, 77(10):2002–2005, 1996.

[176] O. Bäumchen, J. D. McGraw, J. A. Forrest, and K. Dalnoki-Veress. Reduced Glass Transition Temperatures in Thin Polymer Films: Surface Effect or Artifact? *Physical Review Letters*, 109(5):055701, 2012.

[177] J. E. Mark. *Polymer data handbook*, volume 27. Oxford university press New York, 2009.

[178] E. A. Sulyanova, A. Shabalin, A. V. Zozulya, J.-M. Meijer, D. Dzhigaev, O. Gorobtsov, R. P. Kurta, S. Lazarev, U. Lorenz, A. Singer, O. Yefanov, I. Zaluzhnyy, I. Besedin, M. Sprung, A. V. Petukhov, and I. A. Vartanyants. Structural Evolution of Colloidal Crystal Films in the Process of Melting Revealed by Bragg Peak Analysis. *Langmuir*, 903(2013):19–21, 2015.

[179] M. Sutton, S. G. Mochrie, T. Greytak, S. E. Nagler, L. E. Berman, G. A. Held, and G. B. Stephenson. Observation of speckle by diffraction with coherent X-rays. *Nature Publishing Group*, 1991.

[180] A. M. Alsayed, M. F. Islam, J. Zhang, P. J. Collings, and A. G. Yodh. Premelting at defects within bulk colloidal crystals. *Science*, 309(5738):1207–1210, 2005.

[181] M. A. Moram and M. E. Vickers. X-ray diffraction of III-nitrides. *Reports on Progress in Physics*, 72(3):36502, 2009.

[182] P. S. Turner. Thermal-expansion stresses in reinforced plastics. *Journal of Research of the National Bureau of Standards*, 37(4):239–250, 1946.

[183] E. M. Boczar, B. C. Dionne, Z. Fu, A. B. Kirk, P. M. Lesko, and A. D. Koller. Spectroscopic studies of polymer interdiffusion during film formation. *Macromolecules*, 26(21):5772–5781, 1993.

[184] M. A. Krivoglaz. *Diffuse Scattering of X-rays and Neutrons by Fluctuations*. Springer Verlag, 1996.

[185] R. Dronyak, J. Gulden, O. M. Yefanov, A. Singer, T. Gorniak, T. Senkbeil, J.-M. Meijer, A. Al-Shemmary, J. Hallmann, D. D. Mai, T. Reusch, D. Dzhigaev, R. P. Kurta, U. Lorenz, A. V. Petukhov, S. Düsterer, R. Treusch, M. N. Strikhanov, E. Weckert, A. P. Mancuso, T. Salditt, A. Rosenhahn, and I. A. Vartanyants. Dynamics of colloidal crystals studied by pump-probe experiments at FLASH. *Physical Review B*, 86(6):64303, 2012.

[186] S. Kalbfleisch, M. Osterhoff, K. Giewekemeyer, H. Neubauer, S. P. Krüger, B. Hartmann, M. Bartels, M. Sprung, O. Leupold, and F. Siewert. The holography endstation of beamline P10 at PETRA III. In *SRI 2009, 10TH INTERNATIONAL CONFERENCE ON RADIATION INSTRUMENTATION*, volume 1234, pages 433–436. AIP Publishing, 2010.

[187] D. I. Svergun, A. V. Semenyuk, L. A. Feigin, D. I. Svergun, A. V. Semenvuk, and L. A. Feigin. Small-angle-scattering-data treatment by the regularization method. *Acta Crystallographica Section A: Foundations of Crystallography*, 44(3):244–250, 1988.

[188] D. I. Svergun. Determination of the regularization parameter in indirect-transform methods using perceptual criteria. *Journal of Applied Crystallography*, 25(4):495–503, 1992.

[189] P. V. Konarev, M. V. Petoukhov, V. V. Volkov, and D. I. Svergun. ATSAS 2.1, a program package for small-angle scattering data analysis. *Journal of Applied Crystallography*, 39(2):277–286, 2006.

[190] D. I. Svergun, P. V. Konarev, V. V. Volkov, M. H. Koch, W. F. Sager, J. Smeets, and E. M. Blokhuis. A small angle X-ray scattering study of the droplet–cylinder transition in oil-rich sodium bis (2-ethylhexyl) sulfosuccinate microemulsions. *The Journal of Chemical Physics*, 113(4):1651–1665, 2000.

[191] W. Sun and Y.-X. Yuan. *Optimization theory and methods: nonlinear programming*, volume 1. Springer Science & Business Media, 2006.

Appendix A

Numerical integration of Takagi-Taupin equations on a 2D grid

In the numerical integration method the complex amplitudes $E_{0,h}(\mathbf{r})$ are represented by a discrete set of values over all integration grid and the equations are transformed to a recurrence matrix form, similar to Reference [99]. Taking into account that the equations are symmetric for the transmitted and the diffracted amplitudes, it is natural to take the same elementary integration step p for both directions. In order to estimate the partial derivatives using values from two neighboring points we use the central difference approximation, which is valid for any smooth, slowly varying function

$$\frac{\partial}{\partial x} f(x - \frac{p}{2}) = \frac{f(x) - f(x-p)}{p}. \tag{A.1}$$

The value of the function in this middle point is given by a half sum

$$f(x - \frac{p}{2}) = \frac{f(x)}{2} + \frac{f(x-p)}{2}. \tag{A.2}$$

When these formulas are applied to the differential equations (3.5) the those can be replaced by the following set:

$$\begin{aligned} & E_0(s_0, s_h) - E_0(s_0 - p, s_h) = \\ = \frac{i\pi}{2\lambda}[\chi_0 E_0(s_0, s_h) + \chi_0 E_0(s_0 - p, s_h) + BE_h(s_0, s_h) + BE_h(s_0 - p, s_h)], \\ & E_h(s_0, s_h) - E_h(s_0, s_h - p) = \\ = \frac{i\pi}{2\lambda}[\chi_0 E_h(s_0, s_h) + \chi_0 E_h(s_0, s_h - p) + DE_0(s_0, s_h) + DE_0(s_0, s_h - p)], \end{aligned} \tag{A.3}$$

with substitutions

$$\begin{aligned} B &= \chi_{\bar{h}} e^{i(s_0 - \frac{p}{2})\Delta\mathbf{q}\cdot\mathbf{e}_0 + is_h\Delta\mathbf{q}\cdot\mathbf{e}_h + i\mathbf{h}\cdot\mathbf{u}(s_0 - \frac{p}{2}, s_h)}, \\ D &= \chi_h e^{-is_0\Delta\mathbf{q}\cdot\mathbf{e}_0 - i(s_h - \frac{p}{2})\Delta\mathbf{q}\cdot\mathbf{e}_h - i\mathbf{h}\cdot\mathbf{u}(s_0, s_h - \frac{p}{2})}. \end{aligned} \tag{A.4}$$

All the considered points belong to the scattering plane, therefore in further derivations we simply omit the s_y coordinate in behalf of shortness. After little reorganization the set (A.3) can be simplified to

$$\begin{aligned} E_0(s_0, s_h) &= \frac{A}{C} E_0(s_0 - p, s_h) + \frac{B}{C} E_h(s_0, s_h) + \frac{B}{C} E_h(s_0 - p, s_h), \\ E_h(s_0, s_h) &= \frac{A}{C} E_h(s_0, s_h - p) + \frac{D}{C} E_0(s_0, s_h) + \frac{D}{C} E_0(s_0, s_h - p). \end{aligned} \tag{A.5}$$

Here two additional substitutions were made

$$\begin{aligned} A &= \frac{2\lambda}{i\pi p} + \chi_0, \\ C &= \frac{2\lambda}{i\pi p} - \chi_0, \end{aligned} \tag{A.6}$$

and it was assumed that $C \neq 0$, which is definitely true for any real positive p as far as $Im[\chi_0] \neq 2\lambda/(i\pi p)$. Solving this system with respect to $E_0(s_0, s_h)$ and $E_h(s_0, s_h)$ we obtain

$$\begin{aligned} E_0(s_0, s_h)[1 - \frac{BD}{C^2}] = \\ \frac{A}{C} E_0(s_0 - p, s_h) + \frac{B}{C} E_h(s_0 - p, s_h) + \frac{BD}{C^2} E_0(s_0, s_h - p) + \frac{BA}{C^2} E_h(s_0, s_h - p), \\ E_h(s_0, s_h)[1 - \frac{BD}{C^2}] = \\ \frac{AD}{C^2} E_0(s_0 - p, s_h) + \frac{BD}{C^2} E_h(s_0 - p, s_h) + \frac{D}{C} E_0(s_0, s_h - p) + \frac{A}{C} E_h(s_0, s_h - p). \end{aligned} \tag{A.7}$$

For convenience, these relations can be finally expressed in the matrix form

$$\begin{pmatrix} E_0(s_0, s_h) \\ E_h(s_0, s_h) \end{pmatrix} = \frac{1}{C^2 - BD} \begin{pmatrix} AC & BC & BD & BA \\ AD & BD & DC & AC \end{pmatrix} \begin{pmatrix} E_0(s_0 - p, s_h) \\ E_h(s_0 - p, s_h) \\ E_0(s_0, s_h - p) \\ E_h(s_0, s_h - p) \end{pmatrix} \tag{A.8}$$

Appendix B

Form factor evaluation

The form factor profiles $I(q)$ (see Figure 6.3) were obtained by azimuthal averaging of 2D diffraction patterns over the 2π angular range. This yields 1D intensity curves $\langle I(q)\rangle_\phi$ which includes also Bragg peaks. In order to eliminate the contribution of the Bragg peaks, the following iteration procedure was adopted. At each iteration step all intensity values along the ring of radius q exceeding the value $1.5\langle I(q)\rangle_\phi$ were not considered for the next angular averaging iteration. Repeating this procedure for seven iterations allowed us to filter Bragg peaks area from the data leaving information from the form factor of the colloidal particles.

The form factor data for the experiment A were fitted using GNOM program [187, 188] from the ATSAS package [189]. The calculation was made assuming that the scattering originates from uniform spherical particles. Results of fitting of the form factor data at room temperature T_R are shown in Figure B.1(a). By fitting the peak of volume size distribution function $V(r)$

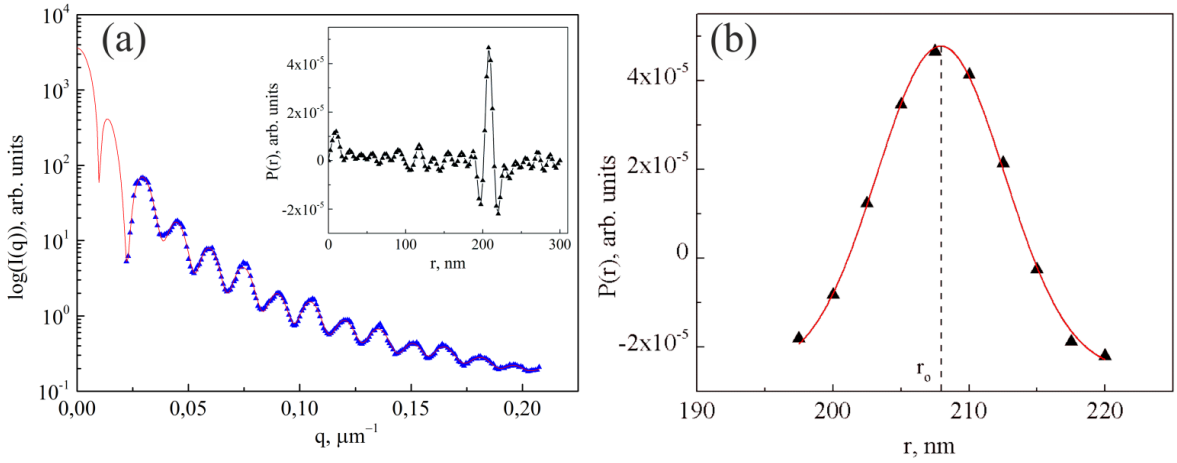

Figure B.1: (a) Form factor data and results of fitting for the experiment A at room temperature. Volume size distribution function $V(r)$ obtained from the results of fitting is shown in the inset. Negative values of $V(r)$ function are due to termination effects of the Fourier transform algorithm. (b) Gaussian function fitting of the peak of $V(r)$ function. The position of the center of a Gaussian distribution r_0 corresponds to an average diameter $D = 2r_0$ of colloidal particles. The polydispersity of colloidal particles in the sample is determined by the width (sigma-value) of Gaussian distribution.

with a Gaussian profile one can determine the diameter and polydispersity of PS particles (see

Figure 6.8(b)). The center position r_0 provides the diameter $D = 2r_0$ of colloidal particles and the r.m.s. width σ defines the polydispersity of particles size distribution as σ/r_0 [190]. The polydispersity of PS colloidal particles in the experiment A was determined to be (2.2 ± 0.2) %, which agrees well with the polydispersity value measured by DLS.

Appendix C

Bragg peak evaluation

Position of the direct beam in a diffraction pattern was determined as the one corresponding to the maximum of the correlation function between the original image and the centrosymmetrically inverted image. The results were averaged over all images containing Bragg peaks and the same coordinates were used for the whole dataset.

The initial position of the Bragg peaks was determined as a position of pixels with maximum intensity, separated by a distance not less than $0.6q_0$, where q_0 is the distance between the nearest Bragg peaks. To exclude false and too weak maxima, the q-dependence of the averaged intensitywas calculated for every image, and only the maxima twice stronger than the average value were selected. Later the positions obtained in this first step were updated from the results of fitting.

The measured intensity distribution around each Bragg peak was considered in the orthogonal coordinate system with the origin in the peak maximum, q-axis directed along the q-vector of the peak (radial coordinate), and ϕ-axis perpendicular to it (azimuthal coordinate) (see Figure 6.4).

The intensities within the circle area with the radius about $0.3q_0$ of the distance to the closest reflections were fitted using two-dimensional Gaussian function (see Figure C.1)

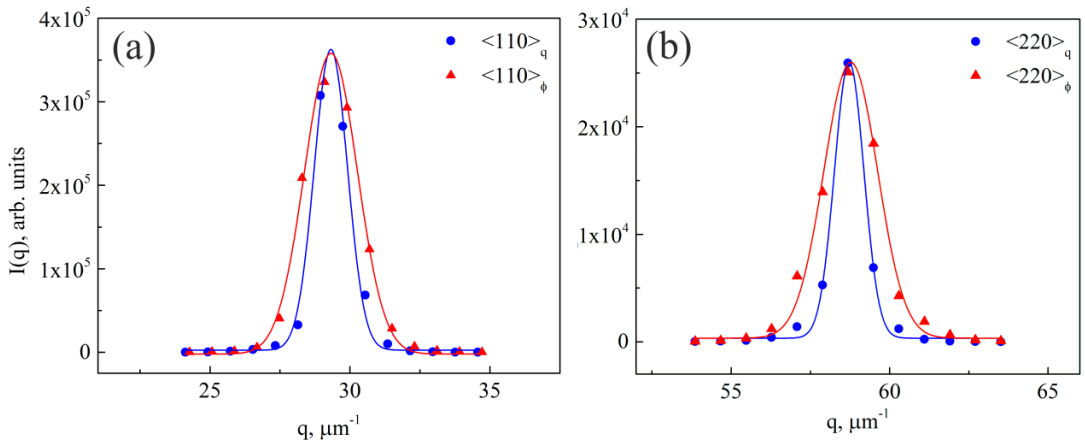

Figure C.1: The radial (q) and azimuthal (ϕ) profiles of 110 (a) and 220 (b) Bragg peaks fitted with Gaussian function.

$$I(r_q, r_\phi) = I_0 exp\Big(- \frac{(r_q - R_q)^2}{2w_q^2} - \frac{(r_\phi - R_\phi)^2}{2w_\phi^2} \Big), \tag{C.1}$$

where I_0, R_q, R_ϕ, w_q, and w_ϕ are the fitting parameters: peak intensity, positions of a Bragg peak and FWHMs in radial (q) and azimuthal (ϕ) directions, correspondingly. The fitting was performed by gradient descent algorithm [191] for each individual Bragg peak and results were averaged over all six equivalent Bragg peak reflections. The results of fitting procedure are shown in Figure 6.5 and Figure 6.5 for experiment A and B, respectively. Weak peaks, not fully measured peaks (for instance, the peaks obscured by a beamstop or detector gaps), and peaks with the fitted parameters significantly different from the others were excluded from the analysis.

In the experiment B a focused beam with the size of a few microns at the sample was used, which contributes to additional broadening of measured Bragg peaks as compared to the experiment A conducted using an unfocused beam. For the experiment B a deconvolution of the peak width was performed assuming Gaussian shape of both the intrinsic width w_i of a reflection and instrumental broadening w_{inst} that gives for the experimental peak width $w_{exp}^2 = w_i^2 + w_{inst}^2$. In the experiment A an unfocused beam was used, and the condition $w_{inst} << w_i$ was fulfilled making the deconvolution not necessary.

A total average lattice parameter $\langle a_{[110]} \rangle$ along the [110] crystallographic direction, which is equal to the nearest-neighbor distance, was determined in the following way. An average lattice parameter for one selected crystallographic direction n for hexagonal lattice [19] was defined as $\langle a_{[110]} \rangle_n = 2\langle d_{[110]} \rangle_n$, where an average interplanar distance is calculated as:

$$\langle d_{[110]} \rangle_n = \frac{2\pi}{\langle q_{[110]} \rangle_n}. \tag{C.2}$$

An average value of the diffraction vector $\langle q_{[110]} \rangle_n$ was derived using the equation:

$$\langle q_{[110]} \rangle_n = \frac{\sum\limits_h \alpha_h \left(q_{hh0}^n / h \right)}{\sum\limits_h \alpha_h}. \tag{C.3}$$

where summation is performed over all $hh0$ reflections determined in the experiment and $\alpha_h = h^2$ is a weight function that takes into account that the higher order Bragg peaks can be determined with higher precision then the lower order ones. The total average lattice parameter was calculated by averaging the values obtained for each of six crystallographic directions $\langle q_{[110]} \rangle = \frac{1}{6} \sum\limits_{n=1}^{6} \langle a_{[110]} \rangle_n$.